Lanthanide-doped Nanoparticles in Sol-Gel Matrices; Improved Optical Properties and New Opportunities

by

Sri Sivakumar
B. Sc. (Tech) University of Mumbai, India, 1997
M. Sc. (Tech) University of Mumbai, India, 2001

A Thesis Submitted in Partial Fulfillment of the
Requirements for the Degree of

DOCTOR OF PHILOSOPHY
in the Department of Chemistry

Lanthanide-doped Nanoparticles in Sol-Gel Matrices; Improved Optical Properties and New Opportunities

by

Sri Sivakumar

B. Sc. (Tech) University of Mumbai, India, 1997
M. Sc. (Tech) University of Mumbai, India, 2001

Supervisory Committee

Dr. Frank C. J. M. van Veggel, (Department of Chemistry)
Supervisor

Dr. Cornelia Bhone, (Department of Chemistry)
Departmental Member

Dr. Peter Wan, (Department of Chemistry)
Departmental Member

Dr. Robert Burke, (Department of Biology/Biochemistry & Microbiology)
Outside Member

Supervisory Committee

Dr. Frank C. J. M. van Veggel, Department of Chemistry
Supervisor
Dr. Cornelia Bhone, Department of Chemistry
Departmental Member
Dr. Peter Wan, Department of Chemistry
Departmental Member
Dr. Robert Burke, Department of Biology/Biochemistry & Microbiology
Outside Member

ABSTRACT

This thesis describes the incorporation of lanthanide-doped nanoparticles into sol-gel matrices to improve the optical properties of lanthanide ions and these materials can potentially be used in white light devices, optical amplifiers, lasers, and biolabeling. Bright white light has been generated from sol-gel thin films (SiO_2 and ZrO_2) made with lanthanide-doped nanoparticles through up-conversion of a single 980 nm light source. The up-conversion mechanisms involved in the generation of light has been discussed. A new and potentially efficient up-conversion process named cross-relaxation-enhanced energy-transfer (CREET) up-conversion process has been described. Preparation of semiconductor sol-gel thin films with lanthanide-doped nanoparticles has been discussed and they show energy transfer from the semiconductor matrix to the lanthanide ions. The preparation and bioconjugation of nearly monodisperse (40 nm) silica-coated $LaF_3:Ln^{3+}$ nanoparticles has been described.

Supervisor: Dr. ir. Frank C. J. M. van Veggel (Department of Chemistry)

Table of Contents

CHAPTER 3

List of Figures and Schemes

CHAPTER 2

CHAPTER 3

CHAPTER 4

CHAPTER 5

List of Tables

CHAPTER 2

CHAPTER 3

Acknowledgements

I would like to take this opportunity thank my supervisor Prof. dr. ir. Frank C. J. M. van Veggel for his guidance, patience, and wisdom that allowed me to stay focused during my studies. In addition, I would like to thank Prof. dr. Stanley P. May and Prof. dr. Mary Berry for his helpful suggestions for the new CREET up-conversion mechanism. I wish to acknowledge Dr. Mati Raudsepp for all XRD measurements. Additionally, I want to thank Dr. Cornelia Bohne for her suggestions with regards to troubleshooting of the fluorimeter. I also thank all my committee members for providing me the support during the last four years. Special thanks to Peter Diamente for his suggestions and help in bioconjugation work.

I am especially grateful for all the help that Sudarsan, Venkat, and Wiljan have given me over the past four years. I would like to acknowledge all my group members for their help and suggestions.

I want to thank my family for giving me the support to finish my degree successfully. To my wife Vimala, thank you for giving me the support that I needed when the going got tough and for your unconditional love.

Finally, thanks to the chemistry staff for their help in various areas that have helped me to complete this thesis.

CHAPTER 1

General Introduction

1.1 Introduction

In the current age of technology there is a demand for optical materials for various applications such as general lighting purposes, LCD backlight, displays, optical amplifiers, and lasers. Investigation of artificial light sources and candles has been started in the 19th century. Artificial light was first produced by pyroluminescence, which is due to radiative transitions of excited atoms and ions, recombination of ions to form molecules, and incandescence of solid particles in a flame. In the second decade of 19th century carbon-arc discharge lamps were developed with longer lifetime (1000 hours) and they were widely used in street lighting. In 1879, Thomas Alva Edison introduced a new age of research on the generation of light by demonstrating a first incandescent light powered by electricity. Despite many years of use, incandescent light bulbs, have low efficiencies (10-12%).[1,2] Lateron, mercury vapour lamps and fluorescent light tubes were developed and they are still in use. Lanthanide ions are used as the emitting species in fluorescent tubes because of their stable photocycle, increased brightness, and high quantum yield. In fluorescent tubes ultra violet (UV) light is the excitation source which is converted into visible (white) light. The overall efficiency of these lighting sources is still relatively low (< 28%) because they also emit infrared (IR) light as heat. In order to address these issues, inorganic-light emitting diodes (ILEDs), organic light-emitting diodes (OLEDs), and polymer light-emitting diodes (PLEDs) are being developed with some major advances. ILEDs such as GaN, InGaN, and InGaAs are fabricated mainly by molecular beam epitaxy (MBE) and metal-organic vapour phase epitaxy (MOVPE) methods which are generally expensive. OLEDs and PLEDs are developed as an alternative to ILEDs with some major recent progress. However, the generation of white

light from OLEDs/PLEDs has some limitations. These include inefficient blue/white emitters, bias dependent colour variation, multilayer devices (leading to increase in fabrication cost), and low photostability. Despite all the recent advances in the lighting technology, there is still a need to develop alternative white light sources. This may be achieved by combining the advantages of lanthanide ions and sol-gel processes.

Sol-gel is one of the promising methods for easy and cost effective fabrication of devices such as optical amplifiers and thin film devices. Increased optical properties are proven by incorporation of lanthanide ions into sol-gel matrices. However, luminescence of lanthanide ions can be quenched by the residual OH groups, an inherent result of the sol-gel process. In addition, clustering of the lanthanide ions reduces the excited state lifetime by concentration quenching. Therefore, a general method is needed to improve the luminescent properties of lanthanide ions in sol-gel films by isolating the luminescent lanthanide ions from the vibrations of the residual OH groups, reducing the phonon energy of the host, and avoiding clustering of the lanthanide ions.

The goal of the thesis is to improve the optical properties (up-conversion efficiency, long luminescence lifetime, and quantum yield) of lanthanide ions through development of new materials and methods and that can potentially be applied to general lighting devices, optical amplifiers, thin film devices, and detection of biomolecules. This is achieved by incorporating lanthanide-doped nanoparticles into sol-gel matrices. These materials are characterized by fluorescence spectroscopy, powder X-ray diffraction (XRD), transmission electron microscopy (TEM), and atomic force microscopy (AFM).

In chapter 2 an overview of optical properties of lanthanide ions and different up-conversion mechanisms are described. A general outlook of lanthanide ions in different

matrices, sol-gel process, different white light sources, and biolabels is discussed in detail.

Chapter 3 demonstrates the generation of white light from SiO_2/ZrO_2 sol-gel thin films made with lanthanide-doped nanoparticles by up-conversion of single NIR source (980 nm). In part I of this chapter, first example of white light generation is described and in part II, methods to increase in the efficiency of generation of white light and different up-conversion mechanisms involved in the white light generation is discussed in detail.

Chapter 4 describes a new and potentially efficient up-conversion mechanism called cross-relaxation enhanced energy transfer (*hetero*-LEET) up-conversion process. Bright green and red emission is generated from Er^{3+} ion through *hetero*-LEET up-conversion process with high quantum yield. The advantage of this mechanism over the existing mechanism is discussed.

Sensitized emission from lanthanide-doped nanoparticles embedded in a semiconductor matrix is discussed in Chapter 5. Preparation and characterisation of semiconductor sol-gel thin films made with lanthanide-doped nanoparticles and semiconductor-coated lanthanide-doped nanoparticles is described in detail. These materials are potential candidate for light emitting diodes.

Chapter 6 demonstrates the preparation and bioconjugation of silica-coated lanthanide-doped nanoparticles as potential biolabels. A wide range of emission lines (450 – 1650 nm) is achieved by doping with selected lanthanide ions. The emission at 800 nm is produced from silica-coated Yb^{3+}/Tm^{3+}-doped nanoparticle through up-conversion of 980 nm light, which is within the biological window (700-1300 nm).[3,4] In this region skin and other biological materials are most transparent, as compared to Ultra violet-

visible light (UV-Vis), thus allowing for deeper penetration of excitation and detection the emission.

The overall summary of the work done is described at the end of the thesis.

References

(1) D'Andrade, B. W.; Forrest, S. R. *Adv. Mater.* **2004**, *16*, 1585.

(2) Service, R. F. *Science* **2005**, *310*, 1762.

(3) Loo, C.; Lowery, A.; Halas, N.; West, J.; Drezek, R. *Nano Lett.* **2005**, *5*, 709.

(4) Nehl, C. L.; Grady, N. K.; Goodrich, G. P.; Tam, F.; Halas, N. J.; Hafner, J. H. *Nano Lett.* **2004**, *4*, 2355.

CHAPTER 2

Optical properties of lanthanide-ions

2.1 Introduction

The lanthanide ions, also known as rare-earth ions, occupy a special place in the periodic table. They are placed separately from the other elements at the bottom of the table because of their unique properties which are discussed later in this chapter. The word lanthanide has originated from Greek a word (*λανθανειν*) which means "to lie hidden".[1] This is a very appropriate word for these ions because it took several years to identify all these ions and moreover these ions were hardly available in earlier days, hence their second name is rare-earth ions. However, they were not rare. The principle sources of lanthanide ions are Bastnasite ($LnFCO_3$), Monazite (Ln, Th)PO_4, and Xenotime (Y, Ln)PO_4.[2] These ores are abundantly available in China which amount to 70% of the known deposits. These ores are very rich in lanthanide ions. The lanthanide ions are obtained industrially by treating their ores first with caustic soda and then hydrochloric acid. The resulting aqueous solutions of chlorides of the lanthanide ions are then separated by column chromatography.

Lanthanide ions are have a wide range of technological applications such as, catalysis,[3-6] batteries,[7] optics,[8,9] and bioapplications.[10,11] They are mainly used in modern household applications such as fluorescent tubes, the cathode ray tubes in televisions and monitors, and plasma display panels. In these applications lanthanide ions are used to convert high-energetic radiation (UV) into visible light. The commonly used phosphors in these applications are $Y_2O_2S:Eu^{3+}$ (red), $Y_2O_3:Eu^{3+}$ (red), $LaPO_4:Ce^{3+}$, Tb^{3+} (green), $GdMgB_5O_{10}:Ce^{3+}$, Tb^{3+} (green), and $BaMgAl_{10}O_{17}:Eu^{2+}$ (blue).[12] Apart from lighting applications, lanthanide ions are also used in lasers and optical amplifiers. For example,

YAG:Nd^{3+} is being used in solid compact lasers[13,14] and Er^{3+}-doped EDFA fiber is being used as an amplifier in telecommunications.[15]

2.2. Unique properties of lanthanide ions

Lanthanide ions exhibit a number of unique properties in their chemistry that differentiate them from the other elements: 1) they have a wide range of co-ordination numbers, 2) their 4*f* electrons are well shielded from the environment by outer 5*s* and 5*p* orbitals and minimally involved in chemical bonding, which leads to minimal effect by the crystal field environment and high stability during photophysics (transition happens within the 4*f* shell in most cases), 3) the transition between the 4*f* electrons are parity forbidden however, they do occur due to mixing with allowed transitions like the 4*f*-5*d* transitions, 4) the result of 3 is, that the lanthanide ions possess low extinction coefficients (<10 $M^{-1}cm^{-1}$)[11] and long lifetime (up to several milliseconds), 5) they prefer anionic ligands with donor atoms possessing high electronegativity (O and F), 6) all the ions show similar reactivity because of the same valence electrons, 7) lanthanide ions often have several luminescent excited states, in contrast with Kasha's rule[16] of organic chromophore, which states that typically multiplicity luminescence occurs only from the lowest state of a given spin, and 8) lanthanide ions can generate light either by down-conversion or up-conversion. Down-conversion (Figure 2.1a) is the conversion of higher energy photons (UV) into lower energy photons (visible). On the other hand, the process (Figure 2.1b) which converts lower energy photons (NIR) into higher energy photons (visible) involving real meta-stable state is generally called an up-conversion process.

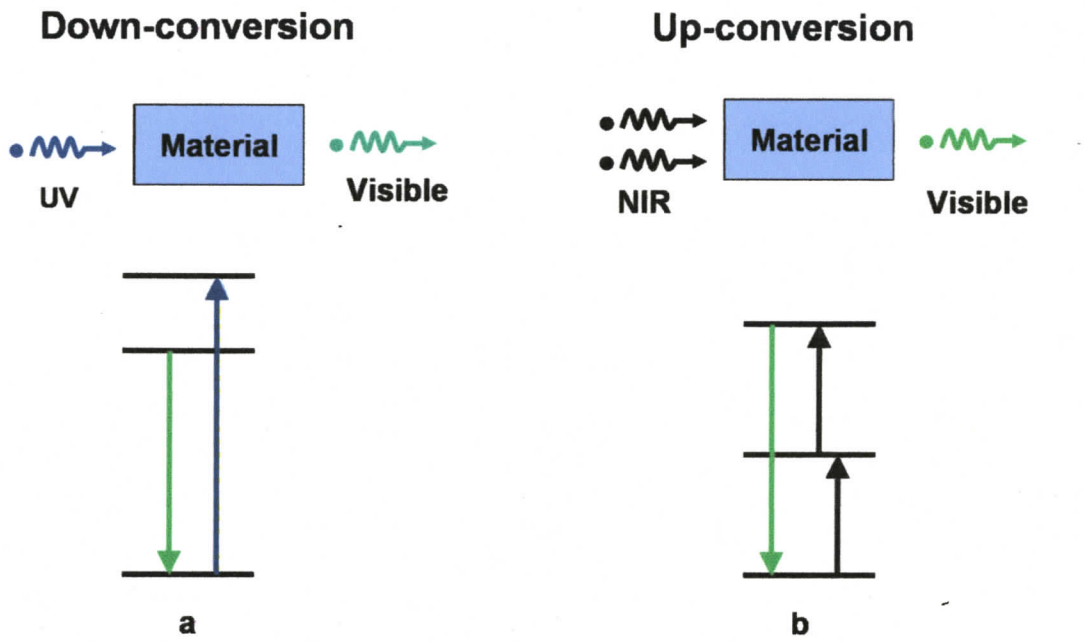

Figure 2.1. Schematic diagram of a) Down-conversion, b) up-conversion (Schematic)

Figure 2.2 demonstrates the energy levels of lanthanide ions, Pr^{3+}, Nd^{3+}, Sm^{3+}, Eu^{3+}, Gd^{3+}, Tb^{3+}, Dy^{3+}, Ho^{3+}, Er^{3+}, Tm^{3+}, and Yb^{3+}. The number of absorption bands depends on the corresponding lanthanide ion and its arrangement of electronic states (see later). Depending upon the co-ordinating ligands and crystal field, only a minimal change is observed in the emission and absorption spectra of lanthanide ions such as small displacements in the peak positions and changes in the relative intensities of some of the emission peaks. This property can be useful to investigate the local environment of lanthanide ion. Three lanthanide ions (La^{3+}, Ce^{3+}, and Lu^{3+}) are not presented (Figure 2.2) because, La^{3+} and Lu^{3+} ion has completely empty and filled shell respectively, which leads to no optical transition. Ce^{3+} has only one electron and one 4*f* level just above ground state, however, it possess an allowed 4*f*-5*d* transition in the ultra violet (UV)

region because of its lower oxidation potential. Because of the allowed 4*f*-5*d* transition the lifetime of Ce^{3+} is much shorter (nanoseconds) than the trivalent lanthanide ions.

The energy levels of the free lanthanide ions arise from interactions between the $4f^n$ electrons, i.e. Coulomb repulsion and spin-orbit coupling. When the lanthanide ion is incorporated in a crystal, the electric field of the ligand produces a crystal field which splits the multiplets into crystal-field levels or Stark levels. The splitting is very small (up to a few hundred cm^{-1}) because of the small interaction between the $4f^n$ electrons and the crystal field. Because of this reason, this energy level diagram can be used effectively as a good starting point for lanthanide ion incorporated in any host. The energy levels are named by Russel-Saunders notation, $^{(2S+1)}\Gamma_J$, where S is the spin multiplicity, Γ is the angular momentum, and J is the total angular momentum.

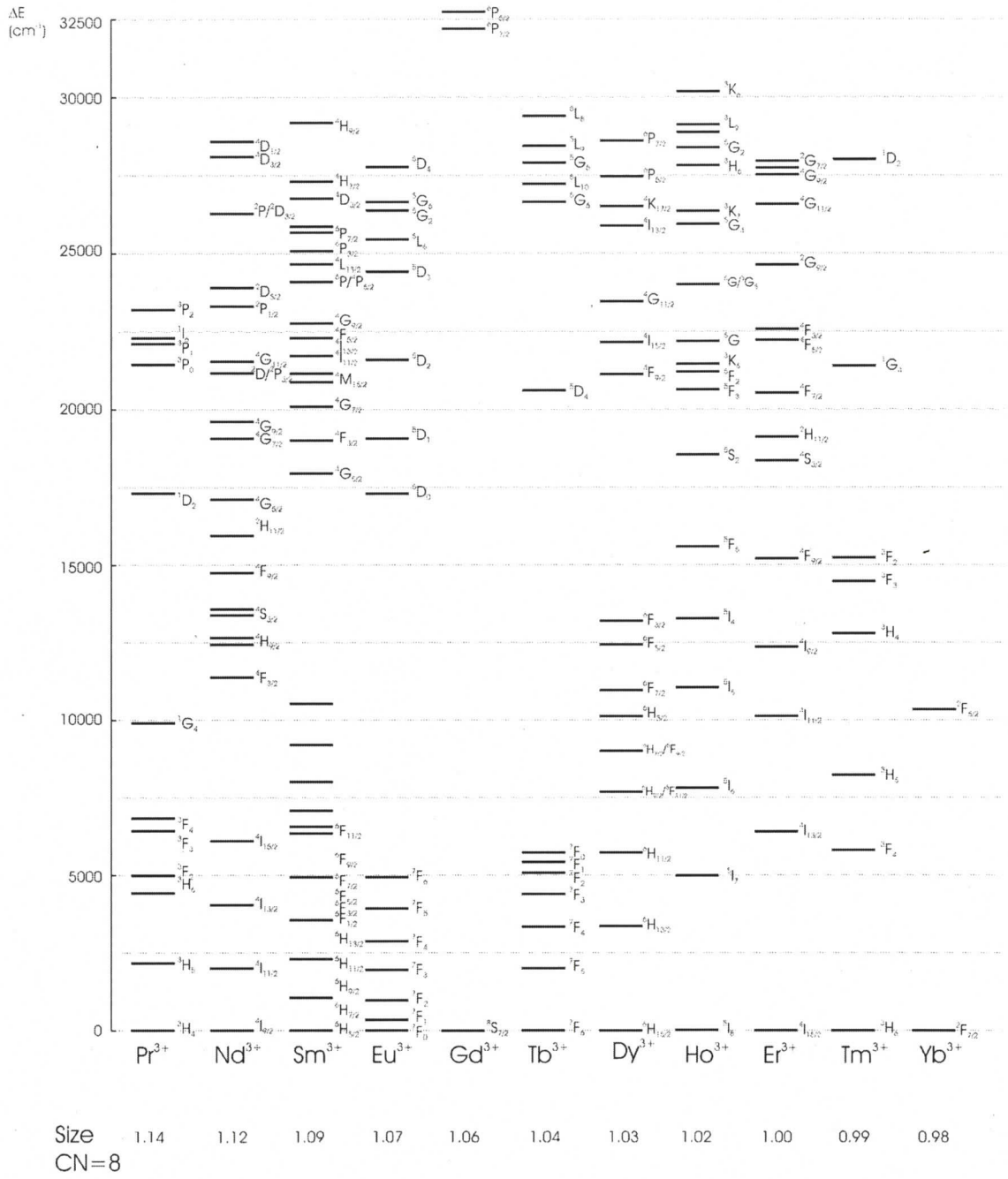

Figure 2.2. Energy level diagram of lanthanide ions in aqueous solution[17] (the sizes are taken from *CRC handbook of chemistry and physics*[1]).

Table 2.1 shows the important emissions of lanthanide ions and their technological applications.

Table 2.1. Important emissions of lanthanide ions and their applications

Lanthanide ion	Transition	Wavelength (nm)	Application
Eu^{3+}	$^5D_0 \rightarrow {}^7F_1, {}^7F_2$	591 and 612	Lightings, displays, biolabels
Tb^{3+}	$^5D_4 \rightarrow {}^7F_5$	545	Lightings, displays, biolabels
Tm^{3+}	$^1D_2 \rightarrow {}^3F_4$ $^1G_4 \rightarrow {}^3H_6$ $^3H_4 \rightarrow {}^3F_4$	450 475 1480	Lightings Lightings Optical amplifiers
Er^{3+}	$^4S_{3/2} \rightarrow {}^4I_{15/2}$ $^4F_{9/2} \rightarrow {}^4I_{15/2}$ $^4I_{13/2} \rightarrow {}^4I_{15/2}$	545 660 1540	Lightings , lasers Lightings, lasers Optical amplifiers
Ho^{3+}	$^5S_2 \rightarrow {}^5I_8$ $^5F_5 \rightarrow {}^5I_8$	540 640	Lightings , lasers Lightings , lasers
Nd^{3+}	$^4F_{3/2} \rightarrow {}^4I_{11/2}$	1064	Lasers
Yb^{3+}	$^2F_{5/2} \rightarrow {}^2F_{7/2}$	980	Sensitizers
Dy^{3+}	$^6F_{11/2} + {}^6H_{9/2} \rightarrow {}^6H_{15/2}$	1330	Optical amplifiers
Pr^{3+}	$^1G_4 \rightarrow {}^3H_5$	1330	Optical amplifiers

2.3. Up-conversion

Up-conversion, simultaneous multi-photon absorption, and second-harmonic generation are well established methods for the generation of higher energy photons from lower energy photons. The up-conversion process (Figure 2.3a) is generally based on sequential absorptions or energy transfer steps involving one or more metastable excited states that are intermediate in energy between the ground state and the emitting state of the ion. This process requires the absorption of at least two photons to provide sufficient energy for the up-converted emission to occur. This event is different from multi-photon absorption and second-harmonic generation processes. The multi-photon processes (Figure 2.3b) require only one real excited state and high excitation densities. Second harmonic generation (Figure 2.3c) produces frequency doubled photons through relatively weak wavelength-dependent hyperpolarizability of a substance which also requires coherent radiation. Up-conversion has been demonstrated as an efficient process when compared to other two processes, because it does not require high excitation densities.

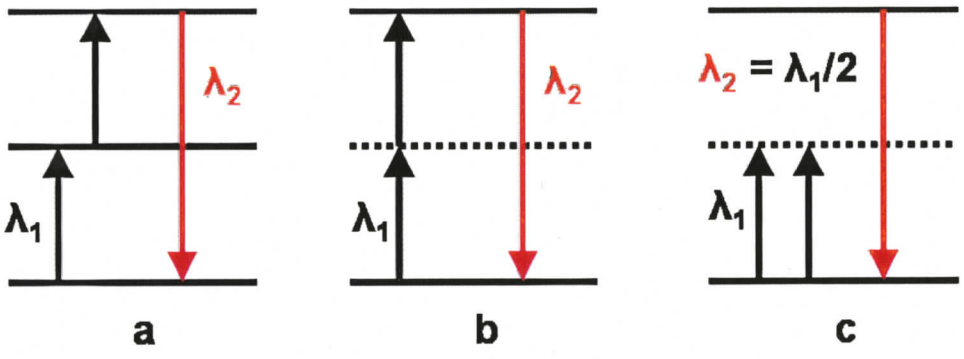

Figure 2.3. Schematic diagram of a) Up-conversion, b) simultaneous multi-photon absorption, and c) second harmonic generation.

Lanthanide ions are particularly suitable candidates for up-conversion process because of their $4f^n$ energy level structure, which provides many intermediate levels with favourable spacings and long-lived excited states. Many researchers[18,19] have investigated the up-conversion of lanthanide-doped materials since 1960 because they could be used for several potential important photonic applications including up-conversion lasers, displays, solid state lighting, fluorescence imaging for detection of biomolecules, optical data storage, LCD back light, and phosphor materials.[20-24] Up-conversion occurs via three mechanisms, 1) ground state/excited state absorption (GSA/ESA), 2) energy transfer up-conversion (ETU), and 3) photon-avalanche (PA) processes.[18]

2.3.1 Ground state/excited state absorption (GSA/ESA)

GSA/ESA up-conversion process (Figure 2.4) is a single-ion mechanism, which involves a minimum of two consecutive transitions. First, the ion is excited to an intermediate long-lived excited state followed by the absorption of second photon, promoting the ion to an even higher excited state. The second photon can be varied in energy when a dual (tunable) excitation source like a dye-laser is used. This is unlikely in the case of two-photon absorption process because both the photons should have the same energy. This single-ion mechanism is the simplest up-conversion process by which higher excited state may be produced, and is one of the most important up-conversion mechanisms operative in rare-earth up-conversion materials. At low excitation powers, this up-conversion luminescence demonstrates a quadratic dependence on excitation power, if two photons are involved in the process. GSA/ESA would be the most likely mechanism in samples with low dopant concentration because the dopant ions are too far

away to interact with each other. Many research groups have investigated this mechanism in different type of materials such as fluorides,[25,26] oxides,[27-29] and glasses[30,31] doped with lanthanide ions.

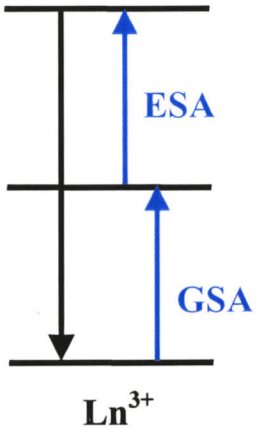

Figure 2.4. Schematic diagram of ground state/excited state absorption up-conversion mechanism

2.3.2. Energy transfer up-conversion mechanism

Besides multistep excitation due to classical ground state/excited state absorption (GSA/ESA), there is an efficient process of up-conversion by sequential energy transfers which has been named by Auzel as APTE effect (for addition de photon par transferts d'energie) in 1966.[32] This effect was later rebranded as energy transfer up-conversion (ETU) process. Energy transfer up-conversion process involves two ions where the ion being first directly excited is called sensitizer or donor and the ion to which the energy is transferred and which subsequently emits a photon is called acceptor or activator. Energy transfer up-conversion occurs in three steps (Figure 2.5). First, the sensitizer or donor is

excited into one of its excited state by ground state absorption while the acceptor or activator ion is in its ground state. Second, due to interactions between donor and acceptor, the donor transfers its energy to acceptor to promote the acceptor to one its excited state. Third, the acceptor further promoted to its higher excited state by another energy transfer process from another excited donor and followed by the emission from acceptor.

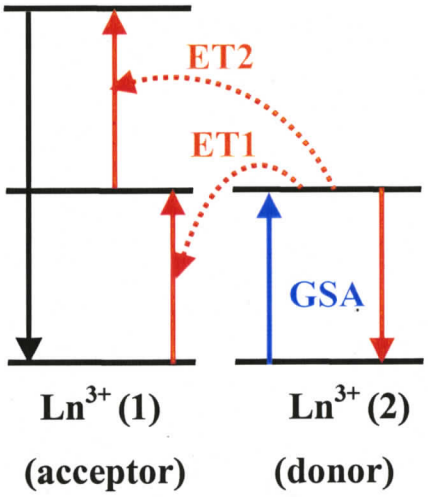

Figure 2.5. Schematic diagram of energy transfer up-conversion process

There are different types of energy transfer up-conversion processes which are described in literature and they are schematized in Figure 2.6. They are, 1) resonant radiative energy transfer (Figure 2.6a), 2) resonant non-radiative energy transfer (Figure 2.6b), and 3) phonon-assisted non-radiative energy transfer (Figure 2.6c). In resonant radiative energy transfer, the donor ion emits a photon which is absorbed by the acceptor ion. In non-radiative energy transfer, the donor ion transfers its excitation energy to the acceptor due to interaction between donor and acceptor. The mutual interactions are of dipole-dipole interaction type which was first investigated by Förster.[33] Often quadrupole

and higher multipole interactions are involved. In phonon-assisted energy transfer there is mismatch in energy levels of donor and acceptor ion. During the energy transfer from donor to acceptor ion the excess energy can be taken up by matrix in the form of vibrational energy. For example, up-conversion of Yb^{3+}/Tm^{3+}, Yb^{3+}/Ho^{3+} -doped materials with 980 nm is a phonon-assisted up-conversion process. This up-conversion process is relatively inefficient compared to the resonant radiative/non-radiative up-conversion process.

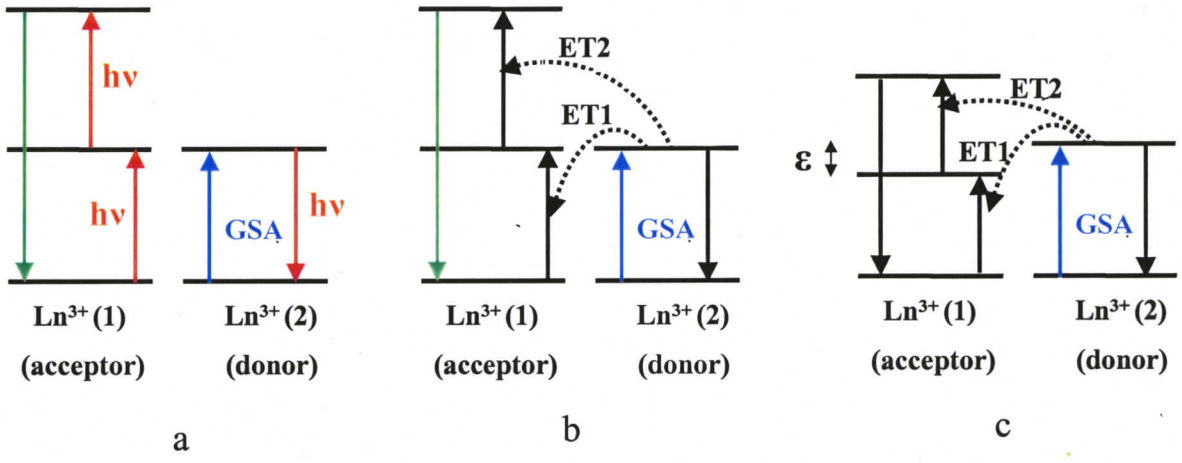

Figure 2.6. Schematic diagram of a) resonant radiative energy transfer, b) resonant non-radiative energy transfer, and c) phonon-assisted non-radiative energy transfer (ε = energy mismatch, which is taken up via a phonon assisted process)

Energy transfer can happen between two identical lanthanide ions or two different lanthanide ions. Energy transfer from one lanthanide ion can be used to enhance the luminescence of another lanthanide ion. For example, materials doped with Yb^{3+}-Er^{3+} ions produce green/red up-conversion, in which Yb^{3+} is excited at 980 nm and then the excited Yb^{3+} ion transfers its energy to an Er^{3+} ion. The Er^{3+} ion has a relatively low absorption cross-section at 980 nm (~1 $M^{-1}cm^{-1}$), whereas, the Yb^{3+} ion exhibits a much

large absorption cross section (~10 $M^{-1}cm^{-1}$) in this region and thus, co-doping with Yb^{3+} ion has proven to be a successful sensitizer in the up-conversion process.[17] Moreover, these materials can be excited with cheap 980 nm continuous wave (CW) lasers. Many research groups have demonstrated that the efficiency of up-conversion increases with co-doping of Yb^{3+} ion. Capobianco *et al.* have demonstrated that the co-doping of Yb^{3+} ion with $Y_2O_3:Er^{3+}$,[34,35] $Lu_2O_3:Er^{3+}$ nanocrystal/bulk material,[28] and $Gd_2GaO_3:Tm^{3+}/Ho^{3+}$ nanocrystal/bulk materials[36-38] increase the efficiency of up-conversion process. Güdel *et al.* have shown that the increase in the efficiency of the up-conversion in $NaYF_4$:Tm/Er[39-42] and $NaGdF_4$:Tm/Er[43,44] nanocrystals co-doped with Yb^{3+} ion. Auzel has summarized the up-conversion properties of materials co-doped with Yb^{3+} ion in a recent review.[19]

2.3.3. Cross-relaxation

Cross-relaxation terminology usually refers to all types of down-conversion energy transfers occurring between two identical ions (Figure 2.7). A lanthanide ion in the excited state 3 can transfer part of its energy to a neighbouring lanthanide ion promoting it to the excited state 2. This leads two ions in the excited state 2. This cross-relaxation process happens in the photon-avalanche up-conversion process (see below). An increase in the doping concentrations of lanthanide ion facilitates the chances of cross-relaxation. It can also happen between two different ions. Cross-relaxation may give rise to energy migration process where the excited state energy levels of two identical ions are resonant. An increase in the doping concentration leads to a faster energy migration through the material, making the chance of meeting a quenching site

higher which leads to a decrease/leveling off the luminescence intensity and luminescence lifetime.

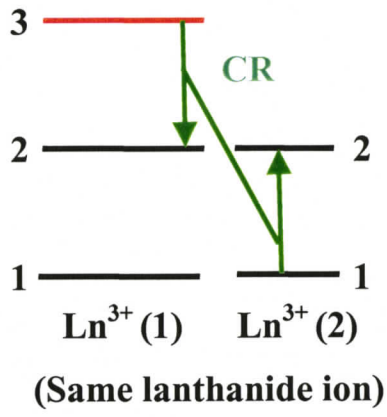

Figure 2.7. Schematic diagram of cross-relaxation process.

2.3.4. Photon-avalanche (PA) up-conversion process

The most recently discovered up-conversion process is the photon-avalanche process in Pr^{3+}-doped $LaCl_3$ or $LaBr_3$ crystals.[45,46] In a photon-avalanche mechanism (Figure 2.8), the intermediate reservoir level 2 is populated through a very weak non-resonant ground state absorption which can also be called phonon-assisted ground state absorption. Subsequently, it is further excited to upper excited level 3 by a resonant excited state absorption. After this initial 'seeding' step, an efficient cross-relaxation populates the key reservoir level 2 of $Ln^{3+}(1)$ ion as well as neighbouring ion ($Ln^{3+}(2)$) to produce two ions in the key reservoir level. Subsequently, these two ions can be further excited to upper excited level 3. After which, by the same feeding process, four ions will be further in this metastable state and so on. The extremely non-linear buildup of the intermediate excited state population arising in this way has earned this mechanism the name of photon-avalanche. Because the up-conversion luminescence intensity is directly

related to the population of the key reservoir intermediate state, the photon-avalanche is observed in up-conversion luminescence experiments.

The photon-avalanche process is characterized by three distinct non-linear behaviours: 1) decrease in the transmission, 2) appearance of threshold in power dependence graph, and 3) long rise time on the pump power intensity (temporal evolution graph) with generally the existence of a critical pump threshold. First, the population of intermediate reservoir level can be monitored by measuring the transmission of the single crystal at the excitation laser energy. It diminishes exactly in the same way as the up-conversion luminescence intensity increases because of the buildup of avalanche and thus loses its transparency at this energy. Second, the appearance of a threshold and a S-shape in the power dependence graph, in which the variation of up-conversion fluorescence intensity vs. pump power is plotted. This is characterized by a large increase in the up-conversion fluorescence intensity at a specific intensity at a specific value of the pump intensity. An example of the pump threshold behaviour is shown schematically in Figure 2.9. Below the threshold the fluorescence intensity is due primarily to non-resonant two-photon process and increases quadratically. In the threshold, the slope is >2 and in higher powers the slope starts to decrease due to the partial saturation of corresponding levels of lanthanide ions. The large increase in fluorescence intensity at threshold results from the reservoir level population produced by photon-avalanche up-conversion pumping. The appearance of a threshold and a S-shape in the power dependence graph confirms the presence of this pump mechanism. Third, long rise time from seconds to minute are observed in the temporal evolution graph due to non-resonant ground state absorption which leads to slow accumulation of Ln^{3+} in the key reservoir state.

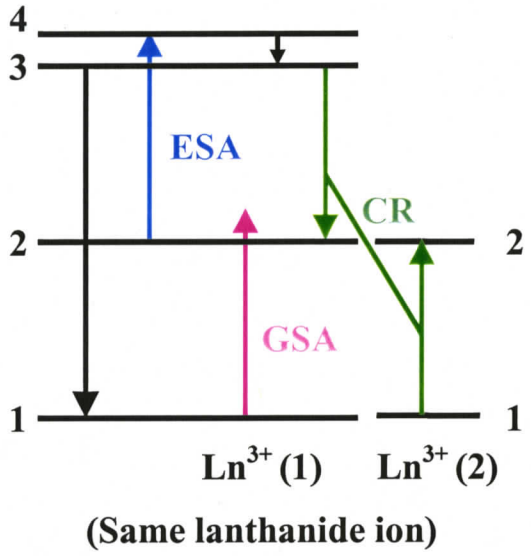

Figure 2.8. Schematic diagram of photon-avalanche process

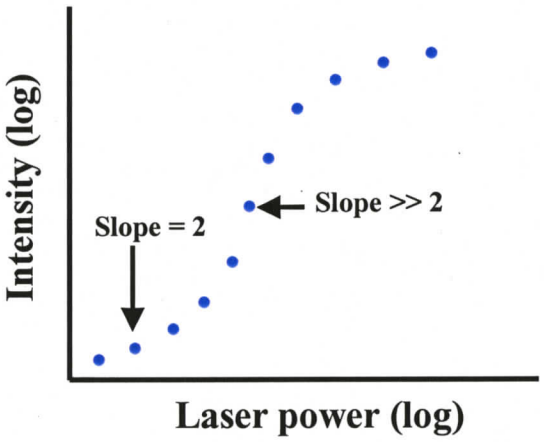

Figure 2.9. Schematic illustration of the variation of up-conversion fluorescence intensity with pump power for photon-avalanche process.

Scheife *et al.*[47] have observed red emission from Pr^{3+} through a photon-avalanche up-conversion process from $LiLuF_4:Pr^{3+}$ and $LiYF_4:Pr^{3+}$ single crystals. Auzel *et al.* have reported the generation of green emission through a photon-avalanche process in Er^{3+}-doped $LiYF_4$ single crystals[48] and ZBLAN (ZrF_4-BaF_2-LaF_3-AlF_3-NaF) fiber

materials,[49,50] which are potential materials for up-conversion lasers. These materials were excited with 579, 690, and 700 nm lasers, respectively. Chadeyron *et al.*[51] have demonstrated violet emission from Nd^{3+} through photon-avalanche process from $LiKYF_5$ single crystals excited at 603 nm. The photon-avalanche process in various materials was summarized in a recent review.[19]

Although photon-avalanche mechanisms can be relatively efficient, they suffer from a number of drawbacks. Maximum output is limited because of the weak ground state absorption, and high pump fluxes are usually needed to reach the threshold condition. In addition, because many looping cycles are required to achieve avalanche, the rise time in the temporal evolution of the up-conversion emission is generally much longer (up to minutes) than the lifetimes of any of the excited states involved. This can be a disadvantage in lighting and display applications because it will take seconds or longer to reach maximum output. In order to address the drawbacks of photon-avalanche process a potentially more efficient up-conversion mechanism is described in chapter 4.

2.3.4.1. Sensitized photon-avalanche

The classical photon-avalanche which is described above occurs within the same lanthanide ions. In sensitized photon-avalanche up-conversion process, the cross relaxation happens between two ions of a different type instead of same ions. It was first investigated in Tm^{3+}-Ho^{3+} system by Brenier *et al.*.[52,53] A complex process of cross-relaxation between two Tm^{3+} ions together with a transfer from excited Tm^{3+} to Ho^{3+} has been demonstrated. The $^3H_4$ level of Tm^{3+} is excited non-resonantly followed by a cross-relaxation within two Tm^{3+} ions which populates the $^3F_4$ level of Tm^{3+}. Subsequently, it

transfers its energy to $^5I_7$ level of Ho^{3+} ion and Ho^{3+} is further excited to $^5S_2$ level by resonant excited state absorption from which the green emission takes. Huber *et al.*[54] demonstrated a similar type of avalanche process in Yb^{3+}-Pr^{3+} doped systems. In this system, Yb^{3+} is excited to $^2F_{5/2}$ level by non-resonant excitation and it transfers its energy to reservoir level of $^1G_4$ level of Pr^{3+} followed by a resonant excited state absorption to $^3P_0$ level. The cross relaxation between two Pr^{3+} ions feeds the reservoir level $^1G_4$ of Pr^{3+} ion and back transfers to Yb^{3+} ion which again feeds the $^1G_4$ level of Pr^{3+} ion. Lupei[55] has demonstrated another type of sensitized photon-avalanche (Figure 2.10) in which the cross-relaxation (Pr^{3+}-Yb^{3+}) populates the intermediate level of sensitizer ion (Yb^{3+}). Immediately following this process, the excited sensitizer ion gives back its energy to the neighbouring acceptor ion (Pr^{3+}) to populate the key reservoir level and the looping starts. Lahoz *et al.*[56] have reported similar sensitized photon-avalanche mechanism in Ho^{3+}-Yb^{3+} co-doped fluoroindate glasses. They have estimated that the efficiency of sensitized photon-avalanche is three-fold higher than the photon-avalanche process.

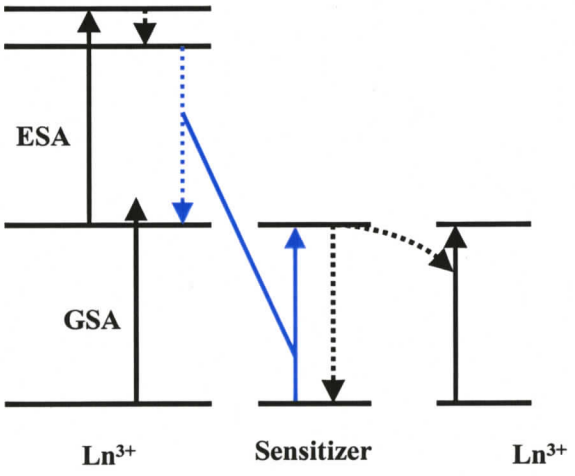

Figure 2.10. Schematic diagram of sensitized photon-avalanche process

2.3.5. Co-operative up-conversion process

Co-operative up-conversion process is different from the above GSA/ESA, ET and PA up-conversion processes. In co-operative up-conversion two excited donor ions simultaneously transfer their energy to the acceptor ion followed by its emission in the visible region (Figure 2.11) This co-operative energy transfer thus results in up-conversion of energy and it is a three-ion process. This coupling between three ions is different from more traditional up-conversion processes that require two-ion interactions. This event is also different from multiphoton absorption processes, which occur in a medium through the simultaneous absorption of two or more photons via a non-stationary, virtual quantum mechanical state, usually requiring high excitation densities. The co-operative up-conversion process described in this report does not require such high excitation densities.

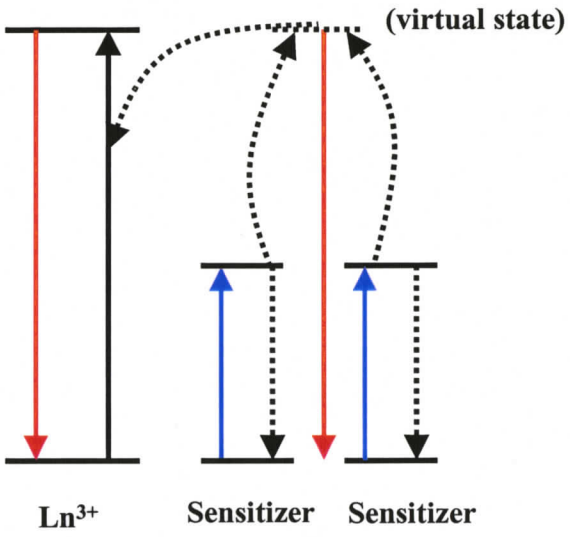

Figure 2.11. Schematic diagram of co-operative up-conversion process

Co-operative up-conversion is generally reported in materials doped with Eu^{3+}/Tb^{3+} ions co-doped with Yb^{3+} ions. In these materials, the energy transfer from excited Yb^{3+} ions to Eu^{3+}/Tb^{3+} ions occurs via co-operative up-conversion process. This is because of the nature of the long-lived (upto few milliseconds) excited state of Yb^{3+} ion which can transfer its energy to another excited Yb^{3+} ion (which is also excited simultaneously from the ground state) to promote it to a virtual level. Only a few groups have studied the generation of green emission through co-operative energy transfer in Yb^{3+}-Tb^{3+} co-doped silica, fluoroindate, and tellurite sol-gel glasses. This up-conversion process was first identified by Nakazawa and Shinoya in 1970.[57] Güdel and co-workers have studied the mechanism of generation of green emission through co-operative up-conversion in $SrCl_2$:Yb,Tb[58,59] and $Cs_3Tb_2Br_9$:Yb[60] single crystals. Maciel *et al.*[61] have studied the co-operative energy transfer from Yb^{3+} ion to Eu^{3+} ions in sol-gel derived silica glasses. Ostermayer *et al.*[62] have estimated that co-operative up-conversion processes are ~130 times weaker than the efficient traditional up-conversion energy transfer process (Er-Yb).

2.4. Luminescence of lanthanide ions in different environments

2.4.1. Luminescence of lanthanide complexes

Luminescence of lanthanide ion in various organic solvents, aqueous solvents and polymers have been studied in detail by many research groups[63-65] including our group.[66,67] However, they suffer from a drawback of luminescence quenching by organic ligands, especially in the NIR region. Our group has studied terphenyl- and calix[4]arene-

based lanthanide complexes in detail.[68] A sensitizer which is attached to these ligands can transfer its energy to a lanthanide ion and can potentially be used in high through-put biological applications, such as immunoassays and biolabels. Lanthanide ions which emit in the visible region such as Eu^{3+} and Tb^{3+} ion based organic complexes have quantum yield of several tens of % with lifetime in milliseconds.[67,69] However, NIR emitting ions (Nd^{3+} and Er^{3+}) have much lower quantum yields with lifetimes in the few microseconds range.[70]

2.4.2. Luminescence of lanthanide-doped inorganic materials

One way to circumvent the above drawbacks is to increase the distance between the lanthanide ion and ligand. This can be achieved by doping the lanthanide ion into inorganic nanomaterials stabilised by organic sensitizers and doping the lanthanide ions into semiconductor matrix. Lanthanide-doped inorganic materials are promising materials in various optical applications such as solid state lasers,[13,14] optical amplifiers,[8,15] and lighting purposes.[12] The optical properties of lanthanide ions are dependent on the phonon energy of materials. Various low-phonon glass materials such as chalcogenide glasses (400 cm^{-1}), fluoride glasses (550 cm^{-1}), and silica glasses (1100 cm^{-1}) have been successfully doped with lanthanide ion with improved optical properties. However, they suffer from a draw back of clustering of ion at higher concentrations which leads to self-quenching. Self-quenching occurs between two identical ions due to interaction of an excited ion with another ion in the ground state. Similarly, inorganic materials like YVO_4,[71] LaF_3,[72] and YAG[14] doped with lanthanide ions have successfully been used in various optical applications. Eventhough these materials are successfully used in optical

applications, the processing of these materials is difficult. These issues have successfully been addressed by lanthanide-doped nanoparticles.

2.4.3. Lanthanide-doped nanoparticles

Nanoparticles are defined as crystalline clusters, consisting of a few hundred to a few hundred thousand atoms which are confined to a size of a few nanometers (1-100 nm). The nanoparticles are having unique chemical and physical properties when compared to their bulk materials because of their small size, and these properties are often dominated by their surfaces, not by their bulk volume. Colloidal gold was first prepared by Faraday in 1857.[73] There are different methods such as colloidal synthesis, sol-gel method, combustion method to prepare nanoparticles. Most of the nanoparticles are prepared by colloidal synthesis route and they are stabilised by charged ligands to minimize the aggregation of nanoparticles. A schematic representation of a nanoparticles stabilsed by ligands is given in the Figure 2.12. Nanoparticles are having improved optical properties such as, pronounced quantum effects for quantum dots (QDs), surface scattering effects for gold and silver nanoparticles, and luminescent efficiencies (for both QDs and lanthanide-based NPs) that are superior to organic fluorophores which makes the nanoparticles as potential candidates for various optical applications.

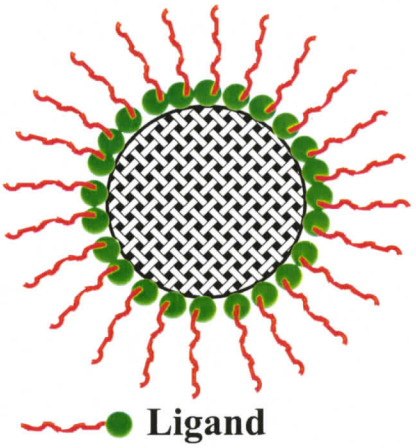

Figure 2.12. Schematic representation of a nanoparticle

In this thesis, we focus mainly on lanthanide-doped nanoparticles and study their optical properties in sol-gel matrices. Many research groups including our group have investigated the optical properties of lanthanide ions in detail in various nanoparticles matrices such as oxides,[74,75] fluorides,[39,76] phosphates,[9,77] vanadates,[78] and semiconductor nanoparticles.[79] Most of the lanthanide-doped oxide and silicate nanoparticles such as Y_2O_3,[34,80] Lu_2O_3,[28] $Gd_2Ga_5O_{12}$,[37] ZnO,[27] ZrO_2,[22,81] $BaTiO_3$,[82] and Y_2SiO_5[83,84] nanocrystals have been prepared at temperatures above 800 °C. Capobianco *et al.* have investigated the effect of co-doping of Yb^{3+} ion with Er^{3+} ion,[35] concentration of Er^{3+} and Yb^{3+} ions in up-conversion of Y_2O_3 nanocrystals[35,80] prepared by propellant synthesis. They observed that the efficiency of up-conversion has been improved by co-doping with Yb^{3+} ion and increase in the red emission when increase in the concentration of Er^{3+} and Yb^{3+} ions. They have also studied up-conversion properties of effect of co-doping of Er^{3+} and Ho^{3+} ions in Lu_2O_3[28] and $Gd_2Ga_5O_{12}$[38] nanomaterials (~20 nm). Prasad *et al.* have demonstrated the generation of green and red emission through up-conversion of Er^{3+} in ZrO_2[22,81] and $BaTiO_3$[82] nanocrystals prepared by sol-gel synthesis. Rosa and his groups

have shown bright green emission from Yb^{3+}/Ho^{3+}-doped ZrO_2 nanocrystals[85] and green/red emission from Yb^{3+}/Er^{3+}-doped ZrO_2 nanocrystals[75] (~80 nm) prepared by a sol-gel synthesis. Patra *et al.*[86] have demonstrated bright blue emission from Yb^{3+}/Tm^{3+}-doped ZrO_2 nanocrystals prepared by sol-gel synthesis. These nanocrystals showed very impressive up-conversion properties, but they are not soluble in any organic solvents because they are not capped with any organic ligand. In order to apply lanthanide-doped nanoparticles into polymer-based optical waveguides, LEDs, and bioapplications the nanoparticles should be capped with organic ligands which can be soluble in organic or aqueous solvents.

Güdel *et al.*[39] have demonstrated bright red, green, and blue emission through up-conversion from highly dispersible Er^{3+} and Tm^{3+}-doped $NaYF_4/NaGdF_4$ nanoparticles prepared at 300 °C in high boiling solvents. Similarly, Capobianco *et al.*.[87] have also shown bright red, green, and blue emission from the same material prepared by thermal decomposition of lanthanide trifluoroacetate precursors. Yi *et al.*[88] have demonstrated red, green, and blue up-conversion from highly dispersible Yb^{3+}/Ho^{3+}, Yb^{3+}/Er^{3+}, and Yb^{3+}/Tm^{3+}-doped LaF_3 nanoparticles respectively. Haase *et al.*[77] have demonstrated the bright green/red and blue up-conversion from $LuPO_4$ nanoparticles doped with Yb^{3+}/Er^{3+} and Yb^{3+}/Tm^{3+} ions respectively. They have also demonstrated the increase in the quantum yield of Tb^{3+} upto 70% in $CePO_4/LaPO_4$ core-shell nanoparticles.[89] Our group has shown NIR emissions from highly dispersible LaF_3 nanoparticles doped with $Er^{3+}/Nd^{3+}/Ho^{3+}$ ions[76] and $LaPO_4$ nanoparticles doped with $Er^{3+}/Nd^{3+}/Yb^{3+}$ ions[9] prepared at low temperatures. We have also demonstrated the sensitized emission occurs from lanthanide ions in highly dispersible $LaVO_4$ nanoparticles by exciting VO_4^{3-} group

in the ultraviolet region.[78] Synthesis of water soluble $LaF_3:Ln^{3+}$ nanoparticles was also reported by us.[90,91] Apart from this, many research groups have synthesised highly dispersible lanthanide-doped nanoparticles which emits in the visible region.

Doping of lanthanide ions into semiconductor nanoparticles could have a number of potential advantages over the doping into insulator host nanoparticles. Lanthanide ions in these materials may be excited through energy transfer from semiconductor materials which could overcome the drawback of the low absorption cross-section of the lanthanide ion and it could facilitate the possibility of electrical excitation. Many research groups have attempted to dope lanthanide ions into dispersible II-VI semiconductor nanoparticles, however, there is no convincing proof available (more in chapter 5). Okamoto *et al.* have reported the luminescence from $CdS:Eu^{3+}$ through energy transfer from CdS to Eu^{3+} ion. Later Bol *et al.*[92] have redone the experiments of Okamoto *et al.* and other research groups and concluded that the lanthanide ions are not incorporated in the II-VI semiconductor nanoparticles. However, this principle has been demonstrated in bulk semiconductors. Our group[79] has shown the energy transfer from semiconductor TiO_2 matrix to lanthanide ions ($Eu^{3+}/Nd^{3+}/Er^{3+}/Yb^{3+}$) in highly dispersible TiO_2 nanoparticles, however the quantum yield is very low. There is clearly a need for a general method to incorporate lanthanide ions into semiconductor matrix, which is described in chapter 5.

2.5. Sol-gel synthesis

The sol-gel process is a promising method for the preparation of bulk materials, nanomaterials, and thin films used in integrated optics (IO) circuits because of the

possibility of modification of refractive index of the material. Sol-gel processing of inorganic ceramic and glass materials was first investigated by Ebelman[93,94] and Graham[95] in the mid 1800s. They have demonstrated the acid hydrolysis of tetraethyl orthosilicate (TEOS) which gives SiO_2 glass-like material. In 1950s and 1960 Roy *et al.*[96,97] have prepared novel ceramic materials with Al, Si, Ti, Zr, etc. with high level of chemical homogeneity by sol-gel methods. In 1968, Stöber *et al.*[98] have shown the hydrolysis of TEOS by NH_4OH to yield silica beads, with uniform size, which is called as Stöber synthesis. Later on, many research groups have demonstrated the controlled hydrolysis of alkoxides to produce un-doped/doped ZrO_2,[22,81] TiO_2,[82,99,100] SiO_2,[91] Al_2O_3,[101] $BaTiO_3$[82] thin films and nanocrystals.

Sols are dispersions of colloidal particles with diameter of 1-100 nm in a liquid. The sols are polymerized through the removal of the stabilizing components and produce a gel. A gel is interconnected, rigid network with pores of submicrometer dimensions and polymeric chains whose average length is greater than a micrometer. The major advantages of the process are its simplicity and its ability to control the purity and homogeneity of the final material on a molecular level. The method also offers the possibility of modifying the refractive index, phonon energy, and transparency of a material by choosing suitable matrices like SiO_2, TiO_2, ZrO_2, Al_2O_3, GeO_2 etc., either individually or in combination. Such matrices are potential candidates for making planar waveguides, fiber amplifiers, and up-conversion devices, when doped with trivalent lanthanide ions.[75,86] However, improvements are still needed to optimize their performance. The most commonly used lanthanide ion for these applications is Er^{3+}, as it provides amplification in the 1550 nm communication window, through its $^4I_{13/2} \rightarrow {}^4I_{15/2}$

transition. It is in general desirable to have a high quantum yield and an increased line width for this transition, to enable those materials to be used for broad-band near-infrared amplification. The three main factors which decide the performance characteristics of such lanthanide ion containing materials are the phonon energy of the host, the proximity of the OH groups present in the matrix to the lanthanide ions, and clustering of lanthanide ions. For example, a high phonon energy of the host matrix incorporated with Er^{3+} ion favours the non-radiative relaxation of the $^4I_{13/2}$ excited state, thereby reducing its lifetime and quantum yield of the $^4I_{13/2} \rightarrow {}^4I_{15/2}$ transition. The OH groups, an inherent result of sol-gel process, quench the excited state of the lanthanide ions by dipole-dipole interaction and the proximity of the OH groups to the lanthanide ions, results in a much higher extent of quenching. Finally, clustering of the lanthanide ions reduce the excited state lifetime by concentration quenching. Many reports are available regarding ways to improve the luminescence characteristics of such materials. These mainly include the works of Biswas *et al.*[102,103] and Tanabe *et al.*[104] on the sol-gel glasses and glass ceramics containing Er^{3+} ions. These materials have only limited applications as they need to be melted at higher temperature to draw them into fibers. Fiber amplifiers are less convenient for integrated optics because of their increased length and extensive research is going on to replace them with planar waveguide amplifiers.[105] A lifetime of 17 ms for the $^4I_{13/2}$ level of Er^{3+} was reported by Slooff *et al.*[106] for Er^{3+} ion implanted silica colloidal particles having sizes in the range of 240-360 nm and annealed over the temperature range of 700-900 °C. This was attributed to the decreased OH concentration in these materials. The disadvantage of this method is that the ion implantation is a small area, low throughput procedure. In this thesis (chapter 3, 4, and 5) a general method, from readily available

starting materials, that combines the advantage of the improved luminescent properties of Ln^{3+}-doped LaF_3 nanoparticles and the simplicity of making thin films using sol-gel method, is demonstrated.

2.6. White light generation from lanthanide ions

Three modern house hold applications that use lanthanide ions to generate white light are the fluorescent light tubes, the cathode ray tube in televisions/computer monitors, and plasma displays. In these applications lanthanide ions are used to convert high energetic radiation into visible light. To produce white light it is necessary to generate blue, green, and red light simultaneously. In the first commercially, available luminescent tubes a mixture of $MgWO_4$ (blue emission), and $(Zn, Be)_2SiO_4:Mn^{2+}$ (green and red) was used. Later on, the so-called tricolour lamp was developed which contains three phosphors $BaMgAl_{10}O_{17}:Eu^{2+}$ (blue), $GdMgB_5O_{10}:Ce^{3+}$, Tb^{3+} or $LaPO_4:Ce^{3+}$, Tb^{3+} (green) and $Y_2O_3:Eu^{3+}$ (red). The overall efficiency of generation of white light from fluorescent light tubes is still low (~30%). All the above white lights have been generated by conversion of UV light (down-conversion). Light-emitting diodes such as organic light-emitting diodes (OLEDs)[107-110] and polymer light-emitting diodes (PLEDs).[111-113] are being developed with some major advances over the last few years. However, the generation of white light from OLEDs and PLEDs has proven to be challenging because, of their inefficiency, bias dependent colour variation, and long-term instability. These issues are addressed further in chapter 3.

2.6. Biolabels

The rapid development of biological science has fueled growing demands to analyse biomolecules such as polypeptides, proteins, and nucleic acids during the past decades, resulting in the development of various biological analytical systems like biosensors. There are various widely used biolabeling techniques such as radioimmunoassay, enzyme-catalysed reactions, bio/chemiluminescence, and fluorescence in which fluorescence labeling is a promising one. Materials such as organic dyes, fluorescent proteins, and lanthanide chelates are most commonly used in biolabels because they are small and highly water soluble (at high salt concentrations) ãs well as the ease of their usage and the existence of standard protocols for their bioconjugation. Organic dyes such as flouresceins[114] and rhodamines[115] are widely used to label proteins. The fluorescein dye fluorescein-5-isothiocyanate (FITC) is a traditional dye used for labeling techniques because of its high absorption, high quantum yield, and aqueous solubility. Moreover, FITC can be excited with an argon ion laser line which is the excitation source in many confocal microscopes. Similarly, rhodamines are very popular in labeling. However, they suffer from some drawbacks such as small stokes shift, poor chemical stability, poor photostability, and short luminescence lifetime. The inherent short-luminescence lifetime may overlap with the spontaneous background emission sources (natural fluorescence of biomolecules such as proteins is within 1-10 ns). The next popular material is green fluorescent protein (GFP)[116] which is isolated from the jelly fish *Aequorea Victoria*. GFP has been used in numerous applications including biological labels to track and quantify individual or multiple protein species, as probes to monitor protein-protein interactions, and as biosensors to describe biological events and

signals. However, they have some limitations such as self-aggregation which may lead to toxicity and short luminescence lifetime.

Lanthanide chelates such as cryptates[117] and terpyridine[118,119] are an important group of luminescence materials used for biolabeling because of their long live luminescence lifetime (microseconds to milliseconds). However, their photostability and quantum yield in the NIR region are remaining as major obstacles. Various semiconductor quantum dots (CdSe, CdS, CdTe, PbS, and PbSe) display high photostability, size-dependant emission, high quantum yields, and narrow emission bandwidth and they have successfully been applied in biological applications. Bawendi *et al.*[120,121] and Alivisatos *et al.*[122,123] have synthesised highly luminescent quantum dots which can potentially be used as biolabel. However, they are still controversial because of their inherent toxicity and chemical instability. In order to address these key issues, the development of an alternative biomaterial via lanthanide-doped nanoparticle is gaining popularity due to their unique luminescent properties such as sharp absorption and emission lines, high quantum yield, long lifetimes, and superior photostability. Silica-coated lanthanide-doped nanoparticles have been developed as potential biolabel which is discussed in chapter 6.

2.7 Summary

In this chapter, a broad outlook of optical properties of lanthanide ions has been discussed with the focus on their applications as white light sources and biolabels. Various up-conversion mechanisms such as GSA/ESA, ET, and PA and their advantages

and drawbacks are discussed in detail with examples. Photon-avalanche up-conversion mechanism is more efficient than the other two however, it has some drawbacks such as inefficient ground state absorption and it needs high pump flux to reach threshold. A avalanche-type up-conversion process with efficient ground state absorption and less laser pump flux would be ideal to achieve higher efficiencies. The research on the generation of white light is growing because the general lighting devices consumes a lot of energy. Despite the major advances in OLEDs, PLEDs, and ILEDs there is still a need to develop alternate white light sources with stable photocycle, cheap excitation source and easy/cost effective fabrication. Therefore, in this thesis generation of white light is investigated in detail. The historical development of biolabeling techniques has been described in this chapter. The major disadvantages of different existing biolabels are their weak photostability, toxicity, and broad absorption/emission band. Therefore a biolabel, addressing the major key issues have been investigated in thesis.

References

(1) *CRC Handbook of Chemistry and Physics 77th ed.,* Baco Raton, Florida, USA, **1996-1997**.

(2) Jones, A. P.; Wall, F., *Rare Earth Minerals: Chemistry, Orgin, and Ore Deposites,* Chapman and Hall, London, **1996**.

(3) Cotton, S., *Lanthanides and Actinides,* Macmillan Education, Basingstoke, **1991**.

(4) Hou, Z. M.; Luo, Y. J.; Li, X. F. *J. Organomet. Chem.* **2006**, *691*, 3114.

(5) Yuan, F. G.; Yang, J.; Xiong, L. F. *J. Organomet. Chem.* **2006**, *691*, 2534.

(6) Parac-Vogt, T. N.; Deleersnyder, K.; Binnemans, K. *Eur. J. Org. Chem.* **2005**, 1810.

(7) Arkhangel'skaya, Z. P.; Demidov, A. I.; Loginova, M. M.; Kas'yan, T. B.; Apollonova, E. V. *Russ. J. Appl. Chem.* **2005**, *78*, 1430.

(8) Polman, A.; van Veggel, F. C. J. M. *J. Opt. Soc. Am. B* **2004**, *21*, 871.

(9) Hebbink, G. A.; Stouwdam, J. W.; Reinhoudt, D. N.; van Veggel, F. C. J. M. *Adv. Mater.* **2002**, *14*, 1147.

(10) Louis, U.; Bazzi, R.; Marquette, C. A.; Bridot, J. L.; Roux, S.; Ledoux, G.; Mercier, B.; Blum, L.; Perriat, P.; Tillement, O. *Chem. Mater.* **2005**, *17*, 1673.

(11) Wang, F.; Tan, W. B.; Zhang, Y.; Fan, X. P.; Wang, M. Q. *Nanotechnol.* **2006**, *17*, R1.

(12) Thornton, W. A. *J. Opt. Soc. Am.* **1971**, *61*, 1155.

(13) Zolotoverkh, I. I.; Lariontsev, E. G. *Quant. Electron.* **2004**, *34*, 727.

(14) Kalisky, Y.; Kravchik, L.; Kokta, M. R. *Opt. Mater.* **2004**, *24*, 607.

(15) Polman, A. *Physica B* **2001**, *300*, 78.

(16) Kasha, M. *Discuss. Faraday Soc.* **1950**, *9*, 14.

(17) Carnall, W. T.; Goodman, G. L.; Rajnak, K.; Rana, R. S. *J. Chem. Phys.* **1989**, *90*, 3443.

(18) Wright, J. C. *Top. Appl. Phys.* **1976**, *15*, 239.

(19) Auzel, F. *Chem. Rev.* **2004**, *104*, 139.

(20) Lim, S. F.; Riehn, R.; Ryu, W. S.; Khanarian, N.; Tung, C. K.; Tank, D.; Austin, R. H. *Nano Lett.* **2006**, *6*, 169.

(21) Mehta, A.; Thundat, T.; Barnes, M. D.; Chhabra, V.; Bhargava, R.; Bartko, A. P.; Dickson, R. M. *Appl. Optics* **2003**, *42*, 2132.

(22) Patra, A.; Friend, C. S.; Kapoor, R.; Prasad, P. N. *J. Phys. Chem. B* **2002**, *106*, 1909.

(23) Zhang, H. X.; Kam, C. H.; Zhou, Y.; Han, X. Q.; Buddhudu, S.; Xiang, Q.; Lam, Y. L.; Chan, Y. C. *Appl. Phys. Lett.* **2000**, *77*, 609.

(24) Soo, Y. L.; Huang, S. W.; Ming, Z. H.; Kao, Y. H.; Smith, G. C.; Goldburt, E.; Hodel, R.; Kulkarni, B.; Veliadis, J. V. D.; Bhargava, R. N. *J. Appl. Phys.* **1998**, *83*, 5404.

(25) Balda, R.; Fernandez, J.; de Ocariz, I. S.; Voda, M.; Garcia, A. J.; Khaidukov, N. *Phys. Rev. B* **1999**, *59*, 9972.

(26) Fernandez, J.; Sanz, M.; Mendioroz, A.; Balda, R.; Chaminade, J. P.; Ravez, J.; Lacha, L. M.; Voda, M.; Arriandiaga, M. A. *J. Alloys Compd.* **2001**, *323*, 267.

(27) Wang, X.; Kong, X. G.; Shan, G. Y.; Yu, Y.; Sun, Y. J.; Feng, L. Y.; Chao, K. F.; Lu, S. Z.; Li, Y. J. *J. Phys. Chem. B* **2004**, *108*, 18408.

(28) Capobianco, J. A.; Vetrone, F.; Boyer, J. C.; Speghini, A.; Bettinelli, M. *Opt. Mater.* **2002**, *19*, 259.

(29) Capobianco, J. A.; Vetrone, F.; Boyer, J. C.; Speghini, A.; Bettinelli, M. *J. Phys. Chem. B* **2002**, *106*, 1181.

(30) Balda, R.; Fernandez, J.; de Ocariz, I. S.; Adam, J. L.; Mendioroz, A.; Montoya, E. *Opt. Mater.* **1999**, *13*, 159.

(31) Fernandez, J.; Balda, R.; Mendioroz, A.; Sanz, M.; Adam, J. L. *J. Non-Cryst. Sol.* **2001**, *287*, 437.

(32) Auzel, F. E. *Proc. IEEE* **1973**, *61*, 758.

(33) Förster, T. *Ann. Phys.* **1948**, *2*, 55.

(34) Vetrone, F.; Boyer, J. C.; Capobianco, J. A.; Speghini, A.; Bettinelli, M. *J. Phys. Chem. B* **2003**, *107*, 1107.

(35) Vetrone, F.; Boyer, J. C.; Capobianco, J. A.; Speghini, A.; Bettinelli, M. *J. Appl. Phys.* **2004**, *96*, 661.

(36) Pandozzi, F.; Vetrone, F.; Boyer, J. C.; Naccache, R.; Capobianco, J. A.; Speghini, A.; Bettinelli, M. *J. Phys. Chem. B* **2005**, *109*, 17400.

(37) Boyer, J. C.; Vetrone, F.; Capobianco, J. A.; Speghini, A.; Bettinelli, M. *Chem. Phys. Lett.* **2004**, *390*, 403.

(38) Boyer, J. C.; Vetrone, F.; Capobianco, J. A.; Speghini, A.; Zambelli, M.; Bettinelli, M. *J. Lumin.* **2004**, *106*, 263.

(39) Heer, S.; Kompe, K.; Güdel, H. U.; Haase, M. *Adv. Mater.* **2004**, *16*, 2102.

(40) Kramer, K. W.; Biner, D.; Frei, G.; Güdel, H. U.; Hehlen, M. P.; Luthi, S. R. *Chem. Mater.* **2004**, *16*, 1244.

(41) Suyver, J. F.; Aebischer, A.; Biner, D.; Gerner, P.; Grimm, J.; Heer, S.; Kramer, K. W.; Reinhard, C.; Güdel, H. U. *Opt. Mater.* **2005**, *27*, 1111.

(42) Suyver, J. F.; Grimm, J.; van Veen, M. K.; Biner, D.; Kramer, K. W.; Güdel, H. U. *J. Lumin.* **2006**, *117*, 1.

(43) Aebischer, A.; Heer, S.; Biner, D.; Kramer, K.; Haase, M.; Güdel, H. U. *Chem. Phys. Lett.* **2005**, *407*, 124.

(44) Aebischer, A.; Hostettler, M.; Hauser, J.; Kramer, K.; Weber, T.; Güdel, H. U.; Buergi, H. B. *Angew. Chem. Int. Ed.* **2006**, *45*, 2802.

(45) Chivian, J. S.; Case, W. E.; Eden, D. D. *Appl. Phys. Lett.* **1979**, *35*, 124.

(46) Krasutsky, N. J.; Case, W. E.; Chivian, J. S. *J. Appl. Phys.* **1979**, *50*, 3142.

(47) Scheife, H.; Huber, G.; Heumann, E.; Bar, S.; Osiac, E. *Opt. Mater.* **2004**, *26*, 365.

(48) Auzel, F.; Chen, Y. H. *J. Lumin.* **1995**, *65*, 45.

(49) Auzel, F.; Chen, Y. H.; Meichenin, D. *J. Lumin.* **1994**, *60-1*, 692.

(50) Chen, Y. H.; Auzel, F. *Electron. Lett.* **1994**, *30*, 1602.

(51) Chadeyron, G.; Mahiou, R.; Joubert, M. F.; Guy, S.; Jacquier, B.; Kaminskii, A. A.; Khaidukov, N. M. *Phys. Stat. Sol. A-Appl. Res.* **1999**, *171*, 597.

(52) Brenier, A.; Garapon, C.; Madej, C.; Pedrini, C.; Boulon, G. *J. Phys. IV* **1994**, *4*, 431.

(53) Brenier, A.; Courrol, L. C.; Pedrini, C.; Madej, C.; Boulon, G. *J. Lumin.* **1994**, *58*, 284.

(54) Kuck, S.; Diening, A.; Heumann, E.; Mix, E.; Sandrock, T.; Sebald, K.; Huber, G. *J. Alloys. Compd.* **2000**, *300*, 65.

(55) Lupei, V. *Spectrochim. Acta, Part A* **1998**, *54*, 1615.

(56) Lahoz, F.; Martin, I. R.; Briones, A. *J. Appl. Phys.* **2004**, *95*, 2957.

(57) Nakazawa, E.; Shionoya, S. *Phys. Rev. Lett.* **1970**, *25*, 1710.

(58) Salley, G. M.; Valiente, R.; Güdel, H. U. *J. Phys.: Condens. Matter* **2002**, *14*, 5461.

(59) Salley, G. M.; Valiente, R.; Güdel, H. U. *J. Lumin.* **2001**, *94*, 305.

(60) Salley, G. M.; Valiente, R.; Güdel, H. U. *Phys. Rev. B* **2003**, *67*, 134111.

(61) Maciel, G. S.; Biswas, A.; Prasad, P. N. *Opt. Commun.* **2000**, *178*, 65.

(62) Ostermay, F. W.; Vanuiter, L. G. *Phys. Rev. B* **1970**, *1*, 4208.

(63) Parker, D.; Gareth, W. *J. Chem. Soc., Daton Trans.* **1996**, *18*, 3613.

(64) Saraidarov, T.; Reisfeld, R.; Pietraszkiewicz, M. *Chem. Phys. Lett.* **2000**, *330*, 515.

(65) Froidevaux, P.; Harrowfield, J. M.; Sobolev, A. N. *Inorg. Chem.* **2000**, *39*, 4678.

(66) Slooff, L. H.; Polman, A.; Klink, S. I.; Grave, L.; van Veggel, F. C. J. M.; Hofstraat, J. W. *J. Opt. Soc. Am. B* **2001**, *18*, 1690.

(67) Klink, S. I.; Grave, L.; Reinhoudt, D. N.; van Veggel, F. C. J. M.; Werts, M. H. V.; Geurts, F. A. J.; Hofstraat, J. W. *J. Phys. Chem. A* **2000**, *104*, 5457.

(68) Hebbink, G. A.; Klink, S. I.; Alink, P.; van Veggel, F. C. J. M. *Inorg. Chim. Acta* **2001**, *323*, 171.

(69) Klink, S. I.; Hebbink, G. A.; Grave, L.; Peters, F. G. A.; Van Veggel, F. C. J. M.; Reinhoudt, D. N.; Hofstraat, J. W. *Eur. J. Org. Chem.* **2000**, 1923.

(70) Hofstraat, J. W.; Wolbers, M. P. O.; van Veggel, F. C. J. M.; Reinhoudt, D. N.; Werts, M. H. V.; Verhoeven, J. W. *J. Fluores.* **1998**, *8*, 301.

(71) Brecher, C.; Samelson, H.; Lempicki, A.; Riley, R.; Peters, T. *Phys. Rev.* **1967**, *155*, 178.

(72) Dekker, R.; Klunder, D. J. W.; Borreman, A.; Diemeer, M. B. J.; Worhoff, K.; Driessen, A.; Stouwdam, J. W.; van Veggel, F. C. J. M. *Appl. Phys. Lett.* **2004**, *85*, 6104.

(73) Faraday, M. *Philos. Trans. R. Soc.* **1857**, *147*, 145.

(74) Capobianco, J. A.; Boyer, J. C.; Vetrone, F.; Speghini, A.; Bettinelli, M. *Chem. Mater.* **2002**, *14*, 2915.

(75) De la Rosa, E.; Diaz-Torres, L. A.; Salas, P.; Rodriguez, R. A. *Opt. Mater.* **2005**, *27*, 1320.

(76) Stouwdam, J. W.; van Veggel, F. C. J. M. *Nano Lett.* **2002**, *2*, 733.

(77) Heer, S.; Lehmann, O.; Haase, M.; Güdel, H. U. *Angew. Chem. Int. Ed.* **2003**, *42*, 3179.

(78) Stouwdam, J. W.; Raudsepp, M.; van Veggel, F. C. J. M. *Langmuir* **2005**, *21*, 7003.

(79) Stouwdam, J. W.; van Veggel, F. C. J. M. *Chemphyschem* **2004**, *5*, 743.

(80) Vetrone, F.; Boyer, J. C.; Capobianco, J. A.; Speghini, A.; Bettinelli, M. *Chem. Mater.* **2003**, *15*, 2737.

(81) Patra, A. *Chem. Phys. Lett.* **2004**, *387*, 35.

(82) Patra, A.; Friend, C. S.; Kapoor, R.; Prasad, P. N. *Chem. Mater.* **2003**, *15*, 3650.

(83) Hu, C. H.; Sun, C. L.; Li, J. F.; Li, Z. S.; Zhang, H. Z.; Jiang, Z. K. *Chem. Phys.* **2006**, *325*, 563.

(84) Sun, C. L.; Li, J. F.; Hu, C. H.; Jiang, H. M.; Jiang, Z. K. *Eur. Phys. J. D* **2006**, *39*, 303.

(85) De la Rosa, E.; Salas, P.; Desirena, H.; Angeles, C.; Rodriguez, R. A. *App. Phys. Lett.* **2005**, *87*.

(86) Patra, A.; Saha, S.; Alencar, M. A. R. C.; Rakov, N.; Maciel, G. S. *Chem. Phys. Lett.* **2005**, *407*, 477.

(87) Boyer, J. C.; Vetrone, F.; Cuccia, L. A.; Capobianco, J. A. *J. Am. Chem. Soc.* **2006**, *128*, 7444.

(88) Yi, G. S.; Chow, G. M. *J. Mater. Chem.* **2005**, *15*, 4460.

(89) Kompe, K.; Borchert, H.; Storz, J.; Lobo, A.; Adam, S.; Möller, T.; Haase, M. *Angew. Chem. Int. Ed.* **2003**, *42*, 5513.

(90) Diamente, P. R.; Burke, R. D.; van Veggel, F. C. J. M. *Langmuir* **2006**, *22*, 1782.

(91) Sudarsan, V.; Sivakumar, S.; van Veggel, F. C. J. M.; Raudsepp, M. *Chem. Mater.* **2005**, *17*, 4736.

(92) Bol, A. A.; van Beek, R.; Meijerink, A. *Chem. Mater.* **2002**, *14*, 1121.

(93) Ebelman, M. *Ann. Chimie Phys.* **1846**, *16*, 129.

(94) Ebelman, M. *M. C. R. Acad. Sci* **1847**, *25*, 854.

(95) Graham, T. *Chem. Soc.* **1864**, *17*, 318.

(96) Roy, R. *J. Am. Ceram. Soc.* **1956**, *39*, 145.

(97) Roy, R. *J. Am. Ceram. Soc.* **1969**, *52*, 344.

(98) Stöber, W.; Fink, A.; Bohn, E. *J. Colloid Interface Sci.* **1968**, *26*, 62.

(99) Zhang, Y. H.; Zhang, H. X.; Xu, Y. X.; Wang, Y. G. *J. Mater. Chem.* **2003**, *13*, 2261.

(100) Julian, B.; Corberan, R.; Cordoncillo, E.; Escribano, P.; Viana, B.; Sanchez, C. *Nanotechnol.* **2005**, *16*, 2707.

(101) Krebs, J. K.; Happek, U. *J. Lumin.* **2001**, *94*, 65.

(102) Biswas, A.; Maciel, G. S.; Friend, C. S.; Prasad, P. N. *J. Non-Cryst. Sol.* **2003**, *316*, 393.

(103) Biswas, A.; Maciel, G. S.; Kapoor, R.; Friend, C. S.; Prasad, P. N. *Appl. Phys. Lett.* **2003**, *82*, 2389.

(104) Tanabe, S.; Hayashi, H.; Hanada, T.; Onodera, N. *Opt. Mater.* **2002**, *19*, 343.

(105) Yeatman, E. M.; Ahmad, M. M.; McCarthy, O.; Martucci, A.; Guglielmi, M. *J. Sol-Gel Sci. Tech.* **2000**, *19*, 231.

(106) Slooff, L. H.; de Dood, M. J. A.; van Blaaderen, A.; Polman, A. *Appl. Phys. Lett.* **2000**, *76*, 3682.

(107) Cheng, J. A.; Chen, C. H. *J. Mater. Chem.* **2005**, *15*, 1179.

(108) Tang, C. W.; Vanslyke, S. A. *Appl. Phys. Lett.* **1987**, *51*, 913.

(109) Chen, C. T. *Chem. Mater.* **2004**, *16*, 4389.

(110) Sheats, J. R. *Science* **1997**, *277*, 191.

(111) Park, J. H.; Lee, T. W.; Kim, Y. C.; Park, O. O.; Kim, J. K. *Chem. Phys. Lett.* **2005**, *403*, 293.

(112) Suzuki, M.; Hatakeyama, T.; Tokito, S.; Sato, F. *IEEE. J. Sel. Top. Quant. Electron.* **2004**, *10*, 115.

(113) Bernius, M. T.; Inbasekaran, M.; O'Brien, J.; Wu, W. S. *Adv. Mater.* **2000**, *12*, 1737.

(114) Holmes, K. L.; Lantz, L. M. *Method. Cell Biol., Vol 63* **2001**, *63*, 185.

(115) Hung, S. C.; Ju, J.; Mathies, R. A.; Glazer, A. N. *Anal. Biochem.* **1996**, *238*, 165.

(116) Shimomura, O.; Johnson, F. H.; Saiga, Y. *J. Cell. Comp. Physiol* **1962**, *59*, 223.

(117) Purdy, M. D.; Ge, P. H.; Chen, J. Y.; Selvin, P. R.; Wiener, M. C. *Acta Crystallograph. D* **2002**, *58*, 1111.

(118) Selvin, P. R. *Ann. Rev. Biophys. Biomol. Struct.* **2002**, *31*, 275.

(119) Selvin, P. R.; Ge, P. H. *Biophys. J.* **2002**, *82*, 427A.

(120) Dabbousi, B. O.; RodriguezViejo, J.; Mikulec, F. V.; Heine, J. R.; Mattoussi, H.; Ober, R.; Jensen, K. F.; Bawendi, M. G. *J. Phys. Chem. B* **1997**, *101*, 9463.

(121) Norris, D. J.; Bawendi, M. G. *Phys. Rev. B* **1996**, *53*, 16338.

(122) Chen, C. C.; Herhold, A. B.; Johnson, C. S.; Alivisatos, A. P. *Science* **1997**, *276*, 398.

(123) Peng, X. G.; Wilson, T. E.; Alivisatos, A. P.; Schultz, P. G. *Angew. Chem. Int. Ed.* **1997**, *36*, 145.

CHAPTER 3

Part I. Bright white light through up-conversion of a single NIR source from sol-gel derived thin film made with Ln^{3+}-doped LaF_3 nanoparticles*©

---

* The major part of the work in this chapter has been published:

1) Sri Sivakumar, Frank C.J.M. van Veggel, and Mati Rausdepp, *J. Am. Chem. Soc.* **2005**, 127, (36), 12464-12465.

2) Sri Sivakumar, Enrico Bovero, Frank C. J. M. van Veggel, submitted.

3) Sri Sivakumar, Frank C. J. M. van Veggel, submitted.

4) Sri Sivakumar, Frank C. J. M. van Veggel, manuscript in preparation.

3.1.1. Introduction

There is a large interest in cheap efficient generation of (white) light sources for a variety of purposes and reasons such as, displays, liquid crystal display (LCD) back light and general lighting appliances in particular the replacement of the incandescent light bulb.[1-3] There are three basic approaches, 1) the conversion of electricity, 2) the conversion of light, either by down-conversion or up-conversion and 3) thermal radiation in the incandescent lamp to achieve white light. Electricity is exploited in light-emitting diodes with some major advances over the last few years in organic light emitting diodes (OLEDs)[4-7] and polymer light emitting diodes (PLEDs).[8-10] In particular the generation of white light from OLEDs and PLEDs has proven to be challenging because, 1) blue and white light emitters are not as efficient as green and red emitters,[11-14] 2) energy down conversion in the case of multilayer devices, i.e blue light can easily be absorbed by a green chromophore, followed by emission of yellow or red light which can then be absorbed by a red chromophore, etc. This process results in one colour emission, 3) bias dependant colour variation i.e recombination zone of hole and electron is shifted at different biases because of different mobilities of the charge carriers,[15] 4) often several layers are involved in the devices which leads to high manufacturing cost,[16] 5) long term stability of emitters remains an issue.[17] Down conversion is the conversion of higher energy UV light into visible light and is widely exploited in phosphors.[18] The short-wavelength emitting light sources can be used as efficient pumps to excite organic and inorganic luminescent matrices for subsequent photon emission at lower energies. The main challenge of this process is the degradation of the emitting material especially in the organic light emitting materials over time due to photoionization. The up-conversion

process converts lower energy photons via multiphoton processes into higher energy photons,[19] which has been explained in more detail in the chapter 2. In our approach, the near-infrared photons are converted into visible photons. An incandescent light bulb produces light by heating a small filament of tungsten to about 2500 °C. At that temperature, the thermal radiation that the filament emits includes a substantial amount of visible light. But the filament also emits a great deal of infrared light ("heat") and it also transfers heat via conduction and convection to the glass bulb around it. This is one of the oldest devices and despite many years of use, the efficiency is very low (10-12%).[14, 20]

The up-conversion process which is dealt within this thesis is based on sequential absorption and energy transfer steps involving real metastable excited states that are intermediate in energy between the ground state and the emitting state of the ion. This process requires the absorption of at least two photons to provide sufficient energy for the up-converted emission to occur. Lanthanide ions are suitable candidates for up-conversion processes because of their energy level structure, which provides many intermediate levels with favourable spacing and their long-lived excited states.[19, 21, 22] Moreover, cheap NIR diode continuous wave (CW) laser can be used as excitation source. This event is different from multiphoton absorption processes, which occur in a medium through the simultaneous absorption of two or more photons via a non-stationary, virtual quantum mechanical state, requiring high excitation densities. In order to achieve an efficient, cost effective and durable white light source, the following points have to be considered: i) stable photocycle of the emitting species, ii) one cheap excitation source (e.g. 980 nm CW laser) and efficient absorption, iii) easy control over

the luminescence intensity of red, green, and blue emission, iv) easy and cost effective fabrication of the device.

In this chapter, a simple method to produce white light from sol-gel matrix like SiO_2 and ZrO_2 made with Ln^{3+} doped LaF_3 nanoparticles co-doped with Yb^{3+} ions is reported (Scheme 3.1). A number of reports are available regarding up-conversion of lanthanide ions in Y_2O_3,[22, 23] Gd_2O_3,[24] ZrO_2,[25-27] and SiO_2[28] matrices prepared by sol-gel method, however, white light generation by using single excitation source like 980 nm CW laser has not been reported. The co-doping with Yb^{3+} ions makes it possible to excite with a single excitation source and generate visible light through two- and three-photon processes involving energy transfer from Yb^{3+} ions to the respective Ln^{3+} ions. Red, green, and blue emission were generated from three different lanthanide ions such as Er^{3+}(red as well as green), Eu^{3+}(red), Tm^{3+}(blue) ions. This is the initial combination, which is discussed in this part I to prove the principle of our approach to generate white light. Scheme 3.1 demonstrates that white light can be generated from a sol-gel thin film made with Yb^{3+}/Eu^{3+} (red), Yb^{3+}/Er^{3+} (green/red) and Yb^{3+}/Tm^{3+} (blue) –doped nanoparticles in a particular ratio (ratio not shown in the scheme) by exciting with 980 nm laser as a single excitation source. We have achieved the following points by using three different types of nanoparticles in the preparation of single sol-gel thin layer: 1) the Commission Internationale de l'Eclairage (CIE) coordinates of the resulting light can easily be adjusted by controlling the concentration of lanthanide ions in the nanoparticles[29-35] as well as the concentration of nanoparticles (Ln^{3+} doped) in the sol-gel thin layer, 2) internal energy transfer between Eu^{3+}, Er^{3+} and Tm^{3+} ions is avoided by the spatial isolation of the blue, green, and red emitters in the sol-gel layer.

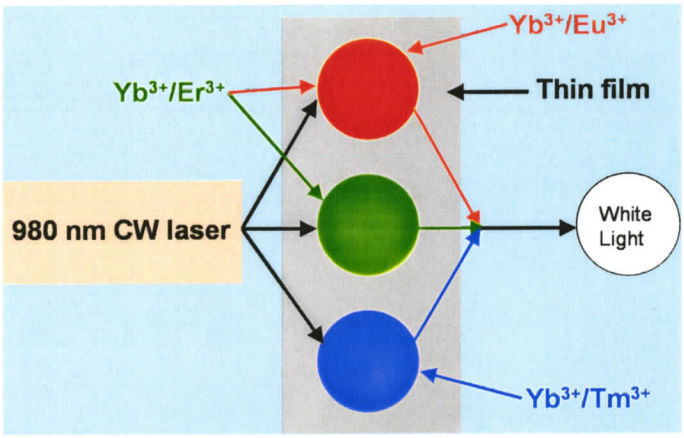

Scheme 3.1. Schematic diagram of generation of white light.

Moreover, the advantages of the sol-gel derived thin film process were also exploited such as its simplicity and its ability to control the purity and homogeneity of the sol-gel material on a molecular level. It also offers the possibility of modifying the refractive index, phonon energy, and transparency of the material.[36] SiO_2 and ZrO_2 films prepared by sol-gel method are potential candidates for making planar waveguides, flat display panels with increased number of pixels, and fiber amplifiers. Furthermore, SiO_2 and ZrO_2 are thermally and chemically robust. The present work takes advantage of a route that we have recently published to improve the NIR emission of lanthanide ions in sol-gel derived thin films, of which an important aspect is the effective isolation of lanthanide ions from the high phonon energy matrix, residual OH groups, and absence of lanthanide ion clustering.[37] The films were transparent to visible light and no cracks were observed with an optical microscope. Spin coating of this sol-gel at 3600 rpm on a silicon wafer followed by soft baking at 100 °C resulted in a film thickness of 192 nm. Further baking at 1100 °C reduced the thickness to 144 nm due to the densification that took place. The thickness evolution of the films with different annealing temperatures and

variation of refractive index of the films with particles concentrations have been discussed in a recent publication.[38]

A convenient and a straight forward method to incorporate nanoparticles in sol-gel matrices like SiO_2, ZrO_2, etc., requires that the nanoparticles are dispersible in water. This is achieved by a judicious choice of the stabilising ligand. Citrate turned out to be a suitable ligand, which on coordination on the surface of the nanoparticle makes it dispersible in water. The main advantage of the citrate ligand is that it gets completely removed from the matrix as gaseous products without leaving any carbon residues, on heating in air at a relatively low temperature of around 400 °C. The higher temperature heat treatment is an essential step in the fabrication of sol-gel films, as it significantly reduces the OH concentration in the film, thereby reducing the quenching brought about by them. The presented approach is very simple, takes advantage of our group's work on monolayer-coated Ln^{3+}-doped LaF_3 nanoparticles, and allows for straightforward optimisation.[30-32, 37] Eventhough $NaYF_4$[21], $NaGdF_4$[39] are good host materials for up-conversion of lanthanide ions, however, to our knowledge, water-soluble nanoparticles have not yet been reported. This chapter is organized as follows: The preparation of nanoparticles of initial combination, sol-gel thin films and their characterisation is discussed in part I of this chapter. Part II discusses the improvement in the efficiency of generation of white light by using different combination of nanoparticles, their up-conversion mechanisms and their efficiency of white light generation.

3.1.2. Results and Discussion

3.1.2.1. Citrate-stabilised nanoparticles

Citrate-stabilised $La_{0.45}Yb_{0.50}Er_{0.05}F_3$, $La_{0.75}Yb_{0.20}Tm_{0.05}F_3$, and $Yb_{0.75}La_{0.20}Eu_{0.05}F_3$ nanoparticles were prepared by the co-precipitation technique in aqueous solution in presence of citrate ions. The citrate prevents agglomeration of the nanoparticles, which would lead to precipitation. Formation of citrate-stabilised nanoparticles has been confirmed from ^1H NMR spectrum and AFM image of the nanoparticles. The broad NMR peak around 2.6 ppm is characteristic of the protons of the citrate ligands coordinated to the surface of the nanoparticle. The broadening is ascribed to the inhomogeneous distribution of the magnetic environment around nanoparticles and a reduction in the rotational freedom of the ligand. The AFM image of a representative $La_{0.45}Yb_{0.5}Er_{0.05}F_3$ sample shows that the majority of the particles have heights in the range of 3-7 nm (Figure 3.1). The larger features are due to nanoparticles agglomeration, which likely occur during solvent evaporation due to capillary interaction. The emission spectrum (data are not shown in the thesis) of nanoparticles in water by direct excitation shows the corresponding emission lines of Er^{3+}, Tm^{3+}, Eu^{3+} and Yb^{3+} ions, respectively, which are consistent with our previously reported Ln^{3+}-doped LaF_3 nanoparticles. A full detailed account on the optical characterisation, doping level of lanthanide ions, core-shell structures and surface modification of these nanoparticles has been published by former group members.[29-35, 37]

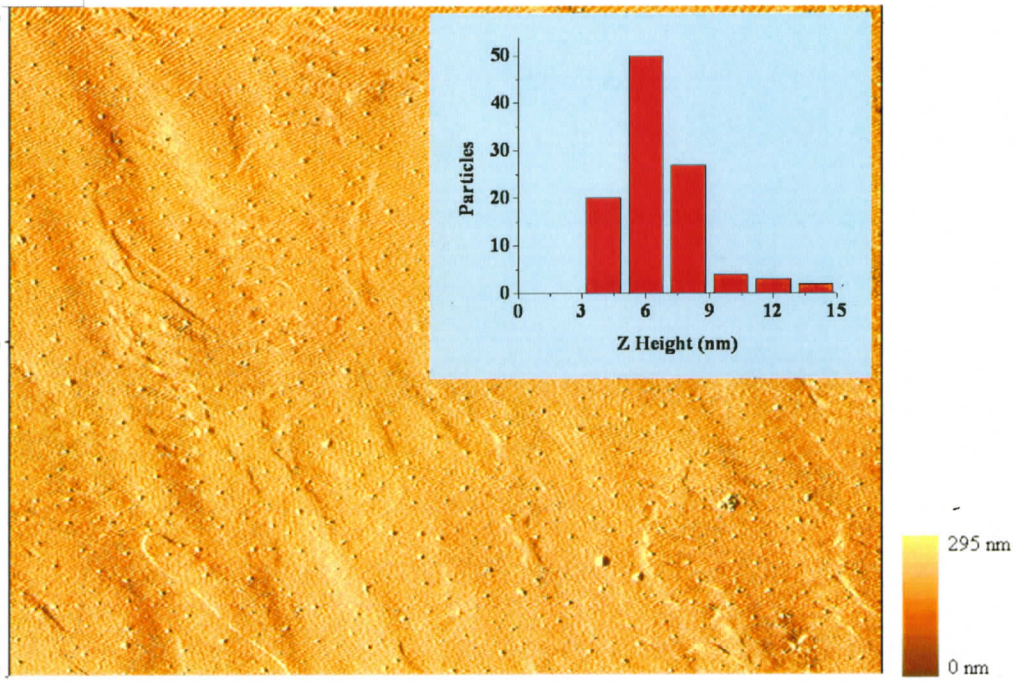

Figure 3.1. AFM image of citrate stabilised $La_{0.45}Yb_{0.5}Er_{0.05}F_3$ nanoparticles deposited on a mica substrate from a water dispersion, inset is histogram of particle sizes.

3.1.2.2. Silica sol-gel thin films made with $La_{0.45}Yb_{0.5}Er_{0.05}F_3$, $La_{0.75}Yb_{0.2}Tm_{0.05}F_3$, and $Yb_{0.75}La_{0.2}Eu_{0.05}F_3$ nanoparticles

Figure 3.2 shows the up-conversion emission spectrum of silica films made with $La_{0.45}Yb_{0.5}Er_{0.05}F_3$, $La_{0.75}Yb_{0.2}Tm_{0.05}F_3$, and $Yb_{0.75}La_{0.2}Eu_{0.05}F_3$ nanoparticles. Emission peaks at red, green and blue region can clearly be seen. The calculated colour coordinates are 0.37 and 0.32.[40, 41] These values fall within the white region of 1931 Commission Internationale de l'Eclairage (CIE) diagram.[41]

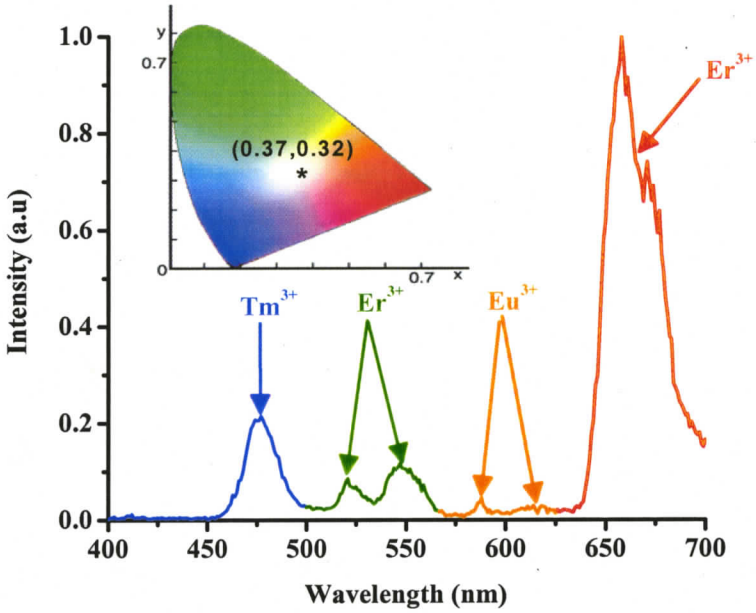

Figure 3.2. Up-conversion emission spectrum of silica thin film prepared at 800 °C made with $La_{0.45}Yb_{0.5}Er_{0.05}F_3$, $La_{0.75}Yb_{0.2}Tm_{0.05}F_3$, and $Yb_{0.75}La_{0.2}Eu_{0.05}F_3$ nanoparticles under 300 mW 980 nm CW laser excitation (the insets show the CIE colour coordinates of the resulting white light).

This white light was bright and can been seen by naked eye even at a laser pump power of only 200 mW. There is virtually no change in the colour coordinates of the white light with a change in the excitation power. This is usually not in the case of OLEDs and PLEDs because of different mobilities of the charge carriers. The weak emissions at 590 and 612 nm from the Eu^{3+} ions are necessary, because in the absence of these emissions the colour coordinates move slightly towards the green region (0.30, 0.41).

The emission band around 470 nm is assigned to the $^1G_4$ to $^3H_6$ transition of Tm^{3+} ions. An emission band of Tm^{3+} ions at 790 nm ($^3H_4$ to $^3H_6$ transition) was also observed (Figure 3.3). Er^{3+} ions gave emission peaks around 515, 540, and 645 nm, which are assigned to the $^2H_{11/2}$ to $^4I_{15/2}$, $^4S_{3/2}$ to $^4I_{15/2}$, $^4F_{9/2}$ to $^4I_{15/2}$ transitions, respectively. The intensity ratio of red to green emission from Er^{3+} ions can be tuned by changing the concentration of Yb^{3+} ions in the Y_2O_3[23] and Gd_2O_3[24] nanoparticles. We also found similar green to red ratio dependence by changing the Yb^{3+} ion concentration in the nanoparticles, which is discussed in part II of this chapter and chapter 4. The emission bands around 590 nm and 612 nm are assigned to the $^5D_0$ to $^7F_1$ and $^5D_0$ to $^7F_2$ transitions of Eu^{3+} ions, respectively.

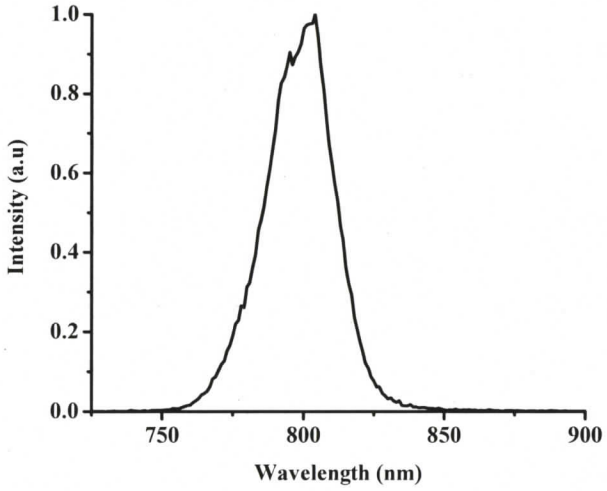

Figure 3.3. Up-conversion emission spectrum of silica thin film prepared at 800°C made with $La_{0.75}Yb_{0.2}Tm_{0.05}F_3$ nanoparticles under 300 mW 980 nm CW laser excitation.

We also observed relatively weak blue emission at 490 nm from a silica film made with $Yb_{0.8}La_{0.15}Eu_{0.05}F_3$ nanoparticles, which results from co-operative up-conversion of

two Yb^{3+} ions. However, the blue emission is very weak compared with blue emission from Tm^{3+} ions. Maciel *et al.* have reported this co-operative up-converted emission mechanism in Yb^{3+} and Eu^{3+} doped silica glasses prepared at 1000 °C.

In order to show that it is essential to use three different Ln^{3+}/Yb^{3+} doped LaF_3 nanoparticles, a silica thin film was prepared with the same concentrations of La^{3+}, Er^{3+}, Tm^{3+}, and Eu^{3+} ions with Yb^{3+} ions by direct incorporation and subjected to the same heat treatment (Scheme 3.2).

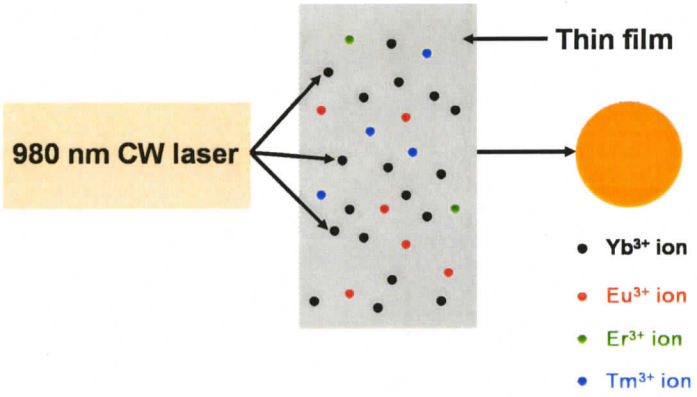

Scheme 3.2. Schematic diagram for a control silica thin film

This sample only shows green and red emission from Er^{3+} ions and no blue and red emission from Tm^{3+} ions and Eu^{3+} ions, respectively (Figure 3.4). The possible reason for this could be, 1) energy transfer between the ions that leads to one colour emission, 2) the co-operative up-conversion of Eu^{3+} does not occur because Yb^{3+} ions should be close to each other, which is unlikely in the case of control thin film, 3) the blue emission from Tm^{3+} is quenched because of residual OH groups present in the silica thin film, 4) clustering of lanthanide ion leads to quenching and 5) high phonon energy of silica matrix quenches the lanthanide ion emission. This clearly demonstrates that a single silica thin film prepared with three different Ln^{3+}/Yb^{3+} doped nanoparticles is necessary to produce

white light. Ln^{3+} (Tm^{3+}, Eu^{3+}) ions with the Yb^{3+} ions individually incorporated in silica thin film and subjected to same heat treatment didn't show any up-conversion, which clearly demonstrates the advantage of silica thin film prepared with nanoparticles rather than direct doping of lanthanide ions. It is obvious that blue, green, and red emission can be produced separately as well from silica thin film individually made with Ln^{3+} doped nanoparticles.

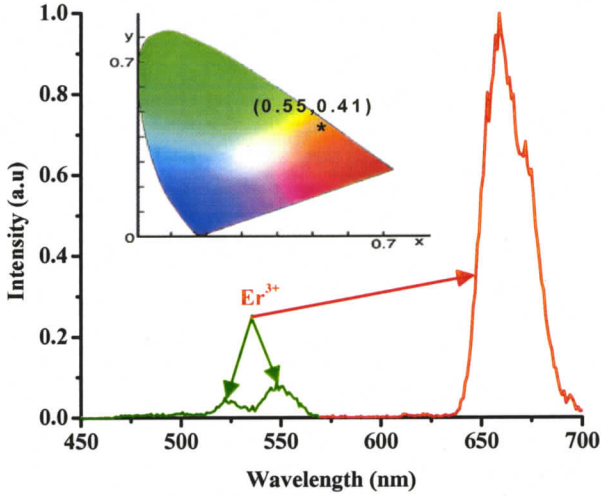

Figure 3.4. Up-conversion emission spectrum of Ln^{3+}(Er^{3+}, Tm^{3+} and Eu^{3+}) and Yb^{3+} ions directly incorporated in one silica film prepared at 800 °C as control sample under 300 mW 980 nm CW laser excitation.

3.1.2.3. ZrO_2 sol-gel thin films made with $La_{0.45}Yb_{0.5}Er_{0.05}F_3$, $La_{0.75}Yb_{0.2}Tm_{0.05}F_3$, and $Yb_{0.75}La_{0.2}Eu_{0.05}F_3$ nanoparticles

In order to further substantiate the generality of the method, above experiments were repeated by taking ZrO_2 as the sol-gel matrix. Similar to SiO_2 matrix, white light

was observed with the coordinates of 0.37, 0.31 when the ZrO_2 films were made with $La_{0.45}Yb_{0.5}Er_{0.05}F_3$, $La_{0.75}Yb_{0.2}Tm_{0.05}F_3$, and $Yb_{0.75}La_{0.2}Eu_{0.05}F_3$ nanoparticles (Figure 3.5). A ZrO_2 thin film prepared with the same concentrations of La^{3+}, Er^{3+}, Tm^{3+}, and Eu^{3+} ions with Yb^{3+} ions by direct incorporation only showed green and red emission from Er^{3+} ions and no blue and red emission from Tm^{3+} ions and Eu^{3+} ions, respectively (Figure 3.6). This again substantiates the importance of the role of three different nanoparticles to produce the white light.

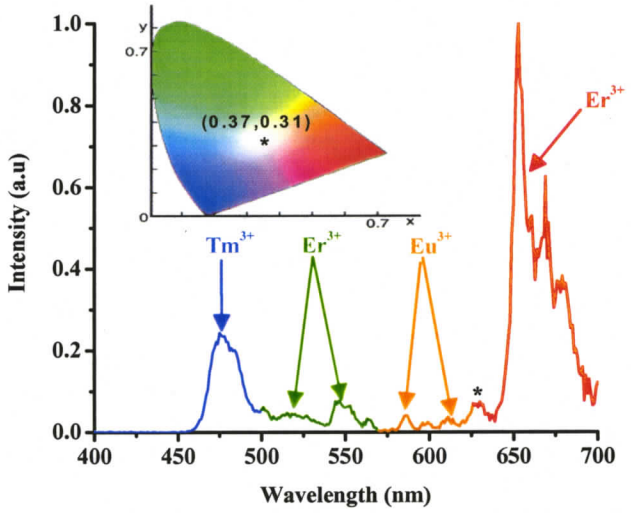

Figure 3.5. Up-conversion emission spectrum of ZrO_2 thin film prepared at 800 °C made with $La_{0.45}Yb_{0.5}Er_{0.05}F_3$, $La_{0.75}Yb_{0.2}Tm_{0.05}F_3$, and $Yb_{0.75}La_{0.2}Eu_{0.05}F_3$ nanoparticles under 300 mW 980 nm CW laser excitation (the inset shows the CIE colour coordinates of the resulting white light). * The origin of the emission at 630 nm is not entirely clear.

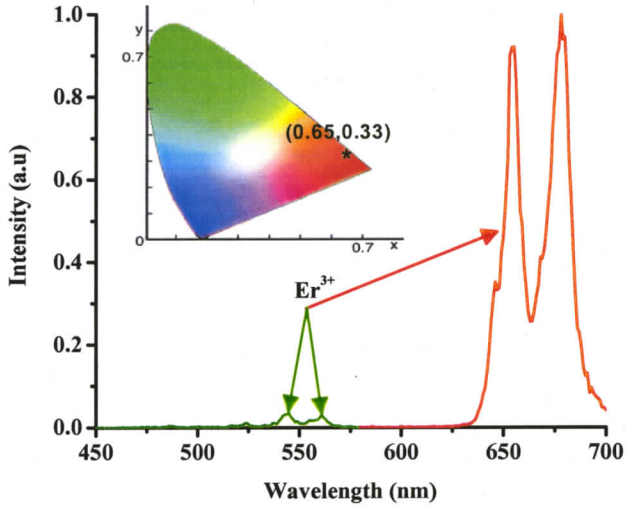

Figure 3.6. Up-conversion emission spectrum of Ln^{3+}(Er^{3+}, Tm^{3+} and Eu^{3+}) and Yb^{3+} ions directly incorporated in one ZrO_2 film prepared at 800 °C as a control sample under 300 mW 980 nm CW laser excitation.

3.1.2.4. XRD characterisation of sol-gel thin films

Our recent report[37] on the highly luminescent sol-gel derived silica and alumina films by using LaF_3 nanoparticles doped with lanthanide ions, (Er^{3+}, Nd^{3+} and Ho^{3+}) shows the presence of a non-stoichiometric lanthanum silicate phase ($La_{9.31}Si_{6.24}O_{26}$) along with the expected LaF_3 phase from X-ray diffraction (XRD) studies carried out on a silica thin film sample. It is likely that the surface of the Ln^{3+}-doped LaF_3 nanoparticles has reacted with the silanol groups of the matrix to form the Ln^{3+}-doped lanthanum silicate surrounding a core of unreacted Ln^{3+}-doped LaF_3 nanoparticle. Line width analysis showed that these phases are nanoparticles of size of ~8 nm, embedded in a SiO_2 matrix. It is reasonable to assume that the same phases are present in the current sample

because they were prepared similarly. XRD studies carried out on ZrO_2 thin films made with nanoparticles showed the presence of lanthanum zirconate ($La_2Zr_2O_7$), but no LaF_3 (Figure 3.7). It has been concluded that the nanoparticles have reacted with OH groups present in ZrO_2 sol-gel to form Ln^{3+} doped lanthanum zirconate. In spite of the formation of lanthanum zirconate, the three pairs of Ln^{3+} ions are still spatially isolated in the sol-gel layer made as nanoparticles, which is not the case of direct incorporation of Ln^{3+} ions. So, effectively the pairs of Ln^{3+} ions are still in a nanoparticle that has very low phonon energy (~ 300 cm^{-1}). This is substantiated by the results from our control experiments done with direct incorporation of La^{3+}, Er^{3+}, Tm^{3+}, and Eu^{3+} ions with Yb^{3+} ions in sol-gel matrix (vide supra).

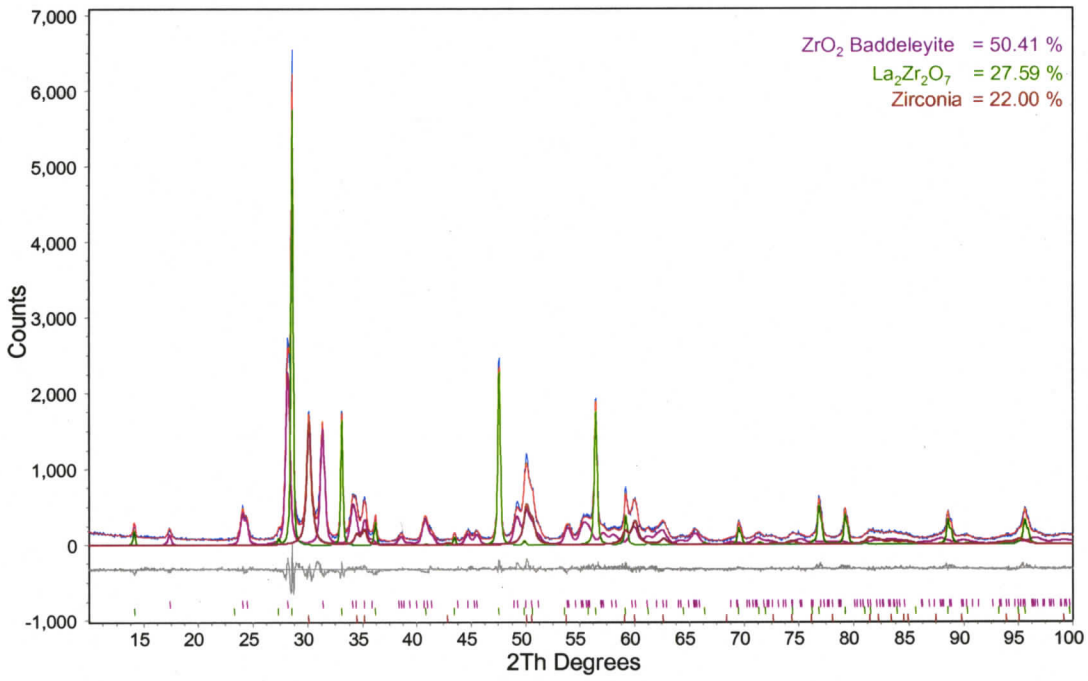

Figure 3.7. Experimental and calculated XRD pattern (Rietveld refinement plot) of a silica film prepared at 800 °C made with 25 weight % of $La_{0.45}Yb_{0.50}Er_{0.05}F_3$ nanoparticles. Blue lines: sample, Green lines: $La_2Zr_2O_7$ phase, Violet lines: ZrO_2 Baddeleyite phase, Red lines: Zirconia, Grey: residue

In part I, generation of white light from SiO_2 and ZrO_2 sol-gel thin film made with Ln^{3+} doped nanoparticles co-coped with Yb^{3+} ions have been discussed. The control experiments proved the need of Ln^{3+} doped nanoparticles rather than Ln^{3+} ion directly incorporated in SiO_2 and ZrO_2 thin films. Notwithstanding this progress, there is still a need to improve the efficiency of generation of white light to compete with existing white light emitters which is reported in part II of this chapter.

Part II. Efficient up-conversion of 980 nm light into bright white light from sol-gel derived thin film made with new combinations of $LaF_3:Ln^{3+}$ nanoparticles

3.2.1. Method to increase the efficiency of generation of white light

In a recent report, Service[14] has argued on the importance of efficiency of white light generation and stated that in the United States alone lighting consumes up to more than six quadrillion British thermal units (BTUs) of energy every year (1 BTU = 1057 joules); and constitutes 17% of all the energy used in buildings. He recommends that in order to "save the world" we have to start getting rid of the incandescent light bulbs, which converts 90% of the energy into heat. In part I of this chapter, it has been reported[42] that a general and facile method to generate bright white light emission through up-conversion from a sol-gel derived thin film made with Ln^{3+}/Yb^{3+} doped LaF_3 nanoparticles as an alternative to the existing white light emitters such as organic light emitting diodes (OLEDs),[6, 14, 43-46] polymer light emitting diodes (PLEDs)[10, 47] and incandescent light bulbs.[14] It is demonstrated that the current material has a number of advantages such as a completely stable photocycle, one cheap excitation source (980 nm CW laser), efficient absorption and easy control over the luminescence intensity (red, green, and blue emission) over the existing white light emitters.

In these thin films, Tm^{3+} and Eu^{3+} ions are responsible for blue and red emissions, respectively. Er^{3+} ion is responsible for green as well as deep red emission. However, the blue emission from Tm^{3+} ions and green and deep red emission from Er^{3+} ions are much more efficient than the red emission from Eu^{3+} ions. It has been reported in part I that the weak emissions at 590 and 612 nm from the Eu^{3+} ions are necessary because in the absence of these emissions the colour coordinates moved slightly towards the green region (0.30, 0.41). In addition, a large amount (Table 3.1) of Yb^{3+} ions had to be used to achieve very little red emission. This reduces the efficiency of white light because a

considerable amount of 980 nm light is consumed by the Yb^{3+}/Eu^{3+} -doped nanoparticles. The reason for this could be the inefficient energy transfer process occurring in Yb^{3+}/Eu^{3+}-doped nanoparticles (see below). In order to increase the efficiency of our approach other suitable combinations of lanthanide ions are needed, which are reported here.

Table 3.1. Amount of nanoparticles used for making thin films

Combination	Amount of nanoparticles used
1	$La_{0.75}Yb_{0.20}Tm_{0.05}F_3$ (150 mg), $La_{0.75}Yb_{0.20}Ho_{0.05}F_3$ (0.5 mg) and $La_{0.45}Yb_{0.50}Er_{0.05}F_3$ (0.5 mg)
2	$La_{0.75}Yb_{0.20}Tm_{0.05}F_3$ (150 mg) and $Yb_{0.75}La_{0.20}Er_{0.05}F_3$ (1 mg)
3	$La_{0.75}Yb_{0.20}Tm_{0.05}F_3$ (100 mg) $La_{0.45}Yb_{0.5}Er_{0.05}F_3$ (0.5 mg) and $Yb_{0.75}La_{0.20}Tb_{0.05}F_3$ (100 mg)
4	$La_{0.75}Yb_{0.20}Tm_{0.05}F_3$ (100 mg) $Yb_{0.75}La_{0.20}Tb_{0.05}F_3$ (80 mg) and $Yb_{0.75}La_{0.20}Eu_{0.05}F_3$ (150 mg)
Part I	$La_{0.75}Yb_{0.20}Tm_{0.05}F_3$ (100 mg), $Yb_{0.75}La_{0.20}Er_{0.05}F_3$ (1 mg) and $Yb_{0.75}La_{0.20}Eu_{0.05}F_3$ (150 mg)

The energy transfer from Yb^{3+} ions to Eu^{3+} ions is occurring via co-operative up-conversion process. In co-operative up-conversion process two excited donor ions (Yb^{3+}) ions simultaneously transfer their energy to acceptor (Eu^{3+}) ions. This co-operative

energy transfer results in up-conversion of energy but it is a three-ion process requiring coupling between three ions, which is different from traditional up-conversion processes that require two-ion interactions. Ostermayer *et al.*[48] have estimated that such co-operative up-conversion processes are ~ 130 times weaker than the efficient traditional up-conversion energy transfer process (Er-Yb).

New alternative sol-gel thin films based on SiO_2 and ZrO_2 made with four different new combinations of Ln^{3+}-doped LaF_3 nanoparticles co-doped with Yb^{3+} ion is reported in this part. These new sol-gel thin films produced white light with increased brightness and efficiency when compared to our earlier thin film.[42] Like our previous material reported in part I, the co-doping with Yb^{3+} ions makes it possible to excite the thin film with a single excitation source (980 nm light) and generate visible light through energy transfer from Yb^{3+} ions to the respective Ln^{3+} ions. Red, green, and blue emissions were generated from five different lanthanide ions such as Er^{3+}(red as well as green), Ho^{3+}(red as well as green), Tb^{3+} (strong green and weak red) , Eu^{3+} (red) and Tm^{3+}(blue) ions. The white light was generated by incorporating the suitable combination of these water-soluble lanthanide ions-doped nanoparticles in the sol-gel matrix. We have achieved the following along with the advantages of our earlier thin film. First, the efficiency of white light generation is 33-fold higher than the thin film reported in part I. Second, lower amounts of Yb^{3+}/Ln^{3+} ions were used when compared to our earlier thin film which is important from a cost point of view.

3.2.2. Results and Discussion

3.2.2.1 White light from silica thin film made with combination 1

The combination of Ln^{3+}-doped LaF_3 nanoparticles incorporated in sol-gel thin films used to generate the white light are given in Table 3.2. Figure 3.8 shows the digital image of bright white light emission from silica thin film made with nanoparticles of combination 1 under 980 nm CW laser excitation. Bright white light can be seen very clearly from the thin film even at a laser pump power of only 300 mW. Figure 3.9a shows the up-conversion emission spectrum of silica thin film made with nanoparticles of combination 1. Emission peaks at red, green and blue region can clearly be seen in Figure 3.9a. The calculated colour coordinates of the combination 1 are 0.39 and 0.31. These values fall within the white region of 1931 Commission Internationale de l'Eclairage (CIE) diagram. A 26-fold increase in the efficiency of generation of white light was observed when compared to our earlier thin film. In this new combination red emission at 640 nm from Ho^{3+} ions compensates the absence of red emission from Eu^{3+} ions and keeps the colour co-ordinates in the white light region. In addition, the energy transfer from Yb^{3+} ions to Ho^{3+} ions is very efficient when compared to co-operative up-conversion of Yb^{3+} ions to Eu^{3+} ions[48] which makes our new combination overall more efficient. Like the thin film in part I, there is virtually no change in the colour coordinates of the white light with a change in the excitation power.

Table 3.2. Silica thin film made with different combination of nanoparticles

Combination	Luminescent Ln^{3+} ions present	Amount of Yb^{3+} ions present (mg)	Relative efficiency[a]	CIE colour co-ordinates[b]
1	Yb/Tm, Yb/Ho, Yb/Er	7.58	26	0.39, 0.31
2	Yb/Tm, Yb/Er	7.68	33	0.30, 0.34
3	Yb/Tm, Yb/Tb, Yb/Er	23.8	11	0.29, 0.30
4	Yb/Tm, Yb/Tb, Yb/Eu	48.13	2	0.39, 030
Part I	Yb/Tm, Yb/Er, Yb/Eu	66.35	1	0.37, 0.32

[a] Relative efficiency is calculated based on the concentration of Yb^{3+} ions

[b] CIE colour co-ordinates were calculated by using the CIE colour calculator software[41]

The emission band around 470 nm is assigned to the $^1G_4$ to $^3H_6$ transition of Tm^{3+} ions. Both Er^{3+} and Ho^{3+} ions are responsible for green and red emission. Er^{3+} ions gave emission peaks around 515, 540, and 665 nm, which are assigned to the $^2H_{11/2}$ to $^4I_{15/2}$, $^4S_{3/2}$ to $^4I_{15/2}$, $^4F_{9/2}$ to $^4I_{15/2}$ transitions, respectively. Ho^{3+} ions gave two emission bands at approximately 540 nm and 640 nm, which are assigned to the $^5S_2$ to $^5I_8$ and $^5F_5$ to $^5I_8$ transitions, respectively.

Figure 3.8. Digital photograph of white light emission from silica thin film made with nanoparticles of combination 1 (Yb/Tm, Yb/Ho and Yb/Er) under 300 mW 980 nm CW laser excitation.

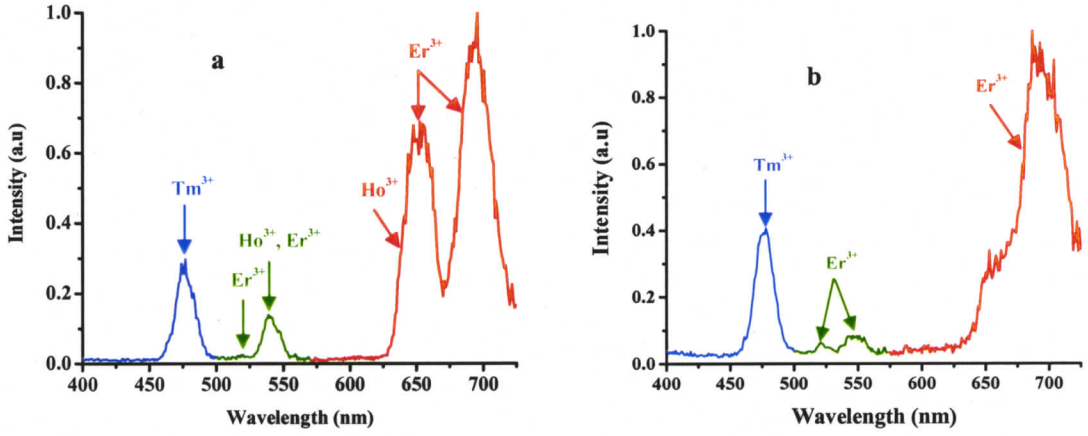

Figure 3.9. Up-conversion emission spectra of silica thin film prepared at 800 °C made with nanoparticles of a) combination 1 (Yb/Tm, Yb/Ho and Yb/Er) b) combination 2 nanoparticles (Yb/Tm and Yb/Er) under 300 mW 980 nm CW laser excitation.

Similar to our previous approach, a control silica thin film was made with the same concentration of La^{3+}, Er^{3+}, Ho^{3+} and Tm^{3+} ions with Yb^{3+} ions by direct incorporation and subjected to the same heat treatment. As observed before, this sample only showed green and red emission from Er^{3+} ions and neither blue emission from Tm^{3+} ion nor green and red emission from Ho^{3+} ions. Ln^{3+} (Ho^{3+}, Tm^{3+}) ions with the Yb^{3+} ions individually incorporated in silica thin film and subjected to same heat treatment didn't show any up-conversion either, which also clearly demonstrates that a single thin film prepared with different nanoparticles is necessary to produce white light. The possible reasons for quenching of other emissions were already discussed in part I.

3.2.2.2. White light from silica thin film made with combination 2

Figure 3.9b shows the up-conversion emission spectrum of silica thin film made with nanoparticles of combination 2. A 33-fold increase in the efficiency of white light generation was observed with nanoparticles of combination 2. The calculated colour coordinates are 0.30 and 0.34. The efficiency of generation of white light from combination 2 has been improved by increasing the red to green emission ratio from Er^{3+} ions. The increase in the red to green emission ratio has been achieved by increasing the concentration of Yb^{3+} ions in the nanoparticle. The detailed discussion about the dependence of red to green ratio on Yb^{3+} concentration is in chapter 4.

3.2.2.3. White light from silica thin film made with combination 3 and 4

Up-conversion emission spectrum of nanoparticles of combination 3 in silica thin film is shown in the Figure 3.10a. An 11-fold increase in the efficiency of generation of white light has been achieved when compared to the thin film in part I.

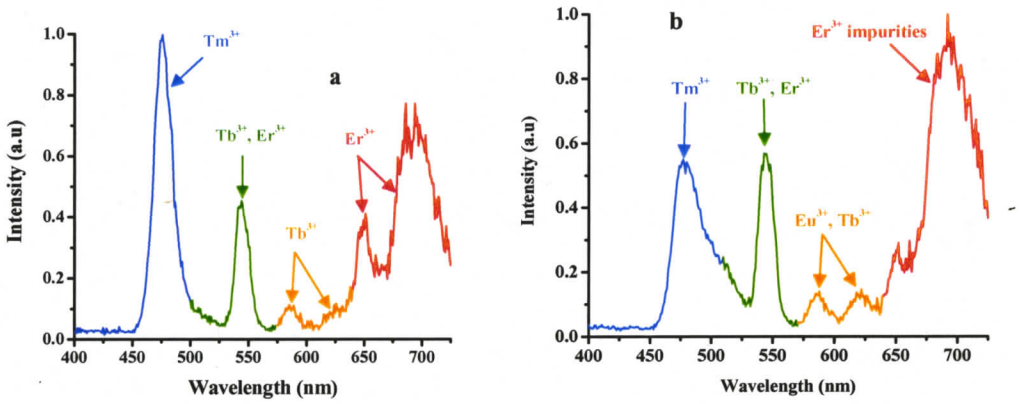

Figure 3.10. Up-conversion emission spectra of silica thin film prepared at 800 °C made with nanoparticles of a) combination 3 (Yb/Tm, Yb/Tb and Yb/Er) b) combination 4 (Yb/Tm, Yb/Tb and Yb/Eu) under 300 mW 980 nm CW laser excitation.

The calculated colour coordinates are 0.30 and 0.34. The emission peaks at 542, 586 and 623 nm are assigned to the $^5D_4$ to $^7F_5$, $^7F_4$ and $^7F_3$ transitions of Tb^{3+} ion, respectively. The co-operative up-conversion of Yb^{3+}-Tb^{3+} ions is more efficient than Yb^{3+}-Eu^{3+} ions because energy transfer can happen relatively easily from the virtual state (~490 nm) of two excited Yb^{3+} ions to the $^5D_4$ level (490 nm) of Tb^{3+} ions, because these two levels are resonant in energy. In the case of Yb-Eu up-conversion process some energy has to be dumped into the matrix during the energy transfer from the virtual state (~490 nm) of two excited Yb^{3+} ions to the $^5D_1$ level (520 nm) of Eu^{3+} ions. Güdel and co-

workers[49] have reported co-operative up-converted emission mechanism in $Cs_3Tb_2Br_9:Yb^{3+}$ single crystal. A control silica thin film made with La^{3+}, Yb^{3+} and Tb^{3+} ions by direct incorporation didn't show any emission, which again supports the need of incorporation of nanoparticles. Figure 3.10b shows the emission spectrum of combination 4. A two-fold increase in the efficiency was observed when compared to the thin film in part I. A lower amount of Yb^{3+}/Eu^{3+} -doped nanoparticles has been used because Tb^{3+} ions also contributes some red emissions at 585 nm and 625 nm in addition to Eu^{3+} emissions. The calculated co-ordinates are 0.30, 0.39. We also observed red emission (660 nm) from Er^{3+} impurities present in the $Yb(NO_3)_3$ salt. Prasad and co-workers[28] have also reported this red emission from Er^{3+} impurities in Yb^{3+} and Eu^{3+} doped silica glasses heated at 1000 °C.

3.2.2.4. White light from ZrO_2 thin film made with combination 1, 2, and 3

Above experiments were repeated by taking ZrO_2 as the sol-gel matrix to prove the robustness of the method. Similar to SiO_2 matrix, white light was observed with the ZrO_2 films made with combination 1 (Figure 3.11a), combination 2 (Figure 3.11b), and combination 3 (Figure 3.12) nanoparticles. ZrO_2 thin films made with these combinations of nanoparticles also showed similar increase in the efficiency of white light like the silica thin films. The calculated CIE colour co-ordinates for all the combinations are given in Table 3.3. The efficiency of generation of white light can likely be further improved by using $LaF_3:Ln^{3+}$ core-shell nanoparticles (the doped LaF_3 core is surrounded by an un-doped shell of LaF_3) in the preparation of silica film. In our recent report[37], we have demonstrated that incorporation of $LaF_3:Ln^{3+}$ core-shell nanoparticle into silica sol-gel

thin layer increases the optical properties of lanthanide ions compared to the core nanoparticle incorporated films.

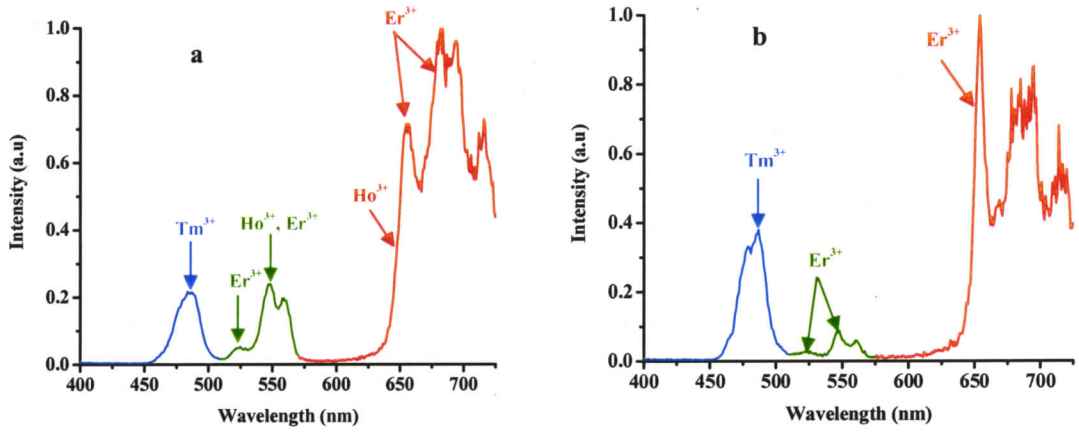

Figure 3.11. Up-conversion emission spectra of ZrO_2 thin film prepared at 800 °C made with nanoparticles of a) combination 1 (Yb/Tm, Yb/Ho and Yb/Er) b) combination 2 (Yb/Tm and Yb/Er) under 300 mW 980 nm CW laser excitation.

A ZrO_2 thin film prepared with the same concentrations of La^{3+}, Er^{3+}, Tm^{3+}, and Ho^{3+} ions with Yb^{3+} ions by direct incorporation only showed green and red emission from Er^{3+} ions and no emission from Tm^{3+} ions and Ho^{3+} ions was observed. Similarly, ZrO_2 thin film prepared with the same concentrations of La^{3+}, Tb^{3+}, Tm^{3+}, and Er^{3+} ions with Yb^{3+} ions showed green and red emission which is from Er^{3+} ions. This again further proved the importance of the nanoparticles in the generation of white light.

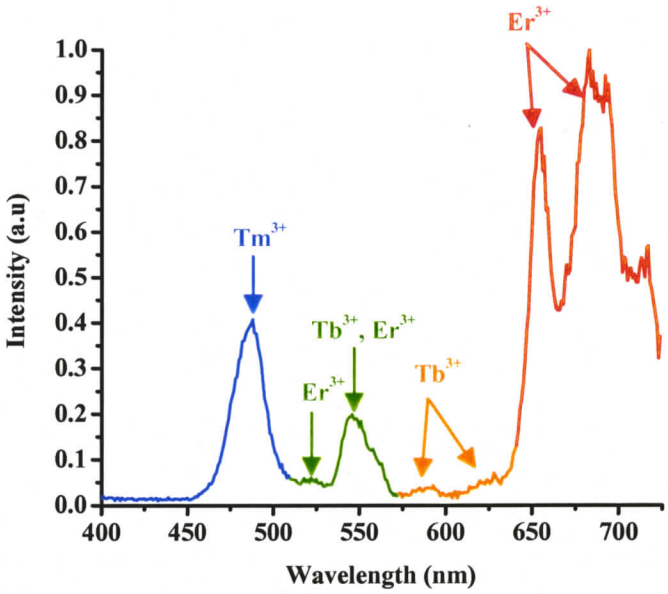

Figure 3.12. Up-conversion emission spectrum of ZrO_2 thin film prepared at 800 °C made with nanoparticles of combination 3 (Yb/Tm, Yb/Tb and Yb/Er) under 300 mW 980 nm CW laser excitation.

Table 3.3. CIE Colour co-ordinates of white light produced from ZrO_2 thin films

Combination	Relative efficiency[a]	CIE colour co-ordinates[b]
1	24	0.37, 0.40
2	30	0.34, 0.29
3	7	0.34, 0.37
Part I	1	0.37, 0.31

[a] Relative efficiency is calculated based on the concentration of Yb^{3+} ions.

[b] CIE colour co-ordinates were calculated by using the CIE colour calculator software.[41]

3.2.3. Mechanism of up-conversion

Possible mechanisms for the up-conversion processes are photon-avalanche (PA), excited state absorption (ESA), and energy transfer (ET). All the three mechanisms have already been discussed in detail in chapter 2. In order to study the up-conversion mechanisms, silica thin films were prepared individually with $La_{0.75}Yb_{0.20}Tm_{0.05}F_3$, $La_{0.75}Yb_{0.20}Ho_{0.05}F_3$, $La_{0.45}Yb_{0.50}Er_{0.05}F_3$, $Yb_{0.75}La_{0.20}Tb_{0.05}F_3$, and $Yb_{0.75}La_{0.20}Eu_{0.05}F_3$ nanoparticles.

3.2.3.1 Up-conversion mechanism in silica thin film made with $La_{0.75}Yb_{0.20}Tm_{0.05}F_3$ nanoparticles

Figure 3.17a shows the dependence of the up-conversion emission intensity on the excitation power in silica thin film individually made with $La_{0.75}Yb_{0.20}Tm_{0.05}F_3$ nanoparticles. Blue emission from Tm^{3+} ion is a three-photon process because the slope of the power dependence graph of blue emission is around 3. Power dependence graphs show a slight decrease in the slope, when the laser power is increased. This can be attributed to a ground state depletion caused by the population build-up of the Yb^{3+} excited level and in turn in the partial saturation of corresponding levels in the lanthanide ions. This up-conversion process is certainly not due to photon-avalanche processes because there is no appearance of threshold in the power dependence graphs and no S-shaped curves are observed. Up-conversion from Tm^{3+} ion must be due to energy transfer processes, because Tm^{3+} ion has no ground or excited state absorption that matches the 980 nm photon. Figure 3.13 demonstrates the up-conversion energy transfer mechanism between Tm^{3+} and Yb^{3+} ions. Initially, Yb^{3+} ions are excited to the $^2F_{5/2}$ level through

absorption of the 980 nm excitation. Subsequently, the excited Yb^{3+} ion transfers its energy to a Tm^{3+} ion in the ground state, there by exciting it to the $^3H_5$ level. Immediately following this process, the excited Tm^{3+} ion in the $^3H_5$ level relaxes to $^3F_4$ level through multiphonon relaxation after which the excited Tm^{3+} ion in the $^3F_4$ level is excited to the $^3F_2$ level through energy transfer from excited Yb^{3+} ion. Subsequently, the excited Tm^{3+} ion in the $^3F_2$ level relaxes to $^3H_4$ level through multiphonon relaxation and further excited to $^1G_4$ level through energy transfer from excited Yb^{3+} ion where by the blue emission at 475 nm takes place. This mechanistic pathway requires three photons to get the blue emission, which is well supported by the slope of three from the power dependence graph (Figure 3.17a). Additionally, an emission at 790 nm ($^3H_4$ to $^3H_6$ transition) takes place.

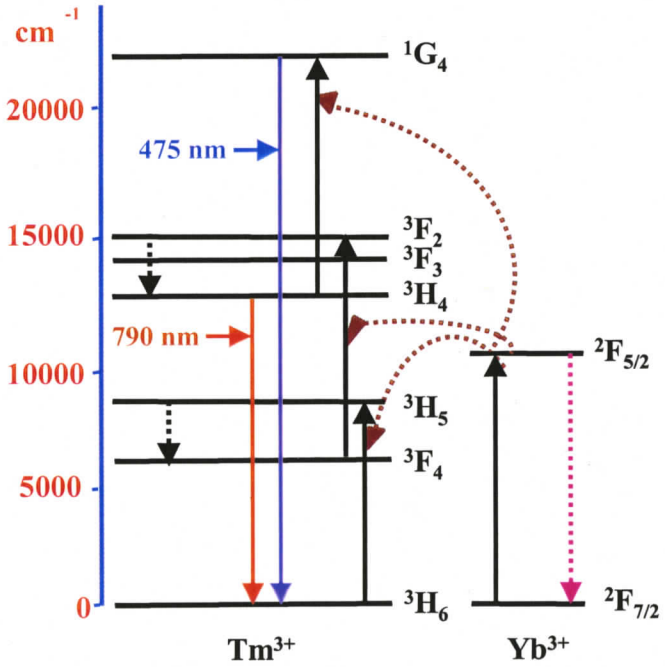

Figure 3.13. Energy level of Tm^{3+} and Yb^{3+} ions as well as the up-conversion mechanisms.

3.2.3.2. Up-conversion mechanism in silica thin film made with $La_{0.75}Yb_{0.20}Ho_{0.05}F_3$ nanoparticles

Figure 3.17b plots the logarithm of up-conversion emission intensity vs. the logarithm of excitation power with the slope ~2. This clearly demonstrates that both the green and red emissions from Ho^{3+} ions are two-photon processes. Similar to Tm^{3+} up-conversion process, this up-conversion process is also certainly due to energy transfer processes, because there is no appearance of threshold in the power dependence graphs and Ho^{3+} ion also has no ground or excited state absorption that matches the 980 nm photon. The proposed mechanism energy transfer up-conversion responsible for both red and green emission is illustrated schematically in Figure 3.14a. Initially Yb^{3+} ions are excited to the $^2F_{5/2}$ level via 980 nm photons through CW laser excitation. Subsequently, the Ho^{3+} ion in the ground state is excited to the $^5I_6$ level through energy-transfer from excited Yb^{3+} ion. Immediately following this process, the excited $Ho^{3+}(^5I_6)$ ion is excited further to the $^5S_2$ level through energy-transfer from excited Yb^{3+} ions where by the green emission at 545 nm takes place. Alternatively, it can relax to the $^5F_5$ level by multiphonon relaxation where by the red emission at 640 nm takes place.

Theoretically, the red emission can occur by another pathway which is unlikely in the current material (Figure 3.14b). The alternative pathway of mechanism is: the excited Ho^{3+} ion in the $^5I_6$ can relax to the $^5I_7$ by multiphonon relaxation. Subsequently, the excited Ho^{3+} ion ($^5I_7$) can be excited to $^5F_5$ level through energy transfer from excited Yb^{3+} ion. This pathway should lead to increase in the green to red emission ratio with the increase in the laser power because of the saturation of the $^5I_6$ level in the higher laser powers. However, there is no increase in the green to red emission ratio with the increase

in laser power in the silica thin film made with $La_{0.75}Yb_{0.20}Ho_{0.05}F_3$ nanoparticles. This clearly demonstrates that this alternative pathway is unlikely in the current material. This pathway is similar to the pathway of the red emission from Er^{3+} through two-photon up-conversion processes (discussed in chapter 2).

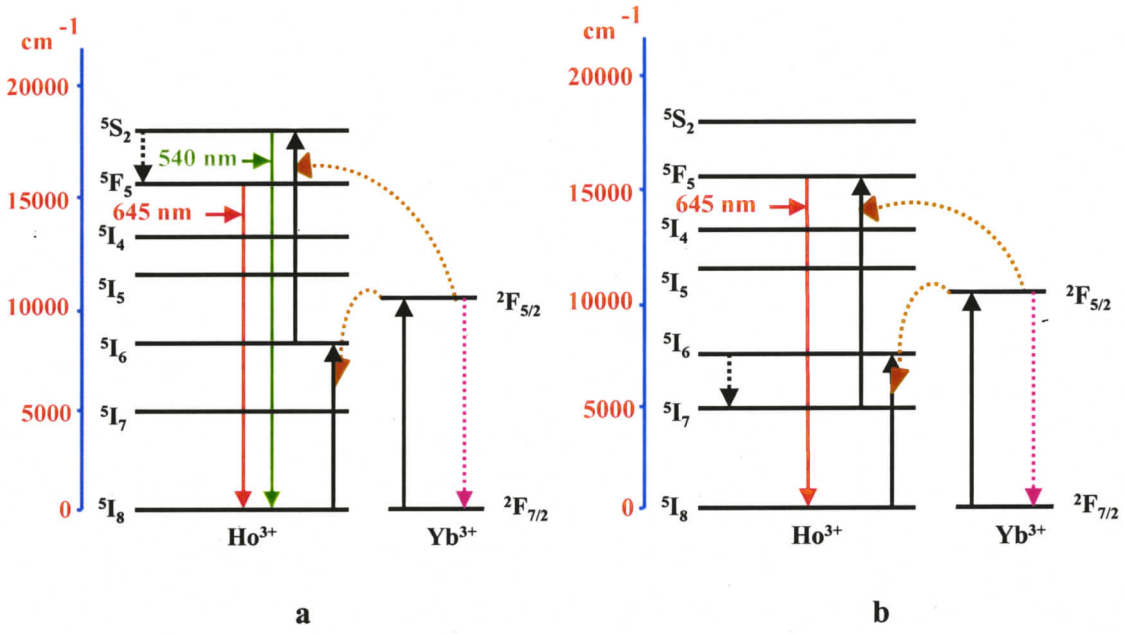

Figure 3.14. Energy level of Ho^{3+} and Yb^{3+} ions as well as the up-conversion mechanisms, a) mechanism occurring in the current sample b) alternative pathway for red emission.

3.2.3.3. Up-conversion mechanism in silica thin film made with $Yb_{0.80}La_{0.15}Tb_{0.05}F_3$ nanoparticles

Figure 3.16a shows the up-conversion emission spectrum of silica sol-gel thin film made with $Yb_{0.80}La_{0.15}Tb_{0.05}F_3$ nanoparticles, in which the most intense peak at 545 nm corresponds to $^5D_4$ to $^7F_5$ transition, and the peaks at 488, 586, 623, and 660 nm correspond to the $^5D_4$ to $^7F_6$, $^7F_4$, $^7F_3$, and $^7F_2$ transitions, respectively. The peaks at 413,

435 nm corresponds to $^5G_6/^5D_3$ to $^7F_5$ and $^7F_4$ transitions, respectively. The effective lifetime of the $^5D_4$ level is 2.0 ms (τ_R = 4.9 ms [50]) and the $^5G_6/^5D_3$ level is 1.7 ms. The temporal evolution of the 545 nm emission is shown in Figure 3.16b with a rise time of 2.0 ms and a decay time of 1.9 ms. Additionally, the temporal evolution of the 413 nm emission is similar to the 545 nm emission temporal evolution graph with a rise of 1.9 ms and a decay of 1.8 ms (data not shown). The rise time of ~2 ms in both the evolution graphs matches with the lifetime of the $^5D_4$ level of Tb^{3+} ion and clearly suggests that the $^5D_4$ level is the key level in the rate determining step, which is populated through co-operative up-conversion process. Furthermore, the decay of 545 nm emission deduced from the temporal evolution graph is consistent with the decay measured using the optical parametric oscillator (OPO) excitation at 980 nm.

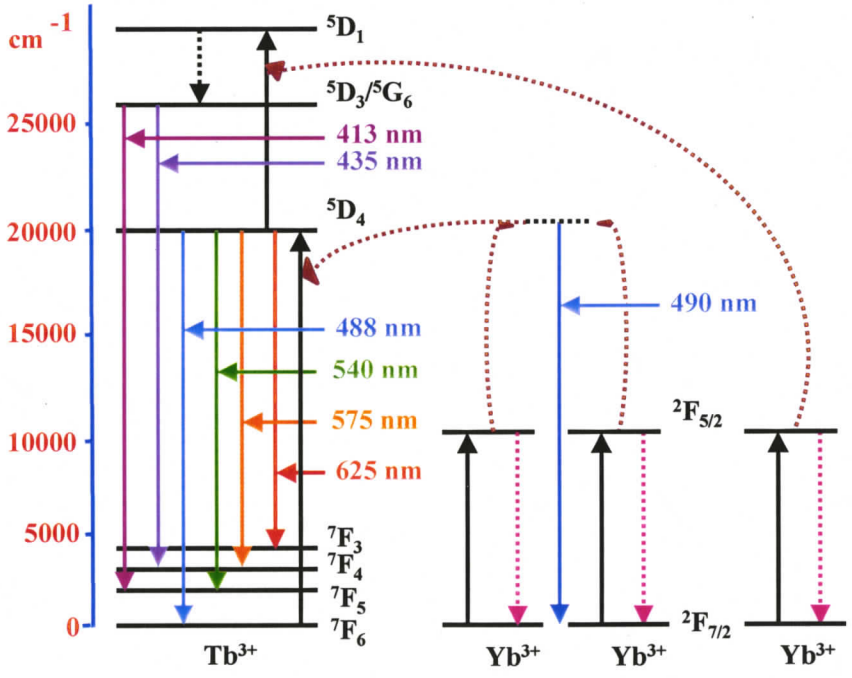

Figure 3.15. Energy level of Tb^{3+} and Yb^{3+} ions as well as the up-conversion mechanisms.

Figure 3.17c shows the dependence of the up-conversion emission intensity on the excitation power in silica thin film individually made with $Yb_{0.80}La_{0.15}Tb_{0.05}F_3$ nanoparticles. Blue and green emission from Tb^{3+} ions are both three-photon processes because the slope of both the green and blue emission is around 3. Figure 3.15 demonstrates the up-conversion energy transfer mechanism between Tb^{3+} and Yb^{3+} ions. Initially, Yb^{3+} ions are excited to the $^2F_{5/2}$ level through absorption of the 980 nm excitation. Subsequently, two of these excited Yb^{3+} ions interact with each other to reach a virtual state at 490 nm by co-operative up-conversion energy transfer process and transfer their energy to a Tb^{3+} ion in the ground state, there by exciting it to the $^5D_4$ level. Immediately following this process, the excited Tb^{3+} ion in the $^5D_4$ level is excited to the $^5D_1$ level through a subsequent energy transfer process from the excited Yb^{3+} ion. Subsequently, the excited Tb^{3+} ion relaxes to the $^5G_6/^5D_3$ level through multiphonon relaxation after which the blue emission at 413 and 435 nm takes places. Alternatively, it can relax to the $^5D_4$ level where by the 488, 545, 585, 625, and 660 nm emissions take place. This mechanism pathway requires three photons to get the blue, green, and red emission, which is well supported by the slope of three from the power dependence graph (Figure 3.17c).

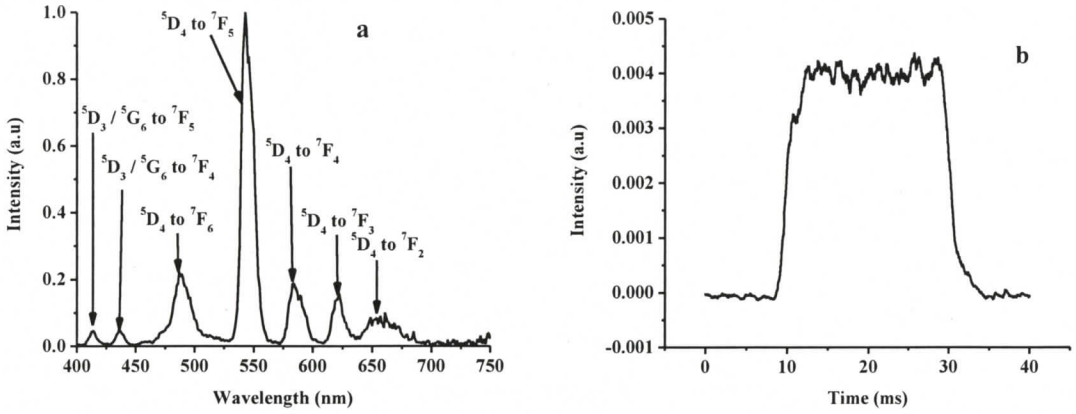

Figure 3.16. Silica thin film prepared at 800 °C made with $Yb_{0.80}La_{0.15}Tb_{0.05}F_3$ nanoparticles under 300 mW 980 nm CW laser excitation, a) Up-conversion emission spectrum b) Temporal evolution of green emission through up-conversion.

In principle, the green emission could be a two-photon process and indeed researchers have demonstrated the blue emission as a three-photon process and green emission as a two-photon process. The observation of relatively strong blue emission and the slope of power dependence graph of both green and blue emission clearly suggest that the up-conversion transition of the $^5D_4$ level to the $^5G_6/^5D_3$ level through an energy transfer from one Yb^{3+} to a Tb^{3+} in the $^5D_4$ excited state is much more efficient than the co-operative up-conversion of the $^7F_6$ level to the $^5D_4$ level. Moreover, the long lifetime of the $^5D_4$ level favours the extra up-conversion energy transfer process.

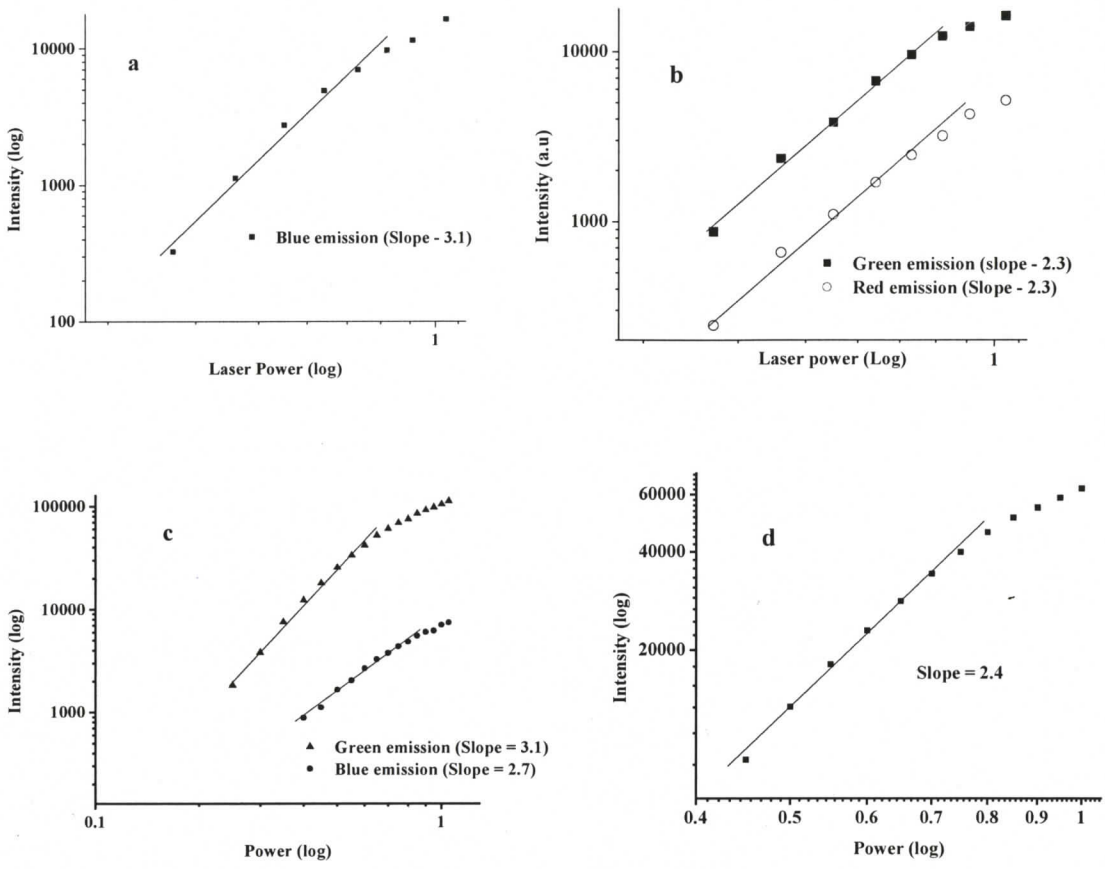

Figure 3.17. Dependence of the up-conversion emission intensity on the excitation power in silica thin film prepared at 800 °C made with a) $La_{0.75}Yb_{0.20}Ho_{0.05}F_3$, b) $La_{0.75}Yb_{0.20}Tm_{0.05}F_3$, c) $Yb_{0.75}La_{0.20}Tb_{0.05}F_3$, d) $Yb_{0.75}La_{0.20}Eu_{0.05}F_3$ nanoparticles under 980 nm excitation.

3.2.3.4. Up-conversion mechanism in silica thin film made with $Yb_{0.80}La_{0.15}Eu_{0.05}F_3$ nanoparticles

The temporal evolution of the 612 nm emission is shown in Figure 3.18 with a rise time of 3.0 ms and a decay time 3.2 ms. The rise time of ~3.0 ms matches with the lifetime of the $^5D_0$ level which clearly suggests that the $^5D_0$ level is the key level in the rate determining step which is populated through co-operative up-conversion process.

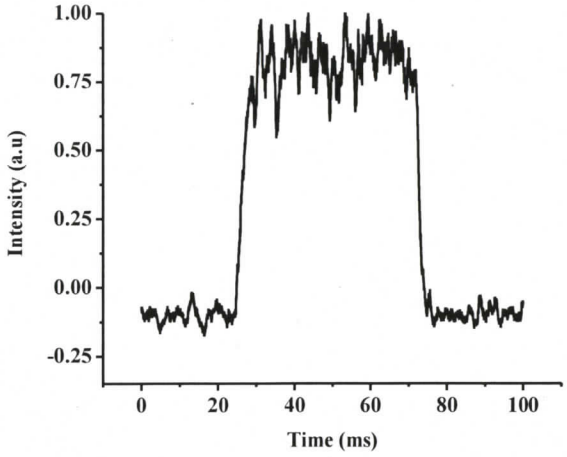

Figure 3.18. Temporal evolution of red emission through up-conversion from silica thin film prepared at 800 °C made with $Yb_{0.80}La_{0.15}Eu_{0.05}F_3$ nanoparticles under 300 mW 980 nm CW laser excitation.

The dependence of the up-conversion emission intensity on the excitation power in silica film individually made with $Yb_{0.80}La_{0.15}Eu_{0.05}F_3$ nanoparticles is shown in Figure 3.17d with a slope ~2. This clearly demonstrates that the red emissions from Eu^{3+} ions are two-photon process. Figure 3.19 shows the up-conversion energy transfer pathway between Eu^{3+} and Yb^{3+} ions. Initially Yb^{3+} ions are excited to the $^2F_{5/2}$ level via 980 nm photons through CW laser excitation. Subsequently, two of these excited Yb^{3+} ions interact with each other to reach a virtual state at 490 nm by co-operative up-conversion energy transfer process and transfer its energy to a Eu^{3+} ion in the ground state, thereby exciting it to the $^5D_1$ level. This then relaxes quickly to the $^5D_0$ level from which the 591 and 612 nm emissions occur.

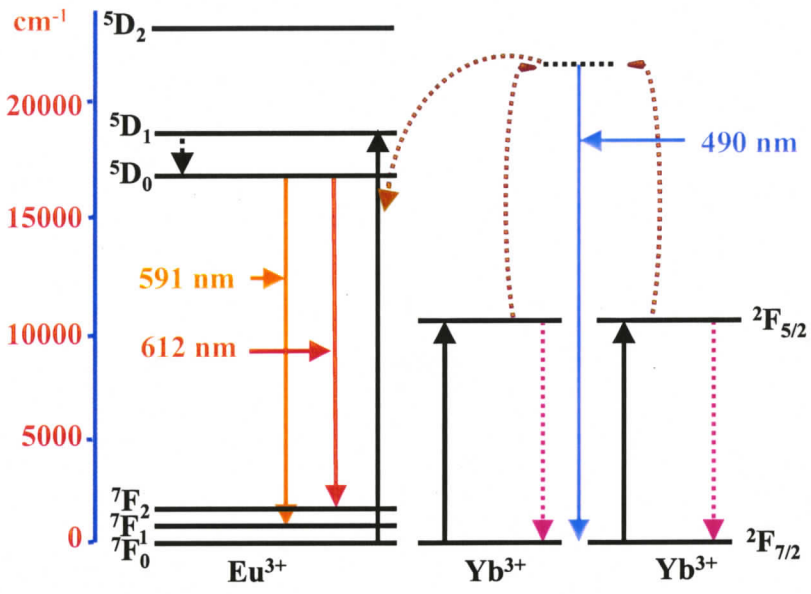

Figure 3.19. Energy level of Eu^{3+} and Yb^{3+} ions as well as the up-conversion mechanisms.

3.2.3.5. Up-conversion mechanism in silica thin film made with $La_{0.45}Yb_{0.50}Er_{0.05}F_3$ nanoparticles

The green and red emission from Er^{3+} ions are predominantly due to newly described cross-relaxation-enhanced energy-transfer (*hetero*-LEET) up-conversion process, which exhibits a power dependence *similar* to that of a photon-avalanche (PA). The *hetero*-LEET mechanism is potentially more efficient than PA, ground state absorption/excited state absorption (GSA/ESA), and energy-transfer (ETU) mechanisms because it combines the advantages of resonant ground-state absorption of the pump beam and an ETU-based up-conversion with an avalanche-like looping mechanism that enhances the population of the reservoir levels. This mechanism is discussed in detail in chapter 4.

3.2.4 Efficiency of energy transfer

The efficiency of energy transfer (η_τ) can be calculated from Yb^{3+} to Ln^{3+} ions using the equation (1)

$$\eta_\tau = 1 - \frac{\tau_{DA}}{\tau_D} \qquad \text{---------- (1)}$$

Where $\boldsymbol{\tau}_{DA}$ is the lifetime of donor (Yb^{3+}) in the presence of an acceptor (Ln^{3+}) and $\boldsymbol{\tau}_D$ is the lifetime of donor in the absence of an acceptor (Y^{3+}). The lifetime of Yb^{3+} ion (donor) in the absence of an acceptor lanthanide ion was obtained for a control silica sol-gel thin film made with $La_{0.45}Yb_{0.50}Y_{0.05}F_3$ nanoparticles. The Y^{3+} ion does not posses any optical properties and mimics the doping of Ln^{3+} (Ln = Er, Tm, Ho, Tb and Eu) ion. The effective lifetime of the $^2F_{5/2}$ level of Yb^{3+} ions in the silica thin film incorporated with $La_{0.45}Yb_{0.50}Y_{0.05}F_3$ nanoparticles is 1.1 ms (Figure 3.20a). Lifetimes of Yb^{3+} ions when it is co-doped with Er^{3+} (Figure 3.20b), Ho^{3+} and Tm^{3+} are 428 μs, 475 μs, and 600 μs, respectively. Thus, the efficiency of energy transfer to Er^{3+}, Ho^{3+} and Tm^{3+} are determined to be 0.6, 0.6 and 0.5, respectively. The lifetime of the $^2F_{5/2}$ level of Yb^{3+} ions in the silica thin film individually incorporated with $Yb_{0.75}La_{0.20}Tb_{0.05}F_3$ and $Yb_{0.75}La_{0.20}Eu_{0.05}F_3$ nanoparticles are 850 μs and 630 μs, respectively. Thus, the efficiency of the energy transfer from Yb^{3+} to Tb^{3+} ions and Yb^{3+} to Eu^{3+} ions were determined to be 0.37 and 0.15, respectively. This efficiency of energy transfer is substantially less than the energy transfer to Er^{3+}, Ho^{3+}, and Tm^{3+}, which is consistent with the corresponding up-conversion mechanisms.

The effective lifetime $^1G_4$ level of Tm^{3+} ions and $^5S_2$ level of Ho^{3+} ions in the sample was found to be 300 μs and 378 μs, respectively. The effective lifetime of $^4S_{3/2}$ level and $^4F_{9/2}$ level of Er^{3+} ions are found to be 525 μs and 418 μs, respectively. The effective lifetime of $^5D_0$ level of Eu^{3+} and $^5D_4$ level of Tb^{3+} ions was found to be 2.8 ms and 2.0 ms, respectively. The effective lifetimes and radiative lifetimes (Table 3.4) of above lanthanide ions suggest that the estimated quantum yield of resulting white light is on the order of 50%. Thus, the efficiency of the resulting white light is on the order of 12.5%. In other words, for every 8-NIR photons (980 nm) absorbed, two-photons lead to one up-converted photon in the visible region.

Table 3.4. Radiative and effective lifetimes of lanthanide ions

Lanthanide ions	**Radiative lifetimes**	**Effective lifetimes**[a]
Er^{3+} - $^4S_{3/2}$ level	778 μs[51]	525 μs
Er^{3+} - $^4F_{9/2}$ level	1.436 ms[51]	418 μs
Tm^{3+} - $^1G_4$ level	837 μs[52]	300 μs
Ho^{3+} - $^5S_2$ level	489 μs[52]	378 μs
Eu^{3+} - $^5D_0$ level	6.7 ms[53]	2.8 ms
Tb^{3+} - $^5D_4$ level	4.9 ms[50]	2.0 ms

[a] The effective lifetimes deduced from the decay measured by excitation at 980 nm (up-conversion) is consistent within experimental error, with the decay measured by down-conversion.

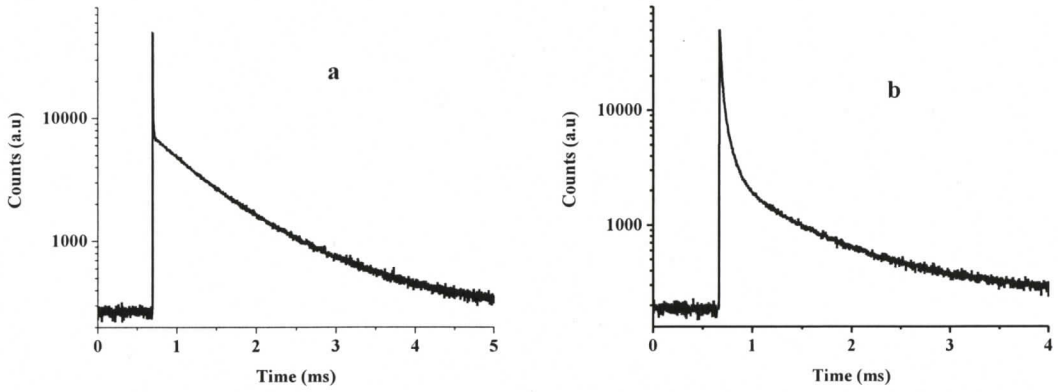

Figure 3.20 a) Decay curves for a) $La_{0.45}Yb_{0.5}Y_{0.05}F_3$, b) $La_{0.45}Yb_{0.5}Er_{0.05}F_3$ nanoparticles individually incorporated in silica film and heated at 800 °C (λ_{ex} = 940 nm, λ_{em} = 980 nm, excitation source - OPO).

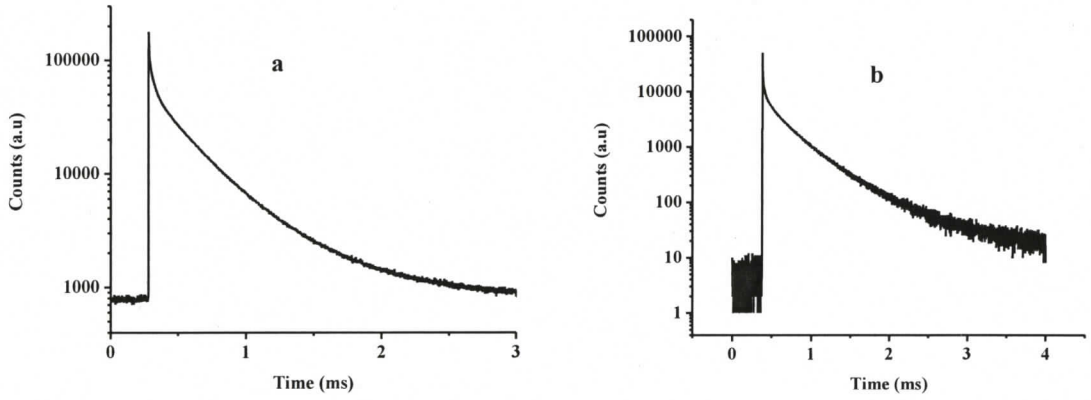

Figure 3.21 a) Decay curves for a) $La_{0.75}Yb_{0.20}Tm_{0.05}F_3$ (λ_{ex} = 980 nm, λ_{em} = 475 nm), b) $La_{0.45}Yb_{0.50}Ho_{0.05}F_3$ (λ_{ex} = 980 nm, λ_{em} = 542 nm) nanoparticles individually incorporated in silica film and heated at 800 °C (excitation source - OPO).

3.2.5. Conclusion

Part I of this chapter demonstrates the principle of incorporation of the three different Ln^{3+}/Yb^{3+} -doped nanoparticles in the sol-gel thin films to produce bright white light. Part II of this chapter shows an increase in the brightness and efficiency of generation of white light. The efficiency of generation of white light has been improved by replacing the inefficient Yb-Eu co-operative up-conversion processes with highly efficient Yb-Er and Yb-Ho energy transfer processes. 26-fold and 33-fold increase in the brightness and efficiency of white light emission has been generated from SiO_2 thin film made with nanoparticles of combination 1 (Yb/Er, Yb/Ho, and Yb/Tm) and combination 2, (Yb/Er and Yb/Tm) respectively, when compared to thin film in part I (Yb/Eu, Yb/Er, and Yb/Tm). Similar increase in the efficiency of white light generation was observed with ZrO_2 thin film made with these new combinations of nanoparticles, which further substantiates the generality of the approach.

3.2.6 Experimental Section

All chemicals were used as received without further purification. The lanthanide salts, $La(NO_3)_3.6H_2O$, $Er(NO_3)_3.5H_2O$, $Ho(NO_3)_3.5H_2O$, $Tm(NO_3)_3.5H_2O$ $Tb(NO_3)_3.5H_2O$, $Eu(NO_3)_3.5H_2O$, $Y(NO_3).6H_2O$, and $Yb(NO_3)_3.5H_2O$, all having a purity of 99.99%, and tetraethylorthosilicate (TEOS) (99.99%), zirconium propoxide (70 wt% solution in 1-propanol), NH_4OH_{aq} (35% wt% aqueous solution), and sodium fluoride (99%) were purchased from Aldrich. Citric acid (99%) was purchased from Caledon Laboratories Ltd.

3.2.6.1. Preparation of nanoparticles

$La_{0.75}Yb_{0.20}Tm_{0.05}F_3$, $La_{0.75}Yb_{0.20}Ho_{0.05}F_3$, $La_{0.45}Yb_{0.50}Er_{0.05}F_3$, $Yb_{0.75}La_{0.20}Er_{0.05}F_3$, $Yb_{0.75}La_{0.20}Tb_{0.05}F_3$, $Yb_{0.75}La_{0.20}Eu_{0.05}F_3$, and $La_{0.45}Yb_{0.50}Y_{0.05}F_3$ nanoparticles stabilised with citrate ligands were prepared by the co-precipitation technique in aqueous solution in presence of citrate ions. Around 2 g of citric acid and 0.126 g of sodium fluoride were dissolved in 40 ml of water. The pH of the solution was adjusted to ~6.0 by adding NH_4OH_{aq} and the solution was subsequently heated to 75 °C. Stoichiometric amounts of the nitrate salts of lanthanide ions were dissolved in 2 ml of methanol and added dropwise. A clear solution was obtained and after two hours of stirring, the reaction mixture was cooled to room temperature. Subsequently, 70 ml of ethanol was added to the reaction mixture to precipitate the nanoparticles. The particles were collected by centrifugation, washed twice with 5 ml of ethanol, and dried under vacuum. Formation of 5-6 nm citrate-stabilised nanoparticles was confirmed from ^{1}H NMR and AFM studies, which is consistent with our earlier reports.[37, 42]

3.2.6.2. NMR measurements

Room temperature ^{1}H NMR pattern was recorded using Bruker AC 300 instrument. The basic frequencies for the ^{1}H nucleus is 300.13 MHz. ^{1}H NMR chemical shift of $La_{0.45}Yb_{0.50}Er_{0.05}F_3$ particles stabilised with citrate ligands δ (D_2O) : 2.45 - 2.60 (broad, $C\underline{H_2}COOH - COH(COOH) - C\underline{H_2}COOH$).

3.2.6.3. Preparation of silica sol-gel thin films

The amounts of citrate stabilised lanthanide-doped nanoparticles used for different combinations to make thin films, which produced white light, is given in the Table 3.1. The relative amounts of nanoparticles were deduced from 4-5 trials. These nanoparticles were dissolved in 2 ml water, which was then mixed with 6 ml of tetraethoxyorthosilane (TEOS) and 15 ml of ethanol. The pH of the solution was adjusted to 2 by adding few drops of 0.1 N HCl and the solution was stirred for 24 h to get a clear sol. The sol was then spin-coated on a quartz substrate at 2500 rpm and heated to 400°C from 25°C in 1.40 h, staying at 400°C for 30 min and then heated to 800 °C in 2 h and staying at 800 °C for 12 h under ambient environment. The concentration of nanoparticles incorporated in the thin film is reported in Table 3.1. The films were transparent to visible light and no cracks were observed under an optical microscope. The thickness evolution of the films with annealing temperatures and variation of refractive index of the films with particles concentrations have been discussed in a recent publication.[54]

3.2.6.4. Preparation of ZrO_2 sol-gel thin films

The amounts of citrate-stabilised lanthanide-doped nanoparticles used for different combinations to make thin films which produced white light is given in the Table 3.1. A solution of the zirconium propoxide (3 ml) was dissolved in 9 ml of ethanol and followed by the addition of 0.5 ml of concentrated HCl. Prescribed amounts of nanoparticles were dissolved in 2 ml distilled water and added dropwise. The solution was stirred for 24 h to get a clear sol. The sol was then spin-coated on a quartz substrate at 2500 rpm and heated

to 400 °C from 25 °C in 1.40 hr, staying at 400 °C for 30 min, and then heated to 800 °C in 2 h and staying at 800 °C for 12 h under ambient environment.

3.2.6.5. Luminescence studies

Fluorescence analyses were done using an Edinburgh Instruments FLS 920 fluorescence system. The excitation source used for up-conversion was a Coherent 2-pin 980 nm CW semiconductor diode laser with P_{max} = 800 mW at 1000 mA. The diode is coupled to 100 μm (core) fiber. All emission analyses in the visible region were measured with a 1 nm resolution. All spectra were corrected for detection sensitivity. Lifetime analyses were done by exciting the solution with a 10 Hz Q-Switched Quantel Brilliant, in which the third harmonic of the Nd:YAG laser pumps the optical parametric oscillator (OPO), with an optical range from 410 to 2400 nm. The emissions were collected by using a red-sensitive Peltier-cooled Hamamatsu R955 photomultiplier tube (PMT), with a photon-counting interface and were used for analyses between 200 and 900 nm. Decay curves were measured with a 0.01 ms lamp trigger delay for the R955 PMT. Effective lifetimes were calculated using Origin software (version 7.0) based on the equation, [55]

$$\tau_{eff} = \frac{\int_0^\infty t\, I(t)\,dt}{\int_0^\infty I(t)\,dt}$$

Intensities down to 1% of the initial intensities were included in these lifetime analysis. Temporal evolution analysis were done with an optical chopper operated at 8 Hz

by chopping the 980 nm CW laser light and the signals were collected by using an oscilloscope. Rise and decay times were also calculated from the temporal evolution graphs by fitting with a single exponential using Origin software (version 7.0). All the calculations were done based on duplicate measurements and the values are within an error of ~10%. For consistency, all the thin film materials scratched from the quartz plate and 15 mg of materials was mixed with 15 mg of KBr to make uniform pellets and the emission intensities over the whole area of the pellet were same within experimental error. The CIE colour co-ordinates of combination 4 were calculated by neglecting Er^{3+} impurities emission.

3.2.6.6. Calculation of relative efficiency

All samples were measured under identical experimental conditions. Relative efficiency of current thin films was calculated based on the area under the emission peaks and scaled to the concentration of Yb^{3+} ions.

3.2.6.7. Calculation of quantum yield

Quantum yield of all the samples were estimated by using the following formula.

$$\text{quantum yield}, \phi = \frac{\tau_{obs}}{\tau_{rad}}$$

Where,

τ_{obs} = observed lifetime and τ_{rad} = radiative lifetime.

3.2.6.8. Calculation of CIE colour co-ordinates

CIE colour co-ordinates were calculated by using the software CIE colour matching linear algebra software.[40, 41]

References

(1) Adachi, C.; Baldo, M. A.; Thompson, M. E.; Forrest, S. R. *J. Appl. Phys.* **2001**, *90*, 5048.

(2) http:/www.cdtltd.co.uk.

(3) http:/www.kodak.com/go/OLED.

(4) Cheng, J. A.; Chen, C. H. *J. Mater. Chem.* **2005**, *15*, 1179.

(5) Tang, C. W.; Vanslyke, S. A. *Appl. Phys. Lett.* **1987**, *51*, 913.

(6) Chen, C. T. *Chem. Mater.* **2004**, *16*, 4389.

(7) Sheats, J. R. *Science* **1997**, *277*, 191.

(8) Park, J. H.; Lee, T. W.; Kim, Y. C.; Park, O. O.; Kim, J. K. *Chem. Phys. Lett.* **2005**, *403*, 293.

(9) Suzuki, M.; Hatakeyama, T.; Tokito, S.; Sato, F. *IEEE. J. Sel. Top. Quant. Electron.* **2004**, *10*, 115.

(10) Bernius, M. T.; Inbasekaran, M.; O'Brien, J.; Wu, W. S. *Adv. Mater.* **2000**, *12*, 1737.

(11) Wu, C. C.; Lin, Y. T.; Wong, K. T.; Chen, R. T.; Chien, Y. Y. *Adv. Mater.* **2004**, *16*, 61.

(12) Yeh, S. J.; Wu, M. F.; Chen, C. T.; Song, Y. H.; Chi, Y.; Ho, M. H.; Hsu, S. F.; Chen, C. H. *Adv. Mater.* **2005**, *17*, 285.

(13) Zhang, X. H.; Liu, M. W.; Wong, O. Y.; Lee, C. S.; Kwong, H. L.; Lee, S. T.; Wu, S. K. *Chem. Phys. Lett.* **2003**, *369*, 478.

(14) Service, R. F. *Science* **2005**, *310*, 1762.

(15) Chuen, C. H.; Tao, Y. T. *Appl. Phys. Lett.* **2002**, *81*, 4499.

(16) Duggal, A. R.; Foust, D. F.; Nealon, W. F.; Heller, C. M. *Appl. Phys. Lett.* **2003**, *82*, 2580.

(17) Zhou, X.; He, J.; Liao, L. S.; Lu, M.; Ding, X. M.; Hou, X. Y.; Zhang, X. M.; He, X. Q.; Lee, S. T. *Adv. Mater.* **2000**, *12*, 265.

(18) Feldmann, C.; Justel, T.; Ronda, C. R.; Schmidt, P. J. *Adv. Funct. Mater.* **2003**, *13*, 511.

(19) Wright, J. C. *Top. Appl. Phys.* **1976**, *15*, 239.

(20) D'Andrade, B. W.; Forrest, S. R. *Adv. Mater.* **2004**, *16*, 1585.

(21) Heer, S.; Kompe, K.; Güdel, H. U.; Haase, M. *Adv. Mater.* **2004**, *16*, 2102.

(22) Vetrone, F.; Boyer, J. C.; Capobianco, J. A.; Speghini, A.; Bettinelli, M. *J. Phys. Chem. B* **2003**, *107*, 1107.

(23) Vetrone, F.; Boyer, J. C.; Capobianco, J. A.; Speghini, A.; Bettinelli, M. *J. Appl. Phys.* **2004**, *96*, 661.

(24) Guo, H.; Dong, N.; Yin, M.; Zhang, W. P.; Lou, L. R.; Xia, S. D. *J. Phys. Chem. B* **2004**, *108*, 19205.

(25) Patra, A. *Chem. Phys. Lett.* **2004**, *387*, 35.

(26) Patra, A.; Friend, C. S.; Kapoor, R.; Prasad, P. N. *J. Phys. Chem. B* **2002**, *106*, 1909.

(27) De la Rosa, E.; Salas, P.; Desirena, H.; Angeles, C.; Rodriguez, R. A. *Appl. Phys. Lett.* **2005**, *87*.

(28) Maciel, G. S.; Biswas, A.; Prasad, P. N. *Opt. Commun.* **2000**, *178*, 65.

(29) Sudarsan, V.; van Veggel, F.; Herring, R. A.; Raudsepp, M. *J. Mater. Chem.* **2005**, *15*, 1332.

(30) Stouwdam, J. W.; van Veggel, F. *Langmuir* **2004**, *20*, 11763.

(31) Stouwdam, J. W.; van Veggel, F. *Nano Lett.* **2002**, *2*, 733.

(32) Stouwdam, J. W.; Hebbink, G. A.; Huskens, J.; van Veggel, F. *Chem. Mater.* **2003**, *15*, 4604.

(33) Hebbink, G. A.; Stouwdam, J. W.; Reinhoudt, D. N.; van Veggel, F. *Adv. Mater.* **2002**, *14*, 1147.

(34) Diamente, P. R.; van Veggel, F. *J. Fluor.* **2005**, *15*, 543.

(35) Diamente, P. R.; Burke, R. D.; van Veggel, F. C. J. M. *Langmuir* **2006**, *22*, 1782.

(36) Slooff, L. H.; de Dood, M. J. A.; van Blaaderen, A.; Polman, A. *J. Non-Cryst. Solids* **2001**, *296*, 158.

(37) Sudarsan, V.; Sivakumar, S.; van Veggel, F. C. J. M.; Raudsepp, M. *Chem. Mater.* **2005**, *17*, 4736.

(38) Dekker, R.; Sudarsan, V.; van Veggel, F. C. J. M.; Worhoff, K.; A., D. *Proceedings symposium IEEE/LEOS Benelux Chapter, Ghent* **2004**, 295.

(39) Aebischer, A.; Heer, S.; Biner, D.; Kramer, K.; Haase, M.; Güdel, H. U. *Chem. Phys. Lett.* **2005**, *407*, 124.

(40) http://www.awitness.org/delphi_pascal_tutorial/index.html.

(41) http://www.brucelindbloom.com/index.html?ColorCalcHelp.html.

(42) Sivakumar, S.; van Veggel, F. C. J. M.; Raudsepp, M. *J. Am. Chem. Soc.* **2005**, *127*, 12464.

(43) Kido, J.; Kimura, M.; Nagai, K. *Science* **1995**, *267*, 1332.

(44) Kido, J.; Shionoya, H.; Nagai, K. *Appl. Phys. Lett.* **1995**, *67*, 2281.

(45) Kanno, H.; Sun, Y.; Forrest, S. R. *Appl. Phys. Lett.* **2005**, *86*.

(46) Shen, Z. L.; Burrows, P. E.; Bulovic, V.; Forrest, S. R.; Thompson, M. E. *Science* **1997**, *276*, 2009.

(47) Mueller, A. H.; Petruska, M. A.; Achermann, M.; Werder, D. J.; Akhadov, E. A.; Koleske, D. D.; Hoffbauer, M. A.; Klimov, V. I. *Nano Lett.* **2005**, *5*, 1039.

(48) Ostermay, F. W.; Vanuiter, L. G. *Phys. Rev. B* **1970**, *1*, 4208.

(49) Salley, G. M.; Valiente, R.; Güdel, H. U. *Phys. Rev. B* **2003**, *67*, 134111.

(50) Binnemans, K.; Van Deun, R.; Gorller-Walrand, C.; Adam, J. L. *J. Non-Cryst. Solids* **1998**, *238*, 11.

(51) Sosa, R.; Foldvari, I.; Watterich, A.; Munoz, A.; Maillard, R. S.; Kugel, G. *J. Lumin.* **2005**, *111*, 25.

(52) Walsh, B. M.; Barnes, N. P.; Di Bartolo, B. *J. Appl. Phys.* **1998**, *83*, 2772.

(53) Werts, M. H. V.; Jukes, R. T. F.; Verhoeven, J. W. *Phys. Chem. Chem. Phys.* **2002**, *4*, 1542.

(54) R. Dekker, V. Sudarsan, F. C. J. M. van Veggel, D. Worhoff, A. Drissen, Prceedings symposium IEEE.LEOS Benelux Chapter, Ghent, 2004, 295

(55) Cannas, C.; Casu, M.; Mainas, M.; Musinu, A.; Piccaluga, G.; Polizzi, S.; Speghini, A.; Bettinelli, M. *J. Mater. Chem.* **2003**, *13*, 3079.

CHAPTER 4

Near-infrared (NIR) to red and green up-conversion emission from silica sol-gel thin films made with $La_{0.45}Yb_{0.50}Er_{0.05}F_3$ nanoparticles, *hetero*-looping-enhanced energy-transfer (*hetero*-LEET): A new up-conversion process*©

---

* The major part of the work in this chapter has been accepted for publication:

Sri Sivakumar, Frank C.J.M. van Veggel, Stanley P. May, *J. Am. Chem. Soc.*, in press.

4.1. Introduction

Lanthanide-based up-conversion phosphors have been investigated for a wide range of potential applications, such as display monitors, fluorescence imaging for detection of biomolecules, optical data storage, LCD back lighting, and compact solid-state lasers.[1-6] Research in this area has intensified due to the recent development of lanthanide-doped oxide[3,5,7-11] and fluoride nanoparticles[12-15] that exhibit NIR-to-visible up-conversion emission. Nanocrystalline up-conversion phosphors can be incorporated into a broad range of materials and devices, and are suitable for sensing at the molecular scale.[7,12] At present, low efficiency is the most important limiting factor in the practical use of up-conversion phosphors.[16] There are three major mechanisms available for up-conversion luminescence (Figure 4.1): A) ground-state absorption followed by excited-state absorption (GSA/ESA); B) sequential energy-transfer events from donors to the up-converting acceptor (ETU);.[17] and C) photon-avalanche (PA).[17-19] In the PA mechanism (Figure 4.1c), the intermediate reservoir level is initially populated through a very weak ground-state absorption (GSA), followed by resonant excited state absorption (ESA), or energy transfer from another excited ion, to populate the upper level, from which up-conversion luminescence occurs. After this initial 'seeding' process, efficient cross-relaxation (CR) populates the reservoir levels of neighbouring ions to produce two ions in the key reservoir level. A feedback, or 'looping,' cycle of ESA (or energy transfer) followed by cross relaxation then ensues, leading eventually to a substantial population of the reservoir level, and, therefore, to strong up-conversion emission. Lupei[20] has demonstrated a sensitized photon-avalanche mechanism (Figure 4.1d) in which the cross-relaxation (Pr^{3+}-Yb^{3+}) populates the key intermediate level of sensitizer ion (Yb^{3+}).

Immediately following this process, the excited sensitizer ion gives back its energy to the neighbouring acceptor ion (Pr^{3+}) to populate the key reservoir level and the looping starts. Lahoz *et al.*[21] have reported similar sensitized photon-avalanche mechanism in Ho^{3+}-Yb^{3+} co-doped fluoroindate glasses. They have estimated that the efficiency of sensitized photon-avalanche is three-fold higher than the photon-avalanche mechanism.

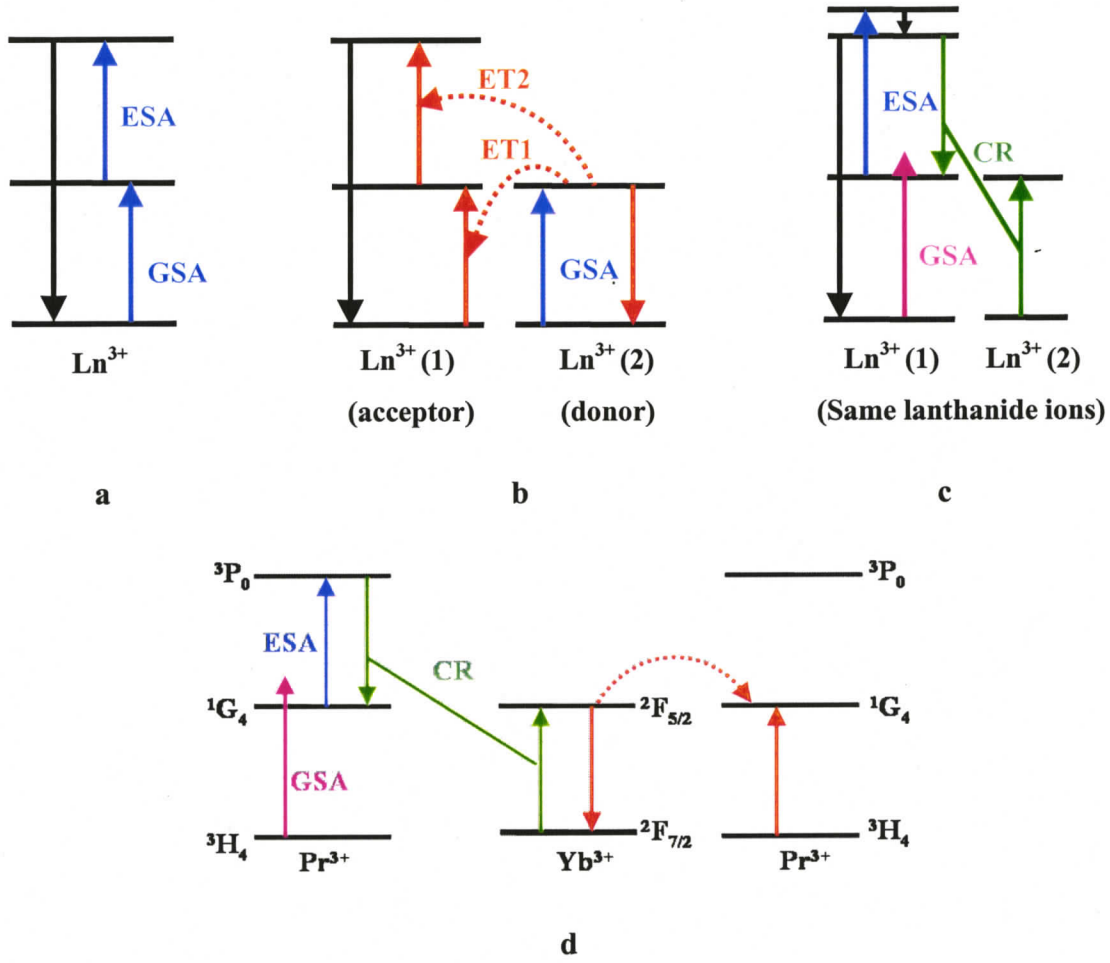

Figure 4.1. Schematic diagram of classical up-conversion mechanisms a) ground-state absorption/excited-state absorption (GSA/ESA), b) energy-transfer up-conversion (ETU) c) photon-avalanche (PA), d) sensitized photon-avalanche.

Although photon-avalanche mechanisms can be relatively efficient, they suffer from a number of drawbacks. Maximum output is limited because of the weak ground state absorption,[22] and high pump powers are usually needed to reach the threshold condition. In addition, because many looping cycles are required to achieve avalanche, the rise time in the temporal evolution of the up-conversion emission is generally much longer (up to seconds) than the lifetimes of any of the excited states involved. This can be a disadvantage in lighting and display applications, because it will take seconds to reach maximum output. However, up-converting phosphors based on these classical mechanisms have successfully been applied in photonic applications there is still room for improvement in the efficiency of up-conversion.

The Er^{3+} ion is quite suitable ion for up-conversion because of its favourable electronic energy levels and its long-lived excited states ($^4I_{9/2}$ and $^4I_{13/2}$ levels) can easily be populated through NIR radiation. ESA[8,10,11] and ET[7,9,12,18] up-conversion processes are very common in Er^{3+}-doped materials, whereas the photon-avalanche process is relatively rare. Auzel and co-workers have reported the generation of green emission through a photon-avalanche process in Er^{3+}-doped $LiYF_4$ single crystals[23] and ZBLAN (ZrF_4-BaF_2-LaF_3-AlF_3-NaF) fiber materials,[24,25] which are potential materials for up-conversion lasers. These materials were excited with 579, 690, and 700 nm lasers. Scheps[17] has described the generation of green emission through a photon-avalanche from $YAlO_3$ single crystals doped with Er^{3+} ions by exciting with 706 or 796 nm lasers. Bell *et al.*[26] have demonstrated photon-avalanche green emission from Er^{3+} doped fluoroindategallate glasses by using a 833 nm laser. Rakov and co-workers[27] have reported green emission through photon-avalanche up-conversion of 633.5 nm from Er^{3+} doped fluoroindate

glasses. However, there are no reports available on generation of green and red emission through photon-avalanche process from Er^{3+}- doped nanosized materials and Yb^{3+}/Er^{3+}-doped materials.

In this chapter, efficient generation of bright green and red light through up-conversion of 980 nm light from silica sol-gel thin films made with $La_{0.45}Yb_{0.50}Er_{0.05}F_3$ nanoparticles at room temperature is reported (Scheme 4.1). This process occurs via a new, potentially more efficient up-conversion mechanism, called hetero-looping-enhanced (*hetero*-LEET) energy-transfer up-conversion. This mechanism combines the advantages of resonant ground-state absorption of the pump beam and an ETU-based up-conversion with an avalanche-like looping mechanism that enhances the population of the reservoir levels. The dependence of up-conversion emission intensity on pump power is similar to that seen for a classical photon-avalanche process. However, up-conversion emission is easily seen by naked eye using pump power of 4.5 W/cm^2 or less, even for dilute samples. In addition, the rise time of up-conversion emission is on the order of the lifetimes of the participating excited states of the Er^{3+} and Yb^{3+} ions.

Goldner *et al.*[22] have demonstrated a cross-relaxation-enhanced GSA/ESA up-conversion mechanism, which they call cross-relaxation enhanced excited state absorption (CRESA), in a Nd^{3+}-doped $LiYF_4$ single crystal. They have demonstrated that CRESA is more efficient than the photon-avalanche process because of the resonant GSA. However, CRESA has only been described in a single crystal and is based on the intrinsically less efficient GSA/ESA process. To the best of my knowledge, this is the first report on the generation of green and red emission from Yb^{3+}/Er^{3+}-doped materials

through a photon-avalanche-type process, and is the first report of feedback enhancement of an ETU mechanism.

4.2. Results and Discussion

Scheme 4.1 demonstrates the generation of red and green light from the silica sol-gel thin layer made with $La_{0.45}Yb_{0.50}Er_{0.05}F_3$ nanoparticles under 980 nm CW laser excitation through *hetero*-LEET up-conversion. Figure 4.2 shows a digital image of up-converted light (under 980 nm CW laser excitation) from the silica thin film made with $La_{0.45}Yb_{0.50}Er_{0.05}F_3$ nanoparticles. Bright light (which is green in appearance) can be seen very clearly from the thin film even at a laser power density of 4.5 W/cm^2. The insert left in Figure 4.2 shows the digital image of bright up-converted green light by filtering the red light and insert right shows bright up-converted red light by filtering the green light. The corresponding up-conversion emission spectrum is shown in Figure 4.3. The emission peaks at 515, 542 nm, and 660 nm are assigned to the $^2H_{11/2}\rightarrow{}^4I_{15/2}$, $^4S_{3/2}\rightarrow{}^4I_{15/2}$, and $^4F_{9/2}\rightarrow{}^4I_{15/2}$ transitions of Er^{3+} ion, respectively. Additionally, a very weak blue emission band at 410 nm was observed which is assigned to Er^{3+}: $^2G_{9/2}\rightarrow{}^4I_{15/2}$ transition (inset in Figure 4.3). The excitation spectra (Figure 4.4) of green and red emission through up-conversion show the typical absorption of Yb^{3+} ion, which clearly demonstrates that the up-conversion occurs from Er^{3+} ion through energy-transfer from Yb^{3+} to Er^{3+} ions (*i.e.* an ETU mechanism). The effective lifetime of $^4S_{3/2}$ (τ_{rad} = 778 μs[28]) and $^4F_{9/2}$ levels (τ_{rad} = 1.4 ms[28]) of Er^{3+} ions in the sample was found to be 525 μs (Figure 4.5a) and 418 μs (Figure 4.5b) respectively suggesting an estimated quantum yield of ~50%.

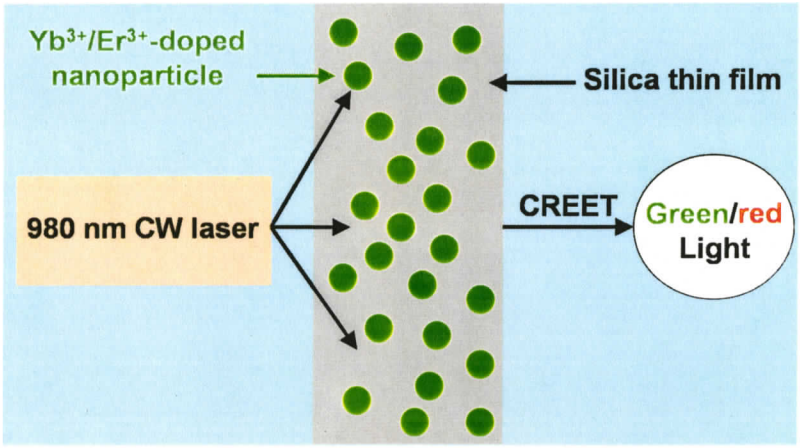

Scheme 4.1. Generation of Green/red light through *hetero*-LEET up-conversion process.

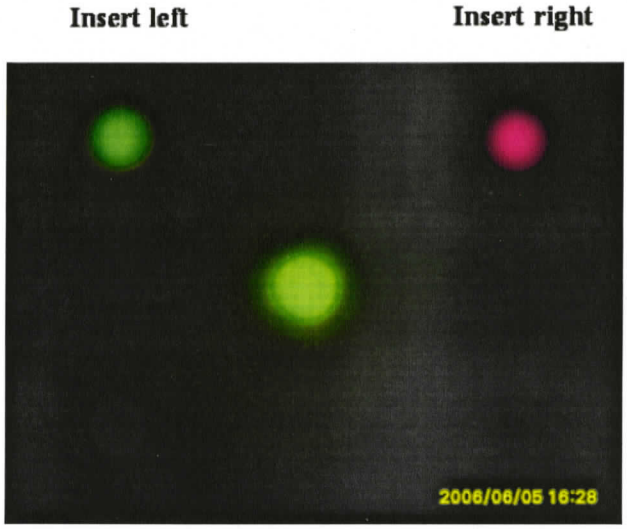

Figure 4.2. Digital photograph of up-conversion emission from silica sol-gel thin film prepared at 800 °C made with $La_{0.45}Yb_{0.50}Er_{0.05}F_3$ nanoparticles under 980 nm 4.5 W/cm^2 CW laser excitation (Insert left is up-converted green emission by filtering red emission and insert right is up-converted red emission by filtering green emission). Digital photographs were taken using a 800 nm low band pass filter to shield 980 nm laser light from the camera.

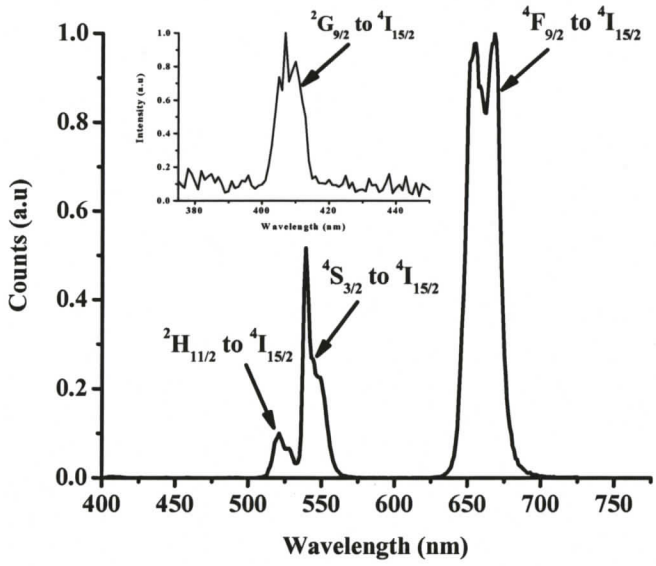

Figure 4.3. Up-conversion emission spectrum of silica thin film prepared at 800 °C made with $La_{0.45}Yb_{0.50}Er_{0.05}F_3$ nanoparticles under 980 nm 400 mW CW laser excitation (inset shows the weak blue emission from $^2G_{9/2}$ level of Er^{3+} ion).

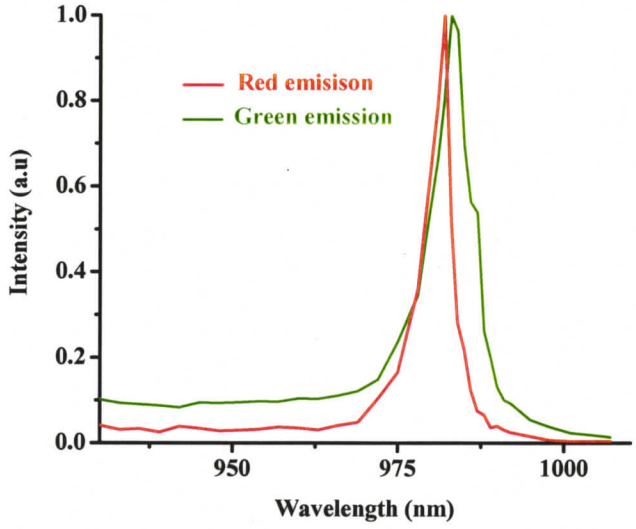

Figure 4.4. Excitation spectrum of silica thin film prepared at 800 °C made with $La_{0.45}Yb_{0.50}Er_{0.05}F_3$ nanoparticles (λ_{em} = 542 nm).

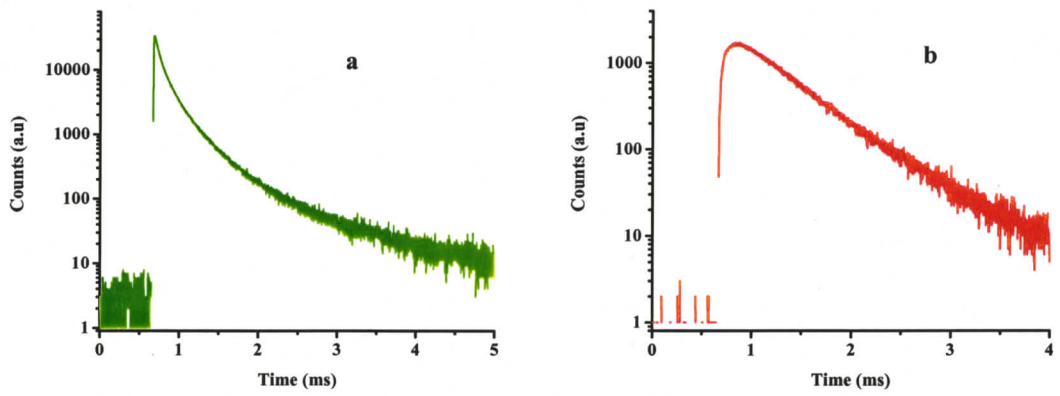

Figure 4.5. Decay curve of silica thin film prepared at 800 °C made with $La_{0.45}Yb_{0.50}Er_{0.05}F_3$ nanoparticles a) green emission ($^4S_{3/2}$ level), b) red emission ($^4F_{9/2}$ level).

Additionally very strong emission band at 1530 nm was observed and is assigned to Er^{3+}: $^4I_{13/2} \rightarrow {}^4I_{15/2}$ transition (Figure 4.6a) with an effective lifetime of 8.0 ms (Figure 4.6b) suggesting an estimated quantum yield of ~50% (τ_{rad} = 15 ms[28]).

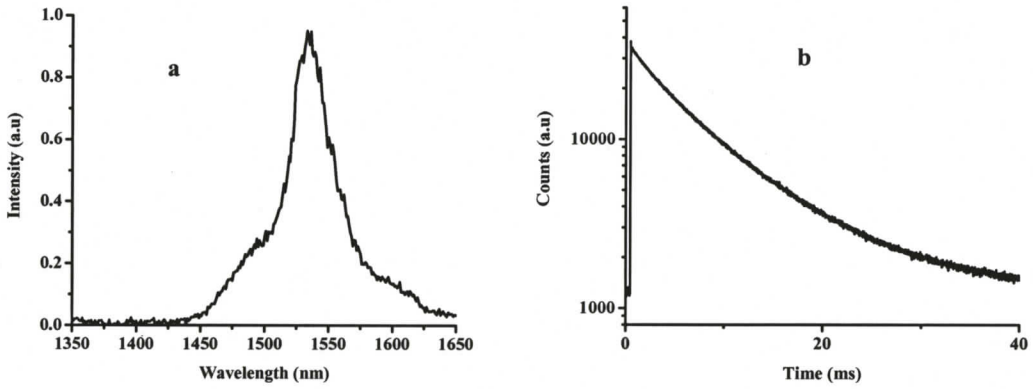

Figure 4.6. a) NIR emission spectrum of silica thin film prepared at 800 °C made with $La_{0.45}Yb_{0.50}Er_{0.05}F_3$ nanoparticles under 980 nm 400 mW CW laser excitation, b) decay curve of silica thin film prepared at 800 °C made with made with $La_{0.45}Yb_{0.50}Er_{0.05}F_3$ nanoparticles (λ_{ex} = 980 nm, λ_{em} = 980 nm, source = OPO).

Figure 4.7 plots the logarithm of up-conversion emission intensity vs. the logarithm of excitation power. At 4.5 W/cm^2 excitation power, the slopes of both the red and green emission increase rapidly with increasing excitation power, giving a maximum slope of ~8 at the feed back point. This is a strong evidence for an avalanche-type mechanism, as it is hard to envision an effective 8-photon process in this system that does not involve a repetitive feedback loop. Moreover, the nearly identical shapes of the red and green emission power-dependence graphs above 4.5 W/cm^2 pump power demonstrates that the same intermediate-state reservoir is involved in both up-conversion processes. In our earlier communication,[29] we had assigned the green and red emission to a two-photon process, because we had only measured the emissions at higher powers, at which the Er^{3+} ions were already partly in saturation. This lead incorrectly to a slope of ~2. Figure 4.8 shows the power dependence graph of 1530 nm emission with slope ~1. This clearly demonstrates that the 1530 nm emission is one-photon process.

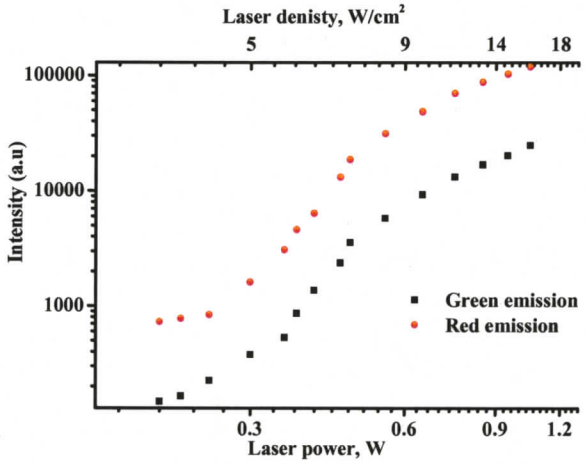

Figure 4.7. Dependence of the up-conversion emission intensity on 980 nm CW laser excitation power in silica thin film prepared at 800 °C made with $La_{0.45}Yb_{0.50}Er_{0.05}F_3$ nanoparticles.

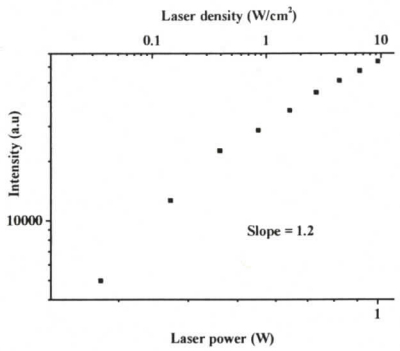

Figure 4.8. Dependence of the 1530 nm emission intensity on 980 nm CW laser excitation power in silica thin film prepared at 800 °C made with $La_{0.45}Yb_{0.50}Er_{0.05}F_3$ nanoparticles.

The temporal evolution (Figure 4.9) of red and green emission at the onset of 980 nm excitation exhibits a rise time of 5.7 and 3.0 ms, respectively. These rise times are on the order of the lifetimes of the metastable levels of Er^{3+} ions, and are considerably shorter than those typically observed in a classical PA mechanism. In addition, the rise time of red emission roughly matches the lifetime of the $^4I_{13/2}$ level of Er^{3+} (~8.0 ms) and suggests that the $^4F_{9/2}$ emitting level is populated *via* the $^4I_{13/2}$ level. Figure 4.10a shows the temporal evolution of red emission at different excitation powers of 980 nm laser. The risetimes are decreasing with an increase of the laser power, which is a typical characteristic of avalanche-type mechanism.[25] However, the green emission does not show this effect (Figure 4.10b). This may be due to a variation in the speed of optical chopper over time because the temporal evolution graph for green emission was measured after the red emission at different laser powers. The measurement took more than 1 h to finish the measurement for red emission and then the measurement for green emission was started. While starting the measurement, the speed of the optical chopper was stable

at 2.70 ± 0.1 Hz and it was stable for 45 min. Then the optical chopper slowly became unstable and the frequency changed from 2.6 to 2.8 Hz after 1 hr. Further investigations are required to resolve this issue.

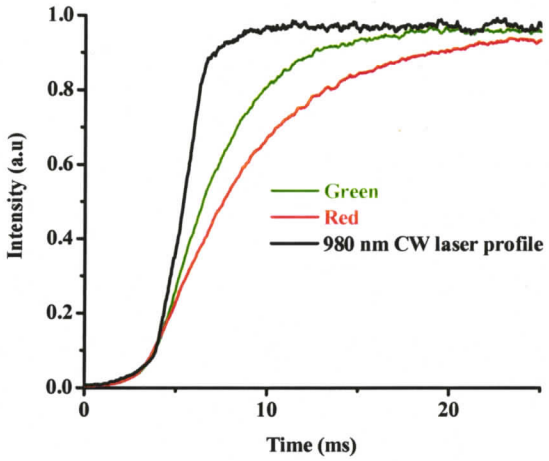

Figure 4.9. Temporal evolution of green emission through up-conversion from silica thin film prepared at 800 °C made with $La_{0.45}Yb_{0.50}Er_{0.05}F_3$ nanoparticles under 980 nm 4.5 W/cm^2 CW laser excitation.

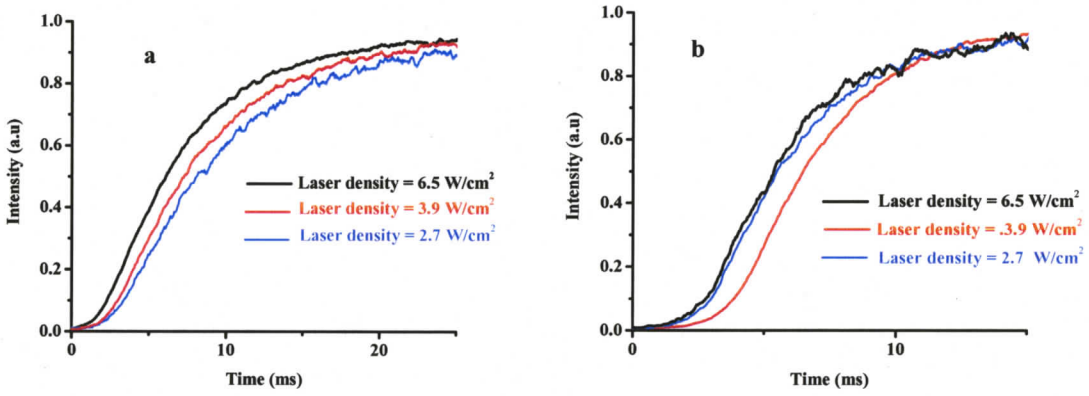

Figure 4.10. Temporal evolution of up-converted emission from silica thin film prepared at 800 °C made with $La_{0.45}Yb_{0.50}Er_{0.05}F_3$ nanoparticles under 980 nm excitation with different laser densities a) red emission b) green emission.

The proposed mechanism of *hetero*-looping-enhanced energy-transfer up-conversion (*hetero*-LEET) responsible for both red and green emission is illustrated schematically in Figure 4.11. Initially, sequential energy transfers from $Yb^{3+}(^2F_{5/2})$ ions (excited by 980 nm light) result in an Er^{3+} ion in the $^4F_{7/2}$ excited state (Figure 4.11a). Then, through multiphonon-assisted relaxation, the $^2H_{11/2}$ level of Er^{3+} is populated. The energy difference of ~1200 cm^{-1} is easily taken up by 3-4 phonons of the LaF_3 phase or 1-2 phonons of the lanthanum silicate phase (see below). Figure 4.11b then illustrates the critical step that begins the feedback loop. Multiphonon-assisted cross relaxation between $Er^{3+}(^2H_{11/2})$ and $Yb^{3+}(^2F_{7/2})$ ions results in excited $Er^{3+}(^4I_{11/2})$ and $Yb^{3+}(^2F_{5/2})$ ions. The energy difference of ~1100 cm^{-1} can easily be taken from 3-4 phonons of the LaF_3 phase or 1-2 phonons of the lanthanum silicate phase. The $Yb^{3+}(^2F_{5/2})$ ion then transfers its energy to a ground-state Er^{3+} ion to produce another $Er^{3+}(^4I_{11/2})$ ion. The net effect of the process illustrated in Figure 4.11b is, therefore, $Er^{3+}(^2H_{11/2})+Er^{3+}(^4I_{15/2})\rightarrow 2Er^{3+}(^4I_{11/2})$. (Note, then, that the role of Yb^{3+} at this stage in the mechanism is to facilitate Er^{3+}-Er^{3+} cross relaxation.) It is this step that provides the multiplier effect to produce $Er^{3+}(^4I_{11/2})$, which is the reservoir level for up-conversion. Feedback, or 'looping,' occurs because energy transfer from $Yb(^2F_{5/2})$ to $Er^{3+}(^4I_{11/2})$ ion regenerates $Er^{3+}(^2H_{11/2})$, which resets the loop. One has to bear in mind that the Yb^{3+} ion which is involved in the cross relaxation in Figure 4.11b is (most likely) different from the Yb^{3+} ion involved in the Figure 4.11a, because of the high concentration of Yb^{3+}. This high Yb^{3+} concentration also facilitates energy migration between them. As a result, the high Yb^{3+} concentration makes the cross relaxation between two Er^{3+} ions relatively efficient when compared to the other energy transfer steps in Figure 4.11a and 4.11c.

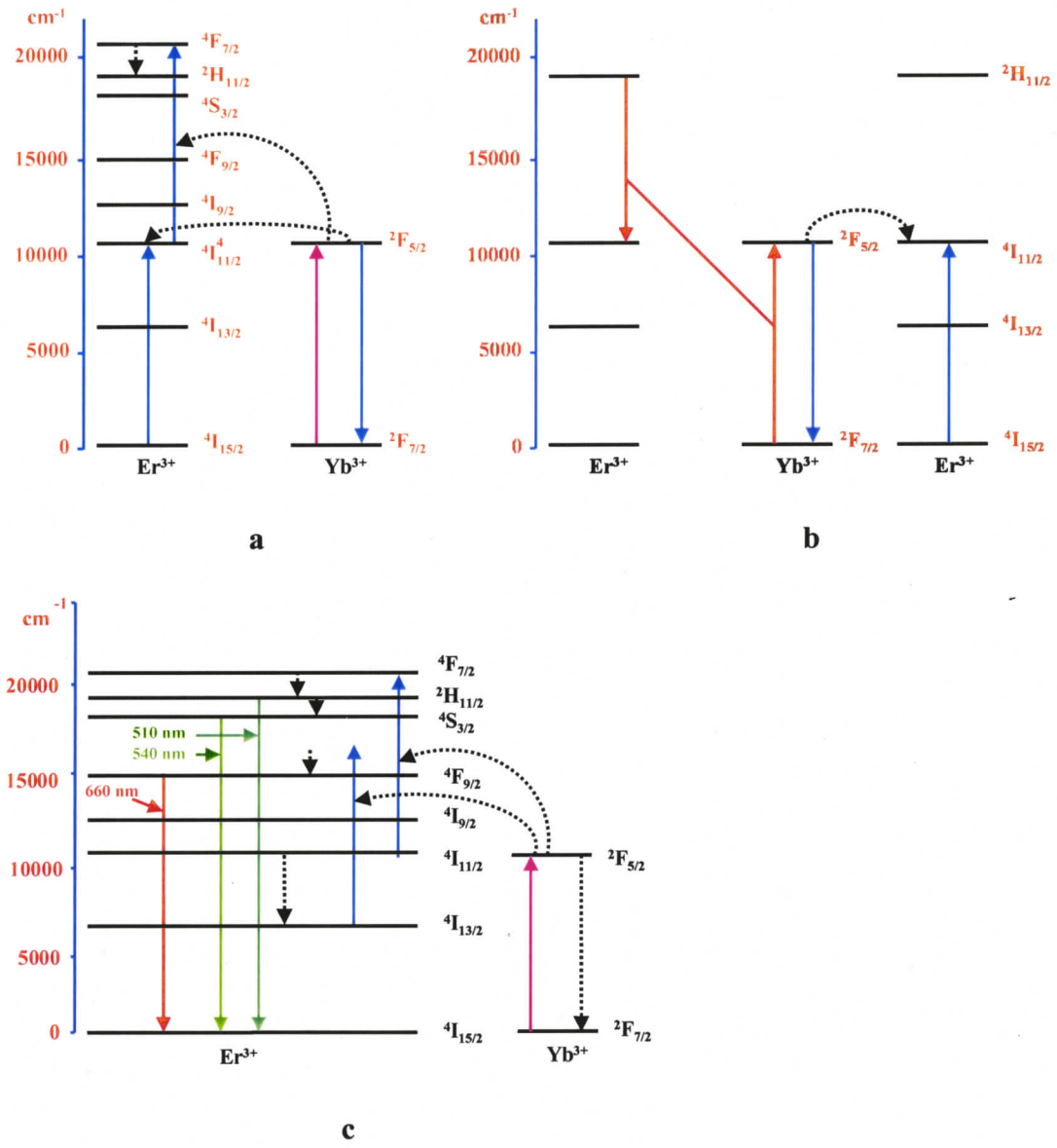

Figure 4.11. Up-conversion mechanism through the *hetero*-LEET process. a) Initial stage involving ETU. b) start of feedback loop via Yb^{3+}-assisted Er^{3+}-Er^{3+} cross relaxation (some energy levels have been omitted for clarity), c) generation of red and green emission from Er^{3+}.

Figure 4.11c shows the generation of up-conversion emission within this loop. Green emission is generated by multiphonon relaxation from $Er^{3+}(^4F_{7/2})$ to $Er^{3+}(^2H_{11/2} + {}^4S_{3/2})$ level, followed by $Er^{3+}(^2H_{11/2} + {}^4S_{3/2}) \rightarrow Er^{3+}(^4I_{15/2})$ emission. For red emission,

excited Er^{3+} ions in the $^4I_{11/2}$ reservoir level relax to $^4I_{13/2}$ level through multiphonon relaxation. Immediately following this process, the excited $Er^{3+}(^4I_{13/2})$ ion is excited further to the $^4F_{9/2}$ level through energy-transfer from excited Yb^{3+} ions.

In the absence of looping, both red and green up-conversion should be two-photon processes. This is supported by the observed power dependence (slope ~ 2) of up-conversion intensity at low laser-power densities (<4.5 W/cm^2), at which feedback amplification is unimportant. Additionally, a very weak blue emission is generated from $Er^{3+}(^2G_{9/2})$ level to ground state, which is populated through the following process: the excited Er^{3+} ion in $^2H_{11/2}/^4S_{3/2}$ level is further excited to $^2G_{7/2}$ level through a energy transfer from $Yb^{3+}(^2F_{5/2})$ ion. Subsequently, the excited Er^{3+} ion relaxes to $^2G_{9/2}$ level through multiphonon relaxation after which the blue emission at 410 nm takes place.

The red emission from $^4F_{9/2}$ level could in principle occur through another possible mechanism (Figure 4.12):[12,18] the excited Er^{3+} ion in $^4S_{3/2}$ level relax to $^4F_{9/2}$ level through multiphonon relaxation. However, this pathway may not occur in the current sample because the intensity of green to red ratio increases with the laser power and the shape of temporal evolution graph of red emission is different from the temporal evolution graph of green emission. If this pathway occurs, the red emission should have the same time characteristics as the green emission.

In order to investigate the importance of Yb^{3+} in the *hetero*-LEET mechanism, two control samples were prepared. Figure 4.13 shows the power dependence graphs of control silica thin films individually made with $La_{0.45}Lu_{0.50}Er_{0.05}F_3$ (no Yb^{3+}, Figure 4.13a) and $La_{0.90}Yb_{0.05}Er_{0.05}F_3$ nanoparticles (low Yb^{3+} concentration, Figure 4.13b), giving a slope of ~2 over most of the power range. This clearly demonstrates that these

are normal two-photon processes. Interestingly, however, they show the appearance of threshold at higher laser powers, which suggests the possibility of a looping mechanism involving direct Er^{3+}-Er^{3+} cross relaxation. Nevertheless, direct Er^{3+}-Er^{3+} cross relaxation is unlikely to dominate in the presence of high Yb^{3+} concentration. This is supported by the power dependence for the silica thin film made with $La_{0.90}Yb_{0.05}Er_{0.05}F_3$ nanoparticles (Figure 4.13a), which shows the appearance of feed back point at lower laser power (~94 W/cm^2) relative to thin films (Figure 4.13b) made with $La_{0.45}Lu_{0.50}Er_{0.05}F_3$ nanoparticles (~125 W/cm^2). It is noted, however, that, in this proposed mechanism, changing the Yb^{3+} concentration simultaneously affects the efficiency of ETU (Figure 4.11a) and the feedback loop (Figure 4.11b), both of which influence the onset of feed back point.

One has to bear in mind that the current sample has a non-stoichiometric lanthanum silicate phase ($La_{9.31}Si_{6.24}O_{26}$) along with the expected LaF_3 phase. It is, however, important to know in which phase the *hetero*-LEET mechanism occurs. Two control samples have been prepared to investigate this. Citrate-stabilised $La_{0.45}Yb_{0.50}Er_{0.05}F_3$ and $La_{0.45}Lu_{0.50}Er_{0.05}F_3$ nanoparticles have been heated to burn of the citrate and XRD data on these materials confirm the presence of pure LaF_3 phase. The power dependence graph of the heated $La_{0.45}Yb_{0.50}Er_{0.05}F_3$ control material (Figure 4.13c) is also S-shaped, similar to the power dependence graph of the silica thin film made with $La_{0.45}Yb_{0.50}Er_{0.05}F_3$ nanoparticles. It demonstrates that the slopes of both the red and green emission increase rapidly with increasing excitation power, giving a maximum slope of ~6. Power dependence graph of the heated $La_{0.45}Lu_{0.50}Er_{0.05}F_3$ control material gives the slope of ~2 (Figure 4.13d). These slopes strongly indicate that the *hetero*-LEET mechanism happens in LaF_3 phase, and also that the apparent many-photon power

dependence is not an artifact due to the presence of impurities or multiple phases. We note that the maximum slope in the $La_{0.45}Yb_{0.50}Er_{0.05}F_3$ control sample is lower than the silica thin film made with $La_{0.45}Yb_{0.50}Er_{0.05}F_3$ nanoparticles. This may be due to the involvement of the silicate phase in the *hetero*-LEET mechanism, but it could also be simply due to the interaction of the Ln^{3+} ions near the surface of the nanoparticles with the silica matrix. Because of the high surface-to-volume ratio of these nanoparticles, the interaction of the nanoparticles with the host matrix has a significant effect on their luminescence properties. Hence, the LaF_3 phase plays a major role in the hetero-LEET, but involvement of the silicate phase cannot be ruled out. Further studies to resolve this are in progress.

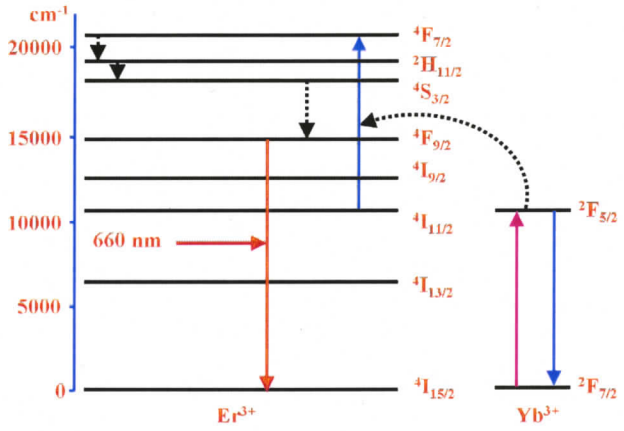

Figure 4.12 Generation of red emission from Er^{3+} through another possible up-conversion mechanism involving the *hetero*-LEET process.

Figure 4.14 shows the up-conversion emission spectra of silica thin film made with nanoparticles with different Yb^{3+} concentrations under 980 nm CW laser excitation. The green to red emission intensity decreases with increase in Yb^{3+} concentration. The distance between Yb^{3+} and Er^{3+} decreases in the lattice with the increase in Yb^{3+}

concentration which increases the cross relaxation between $Er^{3+}(^4F_{7/2})$ and $Yb^{3+}(^2F_{7/2})$ ions. This cross relaxation decreases the population of the $^2H_{11/2}$ & $^4S_{3/2}$ levels and thus decreases the green emission. This further substantiates the importance of Yb^{3+} concentration in the *hetero*-LEET mechanism.

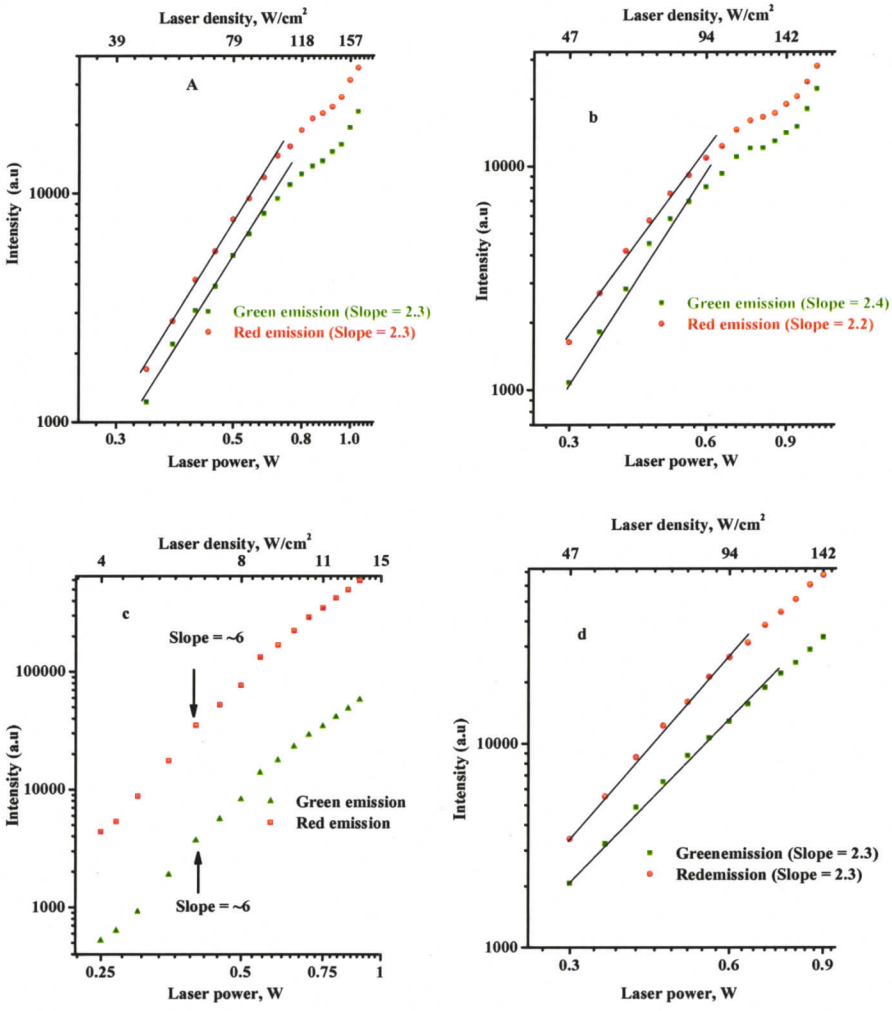

Figure 4.13. Dependence of the up-conversion emission intensity on the excitation power in a) silica thin films prepared at 800 °C made with $La_{0.45}Lu_{0.50}Er_{0.05}F_3$ nanoparticles, b) silica thin films prepared at 800 °C made with $La_{0.90}Yb_{0.05}Er_{0.05}F_3$ nanoparticles, c) heated $La_{0.45}Yb_{0.50}Er_{0.05}F_3$ nanoparticles d) heated $La_{0.45}Lu_{0.50}Er_{0.05}F_3$ nanoparticles under 980 nm CW laser excitation. (end of fiber is 3 mm away from the sample)

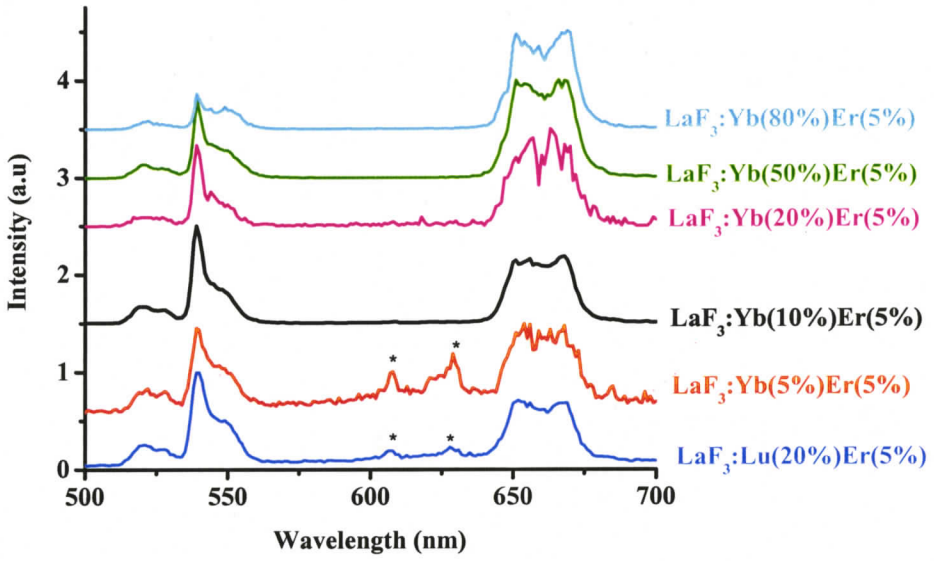

Figure 4.14. Up-conversion emission spectrum of silica thin film prepared at 800 °C made with nanoparticles having different Yb^{3+} concentration under 980 nm 400 mW CW laser excitation (* - artefact).

Figure 4.15 demonstrates the up-conversion emission spectra of silica thin film made with nanoparticles with different Er^{3+} concentration under 980 nm CW laser excitation. The green to red emission intensity also decreases with increase in Er^{3+} concentration, which is attributed to Er^{3+}-Er^{3+} cross relaxation: $Er^{3+}(^4F_{7/2})+Er^{3+}(^4I_{15/2})\rightarrow 2\ Er^{3+}(^4I_{11/2})$. The increase in the red emission intensity may be due the efficient multiphonon relaxation from $^4I_{11/2}$ to $^4I_{13/2}$ level.

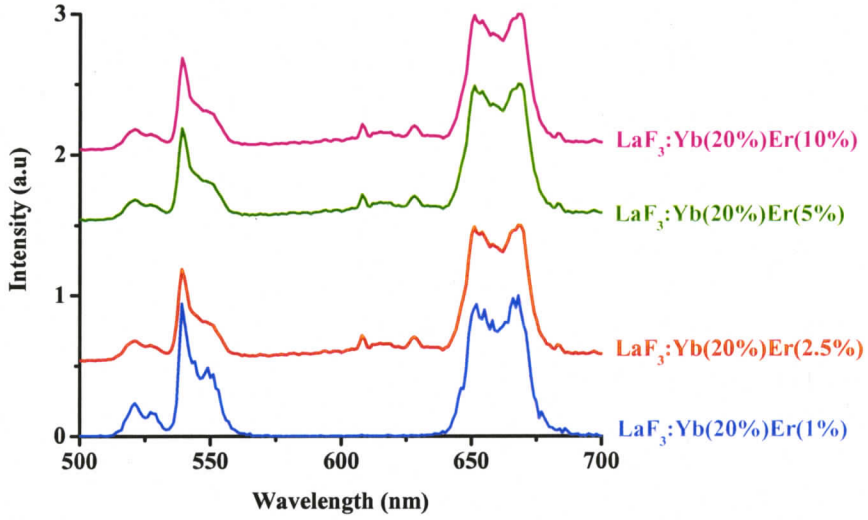

Figure 4.15. Up-conversion emission spectrum of silica thin film prepared at 800 °C made with nanoparticles having different Er^{3+} concentration under 980 nm 400 mW CW laser excitation.

Figure 4.16 demonstrates the up-conversion emission spectra at different temperatures of silica thin film prepared at 800 °C made with $La_{0.45}Yb_{0.50}Er_{0.05}F_3$ nanoparticles under 980 nm 400 mW CW laser excitation. At liquid nitrogen temperature of 77 K, the green emission from $^2H_{11/2}$ to $^4I_{15/2}$ transition was not observed, whereas the other green emission from $^4S_{3/2}$ level and red emission from $^4F_{9/2}$ level were clearly observed. When the temperature was increased to 273 K and 293 K the green band, called hot band ($^2H_{11/2}$ to $^4I_{15/2}$ transition) appeared. This is attributed to the heating effect of the $^2H_{11/2}$. Wang *et al.* have reported this heating effect in erbium doped ZnO nanocrystals.[11] At liquid nitrogen temperature the red to green emission ratio is larger when compared to higher temperatures. This demonstrates that the energy transfer from $Yb^{3+}(^2F_{5/2})$ to $Er^{3+}(^4I_{13/2})$ level could occur bypassing the $^4I_{11/2}$ level or the multiphonon relaxation from

$^4I_{11/2}$ to $^4I_{13/2}$ level is still efficient at lower temperatures (Figure 4.17). One has to bear in mind that Yb^{3+} ion has higher absorption cross section in the NIR region. (940 -1050 nm). Due to crystal field splitting of Yb^{3+} at lower temperature (78 K) the energy transfer could happen from the lowest level (1050 nm) to $^4I_{13/2}$ level rather than to $^4I_{11/2}$ level (up-hill process). Subsequently, it is further excited to $^4F_{9/2}$ level.

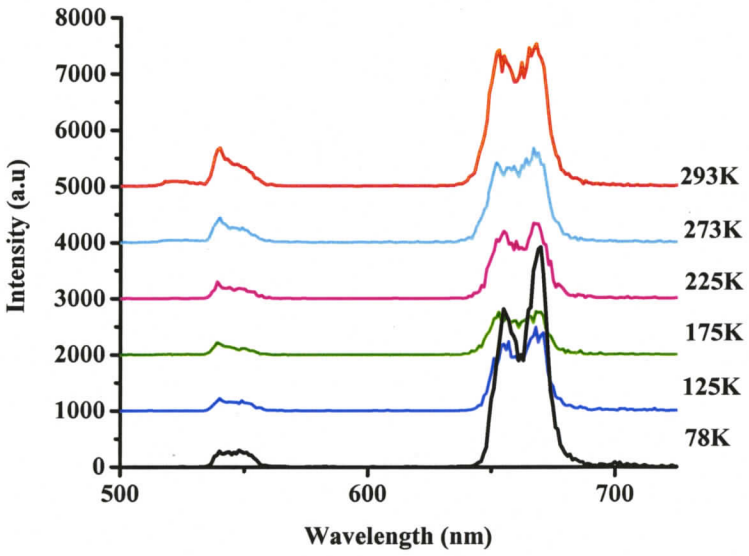

Figure 4.16. Up-conversion emission spectra from silica thin film prepared at 800 °C made with $La_{0.45}Yb_{0.50}Er_{0.05}F_3$ nanoparticles measured at different temperatures under 400 mW 980 nm CW laser excitation.

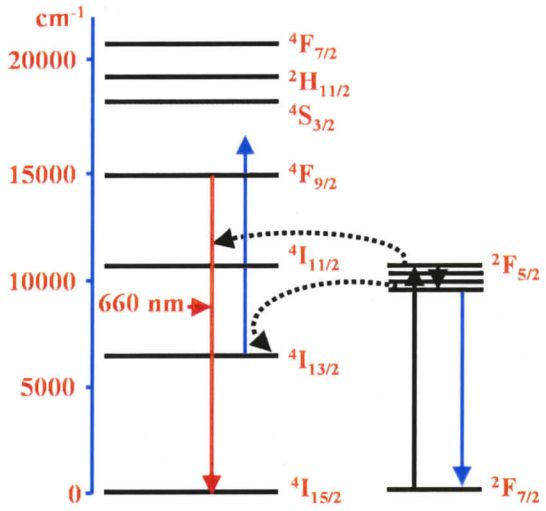

Figure 4.17. Mechanism of up-conversion of Yb^{3+}/Er^{3+} at 78K.

4.3. Conclusion

In conclusion, a new, potentially efficient up-conversion mechanism called *hetero*-LEET is reported in this chapter for the generation of green and red emission from silica thin films made with $La_{0.45}Yb_{0.50}Er_{0.05}F_3$ nanoparticles. This mechanism combines the advantages of resonant ground-state absorption and ETU with a cross-relaxation feedback loop that results in an avalanche-like power dependence.

4.4 Experimental Section

Preparation of citrate-stabilised $La_{0.45}Yb_{0.50}Er_{0.05}F_3$ nanoparticles and silica sol-gel thin layer are described in the chapter 3. Optical characterisations were done by using the same set-up reported in the chapter 3. Temporal evolution analysis were done with an optical chopper operated at 2.7 Hz by chopping the 980 nm CW laser light and the signals

were collected by using an oscilloscope. Up-conversion emission spectra at lower temperatures were measured by using a variable temperature liquid nitrogen cooled cryostat (Optistat DN, Oxford instruments) in which the temperature was controlled by an ITC-601 temperature controller. The up-conversion emission spectra were measured at 2 nm resolution.

For consistency, all the thin-film materials were scratched from the quartz plate, 15 mg of which was mixed with 35 mg of KBr to make uniform pellets. The emission intensities over the whole area of the pellet were the same within experimental error. The power density was calculated based on the divergence of laser light (10°) and distance between the sample and laser. Intensities in the power dependence graphs were calculated based on the integrated area under the peaks of emission spectrum under respective power densities. Control samples of citrate-stabilised $La_{0.45}Lu_{0.50}Er_{0.05}F_3$ and $La_{0.90}Yb_{0.05}Er_{0.05}F_3$ nanoparticles were heated at 500°C to burn off the citrate. The absence of the C=O stretch in the IR spectrum of these heated materials confirms that all the citrate had been burned off. XRD of these materials confirmed the presence of pure LaF_3 phase.

References

(1) Lim, S. F.; Riehn, R.; Ryu, W. S.; Khanarian, N.; Tung, C. K.; Tank, D.; Austin, R. H. *Nano Lett.* **2006**, *6*, 169.

(2) Mehta, A.; Thundat, T.; Barnes, M. D.; Chhabra, V.; Bhargava, R.; Bartko, A. P.; Dickson, R. M. *Appl. Optics* **2003**, *42*, 2132.

(3) Zhang, H. X.; Kam, C. H.; Zhou, Y.; Han, X. Q.; Buddhudu, S.; Xiang, Q.; Lam, Y. L.; Chan, Y. C. *Appl. Phys. Lett.* **2000**, *77*, 609.

(4) Soo, Y. L.; Huang, S. W.; Ming, Z. H.; Kao, Y. H.; Smith, G. C.; Goldburt, E.; Hodel, R.; Kulkarni, B.; Veliadis, J. V. D.; Bhargava, R. N. *J. Appl. Phys.* **1998**, *83*, 5404.

(5) Patra, A.; Friend, C. S.; Kapoor, R.; Prasad, P. N. *J. Phys. Chem. B* **2002**, *106*, 1909.

(6) Sivakumar, S.; Diamente, P. R.; van Veggel, F. C. J. M. *Chem. Eur. J.* **2006**, *12*, 5884.

(7) Heer, S.; Lehmann, O.; Haase, M.; Güdel, H. U. *Angew. Chem. Int. Edn.* **2003**, *42*, 3179.

(8) Patra, A.; Friend, C. S.; Kapoor, R.; Prasad, P. N. *Appl. Phys. Lett.* **2003**, *83*, 284.

(9) Vetrone, F.; Boyer, J. C.; Capobianco, J. A.; Speghini, A.; Bettinelli, M. *J. Phys. Chem. B* **2003**, *107*, 1107.

(10) Vetrone, F.; Boyer, J. C.; Capobianco, J. A.; Speghini, A.; Bettinelli, M. *Chem. Mater.* **2003**, *15*, 2737.

(11) Wang, X.; Kong, X. G.; Shan, G. Y.; Yu, Y.; Sun, Y. J.; Feng, L. Y.; Chao, K. F.; Lu, S. Z.; Li, Y. J. *J. Phys. Chem. B* **2004**, *108*, 18408.

(12) Heer, S.; Kompe, K.; Güdel, H. U.; Haase, M. *Adv. Mater.* **2004**, *16*, 2102.

(13) Stouwdam, J. W.; van Veggel, F. C. J. M. *Nano Lett.* **2002**, *2*, 733.

(14) Stouwdam, J. W.; van Veggel, F. C. J. M. *Langmuir* **2004**, *20*, 11763.

(15) Sudarsan, V.; Sivakumar, S.; van Veggel, F. C. J. M.; Raudsepp, M. *Chem. Mater.* **2005**, *17*, 4736.

(16) Suyver, J. F.; Aebischer, A.; Biner, D.; Gerner, P.; Grimm, J.; Heer, S.; Kramer, K. W.; Reinhard, C.; Güdel, H. U. *Opt. Mater.* **2005**, *27*, 1111.

(17) Scheps, R. *Prog. Quant. Electron.* **1996**, *20*, 271.

(18) Wright, J. C. *Top. Appl. Phys.* **1976**, *15*, 239.

(19) Joubert, M. F. *Opt. Mater.* **1999**, *11*, 181.

(20) Lupei, V. *Spectrochim. Acta, Part A* **1998**, *54*, 1615.

(21) Lahoz, F.; Martin, I. R.; Briones, A. *J. Appl. Phys.* **2004**, *95*, 2957.

(22) Goldner, P.; Pelle, F. *Opt. Mater.* **1996**, *5*, 239.

(23) Auzel, F.; Chen, Y. H. *J. Lumin.* **1995**, *65*, 45.

(24) Auzel, F.; Chen, Y. H.; Meichenin, D. *J. Lumin.* **1994**, *60-1*, 692.

(25) Chen, Y. H.; Auzel, F. *Electron. Lett.* **1994**, *30*, 1602.

(26) Bell, M. J. V.; de Sousa, D. F.; Nunes, L. A. O. *J. Appl. Phys.* **2000**, *87*, 8264.

(27) Rakov, N.; deAraujo, C. B.; Messaddeq, Y.; Aegerter, M. A. *Appl. Phys. Lett.* **1997**, *70*, 3084.

(28) Sosa, R.; Foldvari, I.; Watterich, A.; Munoz, A.; Maillard, R. S.; Kugel, G. *J. Lumin.* **2005**, *111*, 25.

(29) Sivakumar, S.; van Veggel, F. C. J. M.; Raudsepp, M. *J. Am. Chem. Soc.* **2005**, *127*, 12464.

CHAPTER 5

Sensitized emission from lanthanide-doped nanoparticles embedded in a semiconductor matrix*©

---

* The major part of the work in this chapter has been submitted:

Sri Sivakumar, Frank C.J.M. van Veggel, and Mati Raudsepp, submitted.

5.1. Introduction

Bright white light has been generated through up-conversion of a single NIR source from SiO_2 and ZrO_2 sol-gel thin films made with lanthanide-doped nanoparticles, as was discussed in the chapter 3. In these sol-gel thin films, the host nanoparticle/sol-gel thin film material is not involved in the excitation of lanthanide ions, but optically excited through energy transfer from Yb^{3+} ions. The direct excitation of the lanthanide ions is a relatively inefficient process, due to the forbidden character of the intra-4*f* transitions. Eventhough the Yb^{3+} ion has a higher extinction coefficient than the other lanthanide ions, the extinction coefficient of Yb^{3+} ion is still low (10 $M^{-1}cm^{-1}$).[1] An alternative way to generate bright luminescence from lanthanide ions is through energy transfer from the host material to lanthanide ions which could overcome the drawback of the low absorption cross-sections of the lanthanide ions. This can be achieved by doping the lanthanide ions into a semiconductor matrix which can facilitate the efficient generation of luminescence from lanthanide ions by electrical/optical excitation. This principle has already been shown with bulk semiconductor materials.[2] These materials could have potential applications in light-emitting diodes, displays, lasers, and optical amplifiers.

Many research groups[3-6] including our group[7] have investigated the possibility of exciting (optical excitation) the lanthanide ions in highly dispersible $LnVO_4$ (Ln = La, Gd, and Y) nanoparticles by exciting VO_4 group in the UV region followed by energy transfer to lanthanide ions. Eventhough these nanoparticles show very good quantum yield they cannot be excited by electricity because they are insulators. Generation of luminescence from lanthanide complexes through electrical excitation have been investigated by many research groups including our group.[8-12] The major problem in these

devices is that the luminescence of lanthanide ions, especially in NIR region, is heavily quenched by organic ligands. These issues could potentially be addressed by incorporating the lanthanide ions into semiconductor matrix and it could also offer the possibility of electroluminescence. Several research groups including our group have investigated the incorporation of lanthanide ions into semiconductor matrices (thin films[13-20] and nanoparticles[21-26]). Many researchers have reported on the investigation of lanthanide-doped CdS and ZnS nanoparticles that are dispersible in organic solvents.[27-33] However, to date there is no convincing proof available for energy transfer from II-VI semiconductor nanoparticle to lanthanide ion. Direct evidence of energy transfer should be found from the excitation spectrum of lanthanide ion, in which the spectrum should have the absorption lines of lanthanide ions as well as absorption of the semiconductor matrix. In addition, Bol *et al.*[34] have demonstrated that the lanthanide ions are not incorporated in the II-VI semiconductor nanoparticle prepared by commonly applied precipitation methods and microemulsion techniques. They have shown that the excitation spectrum of lanthanide ion doesn't have absorption bands of the semiconductor. They have concluded that lanthanide ions are probably adsorbed on the surface of semiconductor nanoparticles. They have suggested an alternative method to dope the lanthanide ions into semiconductor matrix by doing the synthesis at high temperatures. However, synthesise at high temperatures can lead to substantial increase in the particle size. Raola and Strouse have investigated on the doping of Eu^{3+} ion in CdSe nanoparticles, but no luminescence studies were done.[35] They introduced the europium in the form of Eu^{2+} and found that the Eu^{3+} was present after work-up. Petoud *et al.* claim that the Tb^{3+} ions were incorporated into CdSe nanoparticles prepared by colloidal

synthesis route. However, the excitation spectrum of Tb^{3+} ion probably has the absorption 4f-5d transitions of Tb^{3+} ion, not the absorption of CdSe. The possible reasons for the difficulties in the incorporation of lanthanide ions into semiconductor matrices are (either one of combination of): 1) large mismatch in the size of host cation (Zn^{2+} = 0.74 Å and Cd^{2+} = 1.01 Å) and lanthanide ions (Eu^{3+} = 1.07 Å and Tb^{3+} = 1.04 Å), 2) the charge mismatch, and 3) low affinity of lanthanide ions towards sulphur and selenium.[21] Nevertheless, the principle of energy transfer from semiconductor matrix to lanthanide ions has been proved in bulk ZnS upon excitation of ZnS matrix.[2] The principle has also been shown in low-phonon energy glasses incorporated with semiconductor ($CdS/SnO_2/Si$) nanocrystals and Ln^{3+} (Eu^{3+}/Er^{3+}) ions in which the energy transfer occurs from CdS to Eu^{3+} ions, SnO_2 to Eu^{3+} ions, and silicon nanocrystals to Er^{3+} ions.[24,25] In these glasses the lanthanide ions are near the surface of semiconductor nanoparticles, not doped into the semiconductor matrix.

Our group has investigated the TiO_2 nanoparticles doped with lanthanide ions and have shown proof of energy transfer from TiO_2 semiconductor nanoparticle matrix to lanthanide ions,[21] albeit, the low quantum yield (0.03%) of sensitized Eu^{3+} emission is attributed to the quenching of Eu^{3+} ion by residual OH groups present in the nanoparticles. So clearly, there is a need to investigate general methods to incorporate lanthanide ions into a semiconductor matrix. In this chapter, two alternative approaches to incorporate lanthanide ion into semiconductor matrix are reported. They are, 1) incorporation of lanthanide-doped nanoparticles into semiconductor sol-gel thin films (In_2O_3, ZrO_2, and HfO_2), 2) synthesis of semiconductor (In_2O_3)-coated lanthanide-doped nanoparticles.

In_2O_3 is a n-type semiconductor with a wide band gap of 3.6 eV and is widely used in optoelectronics, solar cells, gas sensors, and flat panel displays. The bandgap of bulk $La_2Zr_2O_7$ and $La_2Hf_2O_7$ are 3.9 and 3.1 eV, respectively.[36] ZrO_2 and HfO_2 are having bandgaps of 4.0 and 4.1 eV, respectively.[37]Despite the fact that the bandgap of ZrO_2 and HfO_2 are high, a few reports have proved that there is energy transfer from ZrO_2 and HfO_2 matrix to lanthanide ions (see below). To date, very few reports are available on the direct incorporation of lanthanide ions into semiconductor sol-gel matrixes. Podhorodecki *et al.* have demonstrated the incorporation of Er^{3+} ion into In_2O_3 sol-gel thin films. However, there is no direct proof of energy transfer from semiconductor matrix to lanthanide ions available. Rosa *et al.*[38,39] have demonstrated the direct proof of energy transfer from ZrO_2 nanopowder to Sm^{3+} ion prepared by sol-gel method. Rodriguez *et al.*[40,41] have shown the energy transfer from SnO_2 nanoparticle to Eu^{3+} ion in silica sol-gel glasses. Sasaki *et al.*[42] have demonstrated the energy transfer from TiO_2 nanosheets to Eu^{3+} and Tb^{3+} ion. To my knowledge, there are no reports available on the incorporation of lanthanide-doped nanoparticles into semiconductor sol-gel thin films and highly dispersible semiconductor-coated lanthanide-doped nanoparticles. These approaches take advantage of an investigation of our group[43-46] from which one can predict that 40% of lanthanide ions are on the surface of LaF_3 nanoparticles and thus developing a semiconductor shell over the nanoparticles could facilitate the energy transfer from semiconductor matrix to lanthanide ion. Moreover, sol-gel technique is one of the promising methods to make thin film because of their advantages such as its simplicity and its ability to control the purity and homogeneity of the final material on a molecular level. The formation of $La_2Zr_2O_7$ phase in the ZrO_2 sol-gel thin film made with

LaF_3 nanoparticles has been already discussed in chapter 3. Similarly, $La_2Hf_2O_7$ is formed in the HfO_2 sol-gel made with LaF_3 nanoparticles (see results and discussion section). In this chapter, In_2O_3, ZrO_2, and HfO_2 sol-gel thin films made with lanthanide-doped LaF_3 nanoparticle and highly dispersible indium oxide-coated lanthanide-doped LaF_3 nanoparticle are reported. Energy transfer from semiconductor matrix to lanthanide ion is also demonstrated in the chapter.

Scheme 5.1 demonstrates the principle of energy transfer from semiconductor matrix to lanthanide ions by optical/electrical excitation. Lanthanide-doped nanoparticles are embedded in the semiconductor sol-gel thin layer and the lanthanide ions are excited through energy transfer from semiconductor matrix which is excited by optical/electrical excitation.

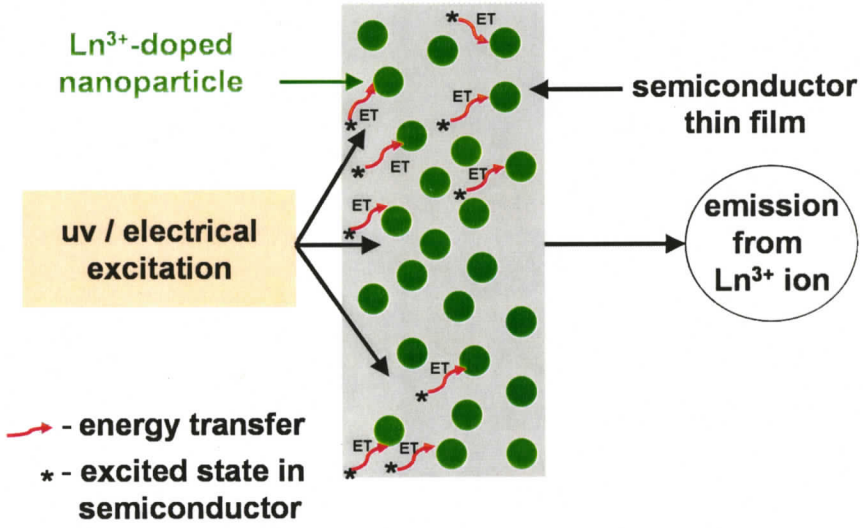

Scheme 5.1. Semiconductor sol-gel thin film made with LaF_3:Ln^{3+} nanoparticles

5.2 Results and discussion

5.2.1. In_2O_3 sol-gel thin film made with LaF_3 nanoparticle

Formation and characterisation of citrate-stabilised LaF_3:Ln^{3+}(5%) nanoparticles has been discussed in chapter 3. The In_2O_3 sol-gel made with nanoparticles was prepared by acid hydrolysis and the sol was spin-coated on a quartz plate and heated at 800 °C for 12 h. A detailed method of preparation of sol-gel thin films made with nanoparticles is given in the experimental section.

XRD studies carried out on In_2O_3 sol-gel thin layer made with LaF_3:Er nanoparticles showed the presence of In_2O_3 along with LaOF (Figure 5.1). It can be concluded that the LaF_3 nanoparticles had reacted with OH groups present in the In_2O_3 sol-gel at high temperature (~800 °C) to form the LaOF phase. However, there is no formation of $LaInO_3$ phase because generally the formation of the $LaInO_3$ phase happens at very high temperature (~1400 °C). There is also no evidence for the presence of LaF_3 and La_2O_3 phase in the sol-gel thin layer. The phase formation is different from the ZrO_2 and SiO_2 sol-gel thin layers where there is no formation of LaOF phase. The chemical equation for the formation of LaOF from LaF_3 is given below.

$$2In(OH)_3 + 2LaF_3 \rightarrow 2LaOF + HF + In_2O_3 + H_2O$$

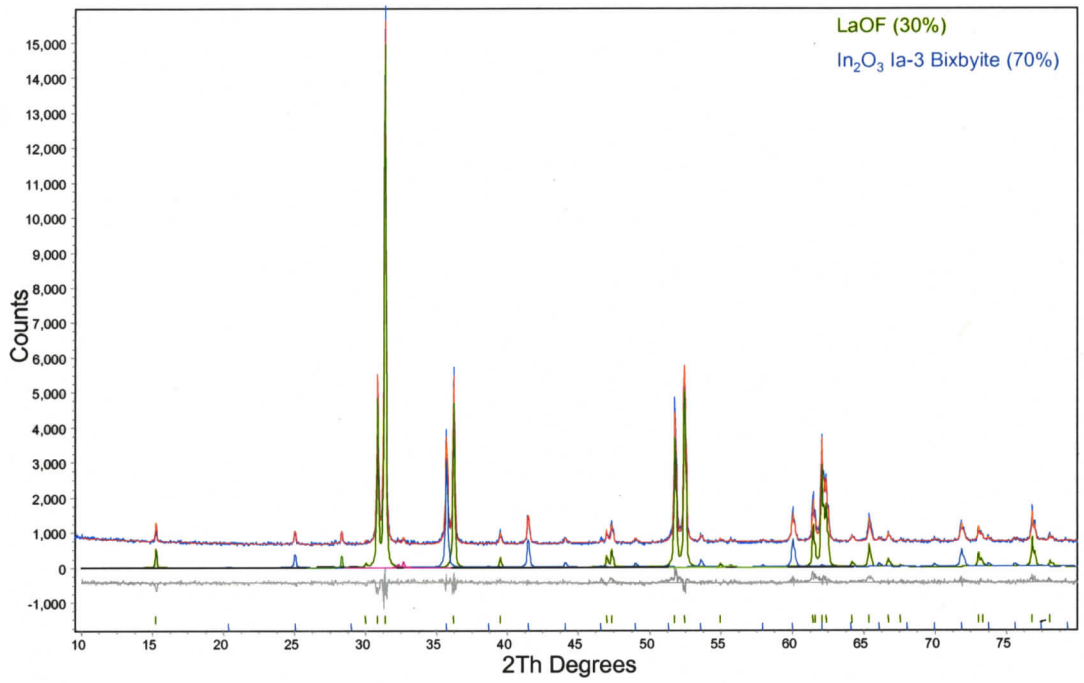

Figure 5.1. Experimental and calculated XRD pattern (Rietveld refinement plot) of a In_2O_3 film prepared at 800 °C made LaF_3:Er nanoparticles. Green lines: LaOF phase, Blue lines: In_2O_3 Ia-3 Bixbyite phase, Grey lines: residual, Red line: Sample

In_2O_3 sol-gel thin film made with $LaF_3:Er^{3+}$ (5%) nanoparticles were chosen as a model thin film to prove the principle of energy transfer from semiconductor matrix to lanthanide ion. Figure 5.2a shows the emission spectrum of In_2O_3 sol-gel thin film made with LaF_3:Er nanoparticles under 385 nm excitation where there are no absorption lines for Er^{3+} ion. The emission band at 1530 nm is assigned to the $^4I_{13/2}$ to $^4I_{15/2}$ transition of Er^{3+} ion. Figure 5.2b demonstrates the excitation spectrum of Er^{3+} ion by collecting the emission at 1530 nm and shows a broad band between 250-450 nm and some sharp peaks at 488 nm and 525 nm. The shape of the broad band in excitation spectrum is different from the absorption spectrum (Figure 5.2c) of the In_2O_3 sol-gel thin film made with LaF_3:Er nanoparticles because, the excitation spectrum shows only the excitation levels of

In_2O_3 which involves in the energy transfer process. On the other hand, the absorption spectrum shows all the absorption levels of In_2O_3. The excitation spectrum clearly proves that there is energy transfer from In_2O_3 matrix to Er^{3+} ion. The sharp peaks at 488 nm and 525 nm corresponds to absorption peaks of the $^4F_{7/2}$ and $^2H_{11/2}$ levels of Er^{3+} ion, respectively. The broad band between 300-460 nm could be due to oxygen vacancies in the semiconductor matrix (see below). The effective lifetime of the $^4I_{13/2}$ level of Er^{3+} ion is 7.8 ms with an estimated quantum yield of 50% based on the radiative lifetime of 16 ms.[47]

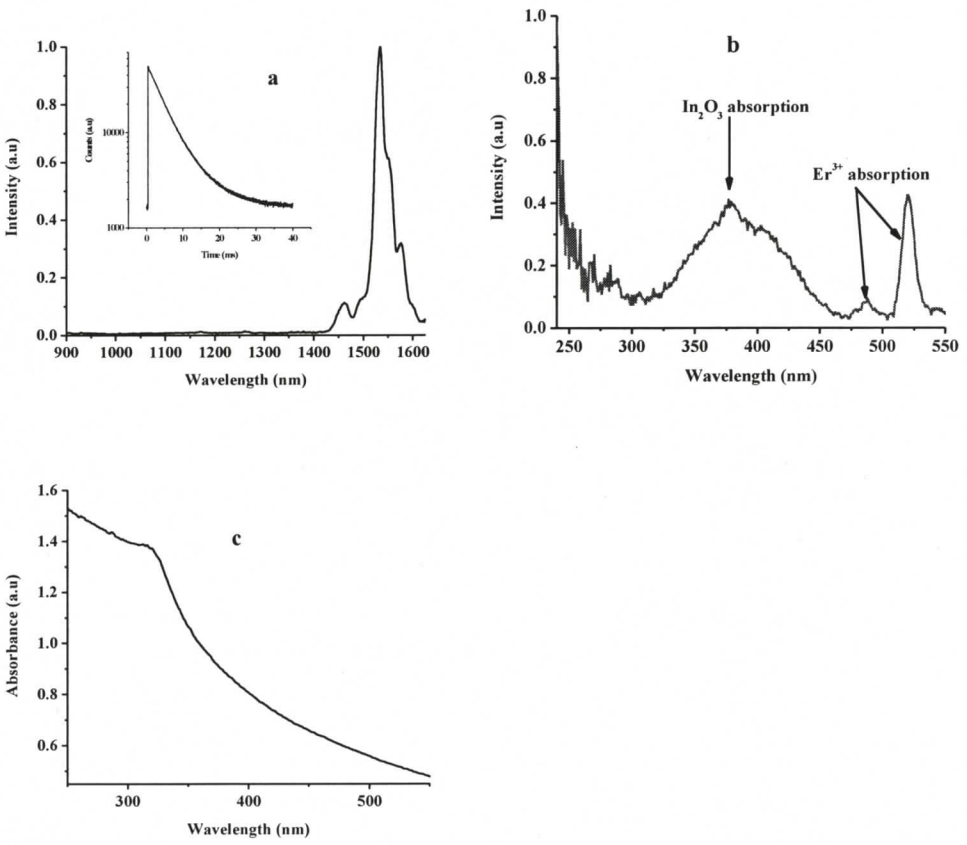

Figure 5.2. In_2O_3 sol-gel thin film made with LaF_3:Er nanoparticles a) emission spectrum under 385 nm excitation. Inset shows the decay curve of $^4I_{13/2}$ level of Er^{3+} ion b) excitation spectrum for emission collected at 1530 nm, c) absorption spectrum.

Similarly, In_2O_3 sol-gel thin layers were prepared with LaF_3:Nd, LaF_3:Tb, LaF_3:Eu nanoparticles. Figure 5.3a demonstrates the emission spectrum of In_2O_3 sol-gel thin layer made with LaF_3:Nd nanoparticles in which the emission bands at 870, 1070, and 1330 nm are from $^4F_{3/2}$ transitions to $^4I_{13/2}$, $^4I_{11/2}$, and $^4I_{9/2}$, respectively, with a effective luminescent lifetime of 220 μs (insert in Figure 5.3a). The excitation spectra (Figure 5.3b) shows the same broad band starting from 450-250 as for the In_2O_3 sol-gel thin film made with LaF_3:Er nanoparticles. It also shows the absorption lines of Nd^{3+} ions at 525 and 575 nm. This further substantiates the proof of energy transfer from In_2O_3 semiconductor matrix to Nd^{3+} ion.

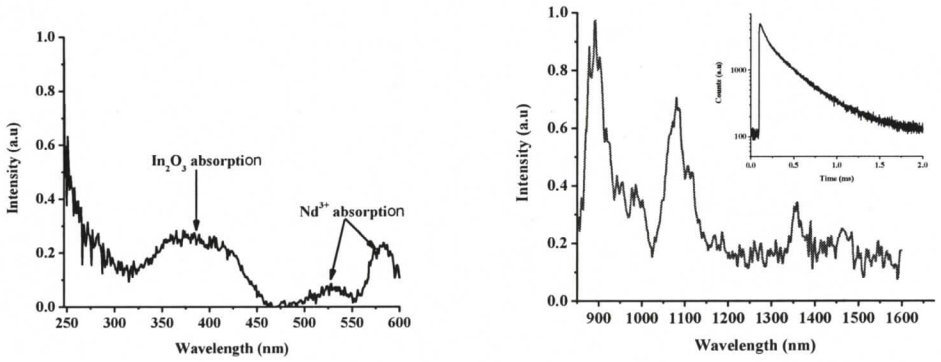

Figure 5.3. In_2O_3 sol-gel thin film made with LaF_3:Nd nanoparticles a) emission spectrum under 385 nm excitation. Inset shows the decay curve of $^4F_{3/2}$ level of Nd^{3+} ion b) excitation spectrum for emission collected at 1070 nm.

Figure 5.4a shows the emission spectrum of In_2O_3 sol-gel thin layer made with LaF_3:Eu nanoparticles where the major emission bands of Eu^{3+} ions at 590 and 612 nm are assigned to the $^5D_0$ to $^7F_1$ and $^5D_0$ to $^7F_2$ transitions. Figure 5.4b demonstrates the excitation spectrum of Eu^{3+} which again shows the absorption of In_2O_3. The absorption

lines of Eu^{3+} did not appear because their absorption lines (380-400 nm) were over shadowed by the In_2O_3 absorption lines.

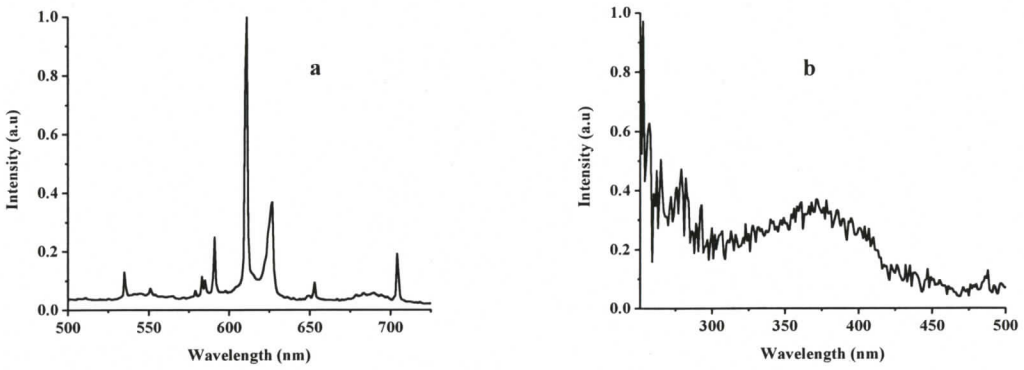

Figure 5.4. In_2O_3 sol-gel thin layer made with LaF_3:Eu nanoparticles a) emission spectrum under 350 nm excitation, b) excitation spectrum for emission collected at 612 nm.

Figure 5.5a demonstrates the emission spectrum of In_2O_3 sol-gel thin layer made with LaF_3:Tb nanoparticles in which the most intense peak at 545 nm corresponds to $^5D_4$ to $^7F_5$ transition, and the peaks at 490, 586, and 623 nm correspond to the $^5D_4$ to $^7F_6$, $^7F_4$, and $^7F_3$ transitions, respectively. Figure 5.5b shows the excitation spectrum of Tb^{3+} which is slightly different from previous ones. This may be due to the presence of different defects in the In_2O_3 matrix.

A control In_2O_3 thin film was prepared with LaF_3:Y (5%) nanoparticles because Y^{3+} does not posses any optical properties and mimics the doping of Ln^{3+} ion. Figure 5.6 demonstrates the emission of In_2O_3 sol-gel thin film made with LaF_3:Y nanoparticles where the blue emission band at 440 nm is assigned to emission from the In_2O_3 matrix due to the presence of oxygen vacancies.[48] These oxygen vacancies generally act as deep

defect donors in semiconductors and would induce the formation of new energy levels. The presence of broad band between 300-460 nm in all the excitation spectra is due to these oxygen vacancies. However, the blue emission is hardly present in the case of sol-gel thin film made with $LaF_3:Ln^{3+}$ nanoparticles because energy transfer occurs through these excited oxygen vacancies and it is apparently efficient (Figure 5.4).

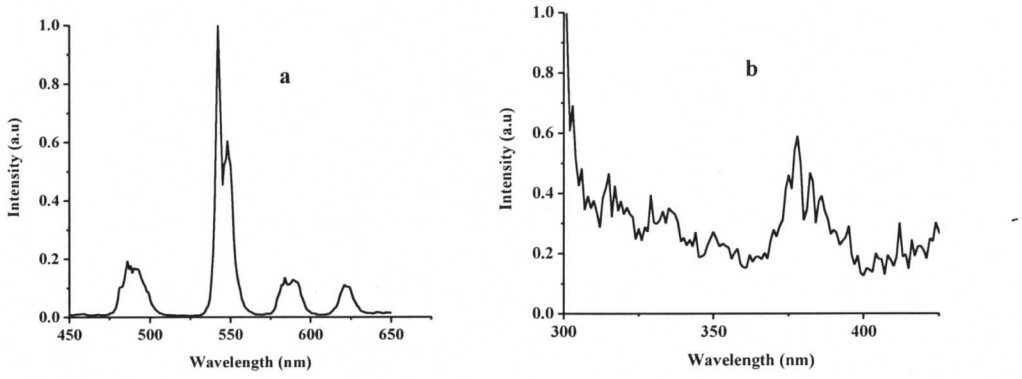

Figure 5.5. In_2O_3 sol-gel thin layer made with LaF_3:Tb nanoparticles a) emission spectrum under 335 nm excitation, b) excitation spectrum for emission collected at 545 nm.

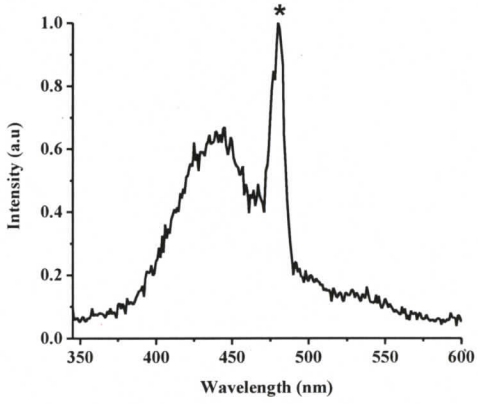

Figure 5.6. Emission spectrum In_2O_3 sol-gel thin layer made with LaF_3:Y nanoparticles under 325 nm excitation (* - artifact).

5.2.2. HfO_2 sol-gel thin film made with LaF_3 nanoparticle

HfO_2 sol-gel thin film made with $LaF_3:Ln^{3+}$ nanoparticles were prepared by the acid hydrolysis method. The sol was spin-coated on a quartz plate and heated at 800 °C. XRD studies carried out on HfO_2 sol-gel thin film made with LaF_3:Eu nanoparticles showed the presence of lanthanum hafnate ($La_2Hf_2O_7$) along with HfO_2 (Figure 5.7). It is concluded that the nanoparticles have reacted with OH groups present in HfO_2 sol-gel to form Ln^{3+} doped lanthanum hafnate. The chemical equation for the formation of lanthanum hafnate is given below.

$$2LaF_3 + 2Hf(OH)_4 \rightarrow La_2Hf_2O_7 + 6HF + H_2O$$

Figure 5.8a shows the emission spectrum of HfO_2 sol-gel thin layer made with LaF_3:Er nanoparticles in which emission bands at 1530 nm is assigned to Er^{3+} ion. Figure 5.8b demonstrates the excitation spectrum of Er^{3+} ion by collecting the 1530 nm emission and shows a broad absorption band from 250 to 350 nm and sharp peaks at 488 and 525 nm. The broad absorption band is assigned to $La_2Hf_2O_7$ absorption and sharp peaks at 488 and 525 nm are assigned to Er^{3+} absorption lines. This clearly proves that the emission from Er^{3+} occurs through energy transfer from $La_2Hf_2O_7$ matrix to Er^{3+} ion. Similarly, the emission and excitation spectrum of HfO_2 sol-gel thin layer made with LaF_3:Eu (Figure 5.9) and LaF_3:Nd (Figure 5.10) nanoparticles also proves that the emissions from lanthanide ions are occurring through energy transfer from matrix to lanthanide ions.

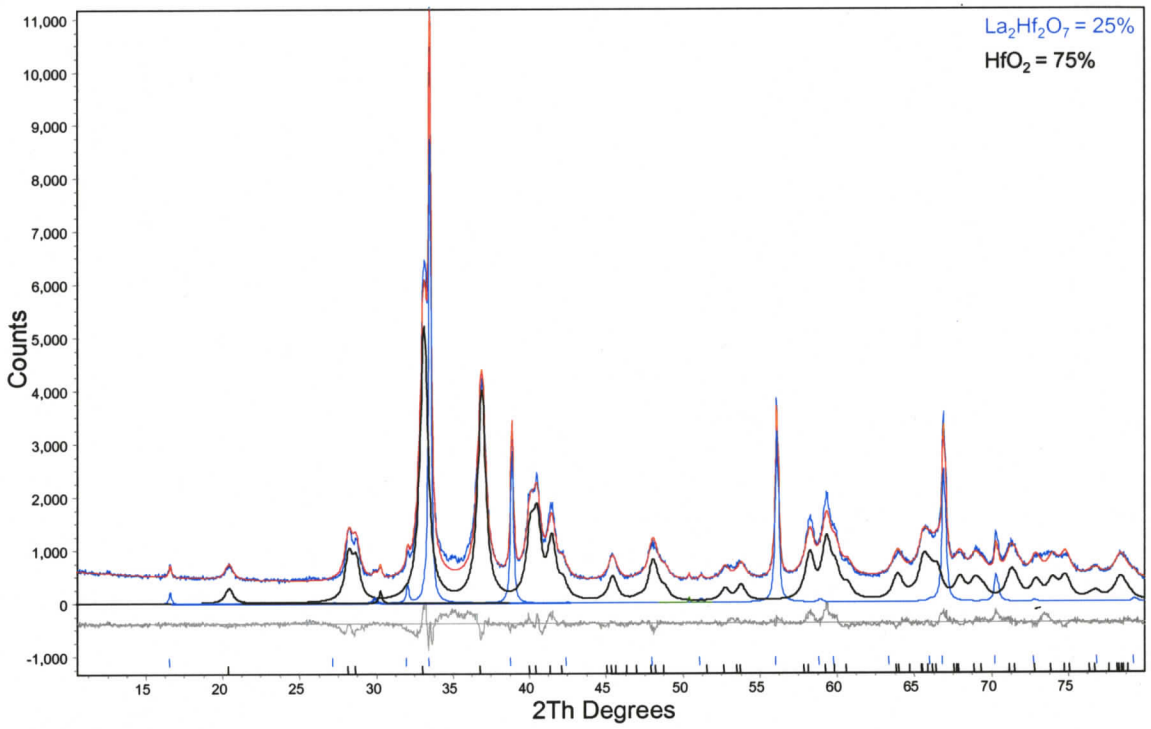

Figure 5.7. XRD pattern (Rietveld refinement plot) of a HfO_2 film prepared at 800 °C made LaF_3:Eu nanoparticles. Black lines: HfO_2 phase, Blue lines: $La_2Hf_2O_7$, Grey lines: risidue, Red line: sample.

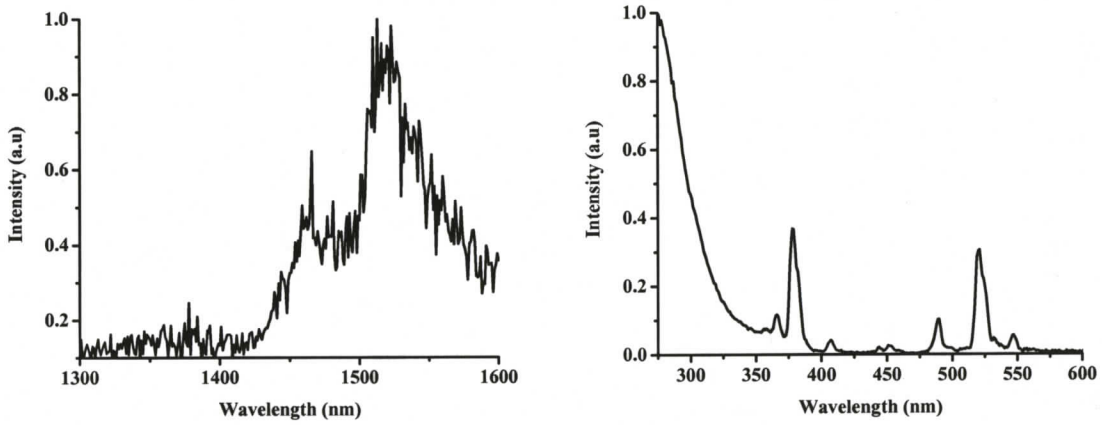

Figure 5.8. HfO_2 sol-gel thin layer made with LaF_3:Er nanoparticles a) Emission spectrum under 270 nm excitation, b) excitation spectrum (emission collected at 1530 nm).

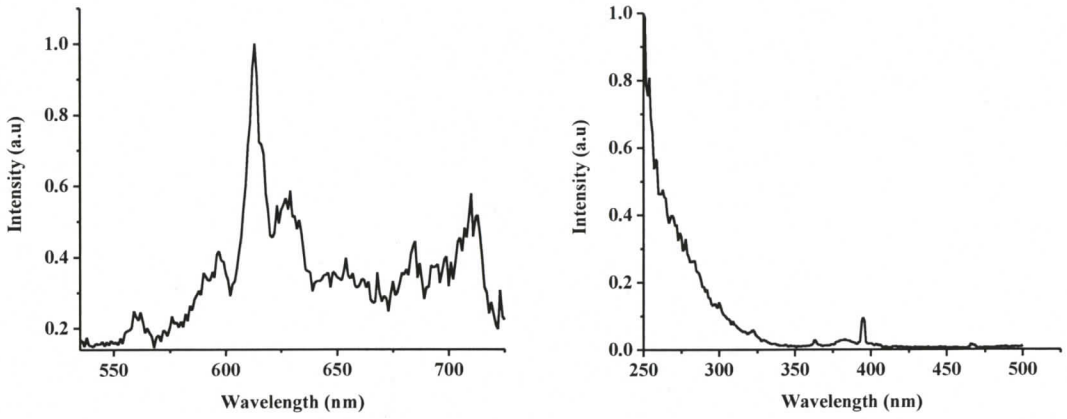

Figure 5.9. HfO_2 sol-gel thin layer made with LaF_3:Eu nanoparticles a) Emission spectrum under 270 nm excitation, b) excitation spectrum (emission collected at 612 nm).

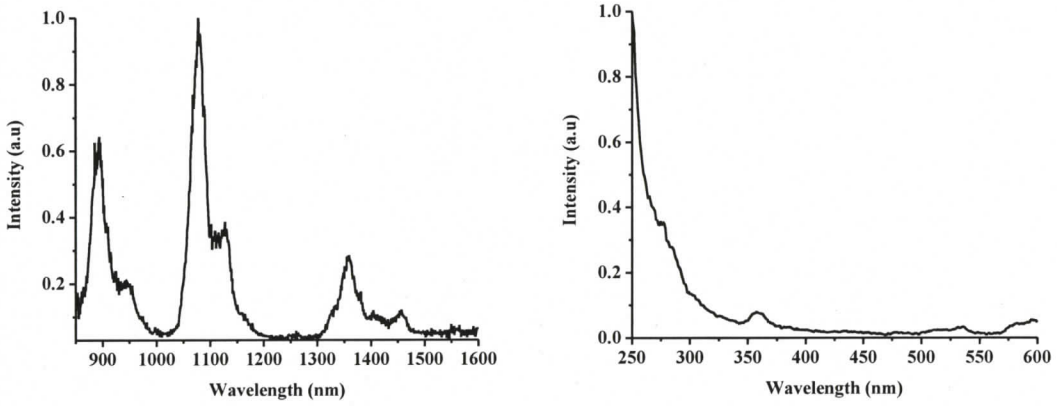

Figure 5.10. HfO_2 sol-gel thin layer made with LaF_3:Nd nanoparticles a) Emission spectrum under 270 nm excitation, b) excitation spectrum (emission collected at 1070 nm).

5.2.3. ZrO_2 sol-gel thin film made with $LaF_3:Nd^{3+}$ nanoparticle

Similar to HfO_2, sol-gel thin films of ZrO_2 also show energy transfer from the matrix to lanthanide ions. Figure 5.11a demonstrates the emission spectrum of ZrO_2 sol-

gel thin film made with $LaF_3:Nd^{3+}$ nanoparticles in which the major emission lines of Nd^{3+} are present. The excitation spectrum of Nd^{3+} ion shows a broad absorption from 250-350 nm which is assigned to $La_2Zr_2O_7$ and the sharp peaks is assigned to Nd^{3+} absorption lines (Figure 5.11). The excitation spectrum clearly demonstrates that energy transfer happens from the $La_2Zr_2O_7$ matrix to Nd^{3+} ions.

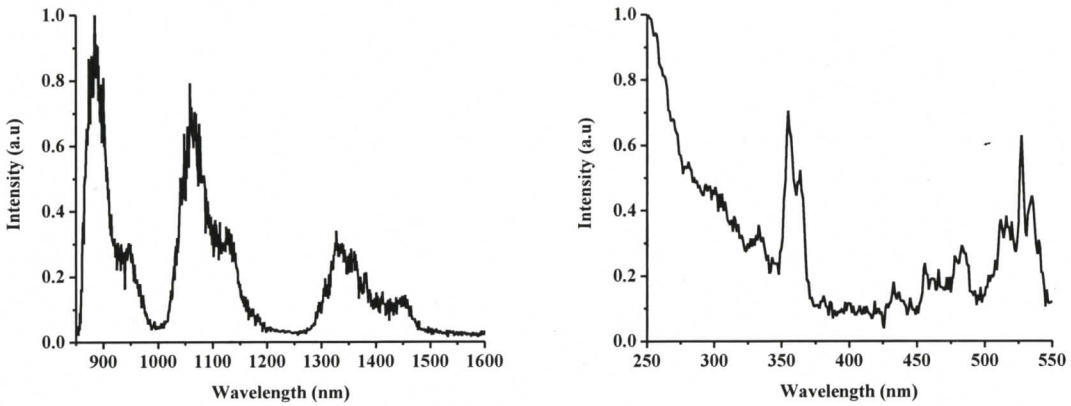

Figure 5.11. ZrO_2 sol-gel thin layer made with LaF_3:Nd nanoparticles a) Emission spectrum under 270 nm excitation, b) excitation spectrum (emission collected at 1070 nm).

The excitation spectra of all the semiconductor (In_2O_3, HfO_2, and ZrO_2) sol-gel thin films made with $LaF_3:Ln^{3+}$ nanoparticles clearly supports that energy transfer occurs from semiconductor matrix to lanthanide ions. Despite the efficient energy transfer from semiconductor sol-gel thin to lanthanide ions (potentially useful in solid state LEDs), additionally, a more general method is needed to synthesise dispersible semiconductor nanoparticles doped with lanthanide ions (potentially useful in polymer LEDs). The next

approach is to synthesise dispersible semiconductor-coated lanthanide-doped nanoparticles.

5.2.4. Dispersible In_2O_3 coated LaOF:Ln^{3+} nanoparticles

Materials scratched from the substrate of In_2O_3 sol-gel thin film made with LaF_3:Ln^{3+} nanoparticles are the starting materials for this synthesis. These materials were heated in oleic acid at 180 °C. Detailed experimental method for the synthesis of oleic acid-stabilised In_2O_3 coated LaOF:Er nanoparticles are given in the experimental section. Characterisation of oleic acid-stabilised In_2O_3 coated LaOF:Er nanoparticles has been confirmed by ^{1}H NMR , AFM, and TEM image of the nanoparticles. The broad NMR peaks around 5.1 ppm is characteristic of the vinylic protons of the oleic acid ligands coordinated to the surface of the nanoparticles (Figure 5.12). The NMR peaks between 1.2-2.4 ppm are the characteristics of other alkane protons of oleic acid. The broadening is ascribed to the inhomogeneous distribution of the magnetic environment around nanoparticles and a reduction in the rotational freedom of the ligand. The AFM image of oleic acid-stabilised In_2O_3 coated LaOF:Er nanoparticles shows that the majority of the particles have heights in the range of 60-70 nm (Figure 5.13). The larger features are due to NP agglomeration, which likely occured during sample preparation i.e. due to solvent evaporation. Figure 5.14 demonstrates the TEM image of oleic acid-stabilised In_2O_3-coated LaOF:Er^{3+} nanoparticles, in which the contrast in the nanoparticles clearly shows that there are core-shell structures present in the sample. It strongly suggests that almost all the LaOF:Er^{3+} nanoparticles are coated with In_2O_3 with the average size of 60-70 nm. The size deduced from the TEM image matches with the size analysis done by AFM

image. Moreover, the TEM image shows that In_2O_3 nanoparticles may have more than one LaOF:Er^{3+} nanoparticle and that they are not necessarily present in the centre of the nanoparticle.

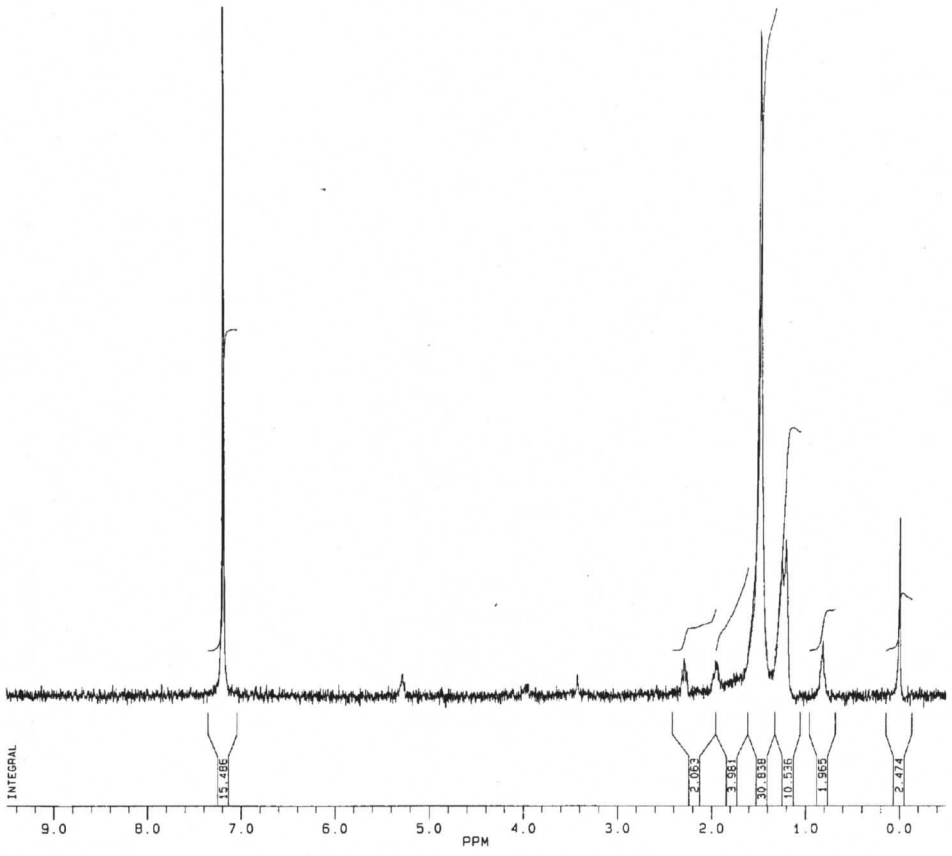

Figure 5.12. ^{1}H NMR of oleic acid-stabilised In_2O_3 coated LaOF:Er^{3+} nanoparticles.

Figure 5.15a demonstrates the emission spectrum of oleic acid-stabilised In_2O_3 coated LaOF:Er nanoparticles which is similar to In_2O_3 sol-gel thin film made with LaF_3:Er nanoparticles. The excitation spectrum (Figure 5.15b) of Er^{3+} by collecting 1530 nm emission of Er^{3+} ion is also similar to In_2O_3 sol-gel thin film made with LaF_3:Er

nanoparticles. This clearly proves that the emission is occurring through energy transfer from the In_2O_3 matrix to Er^{3+} ion. In order to show the generality of the method oleic acid-stabilised In_2O_3 coated LaOF:Eu nanoparticles were prepared by the same procedure. These nanoparticles also proves the energy transfer from In_2O_3 matrix to Eu^{3+} ion (Figure 5.16). The lifetime matches with the corresponding sol-gel thin layers.

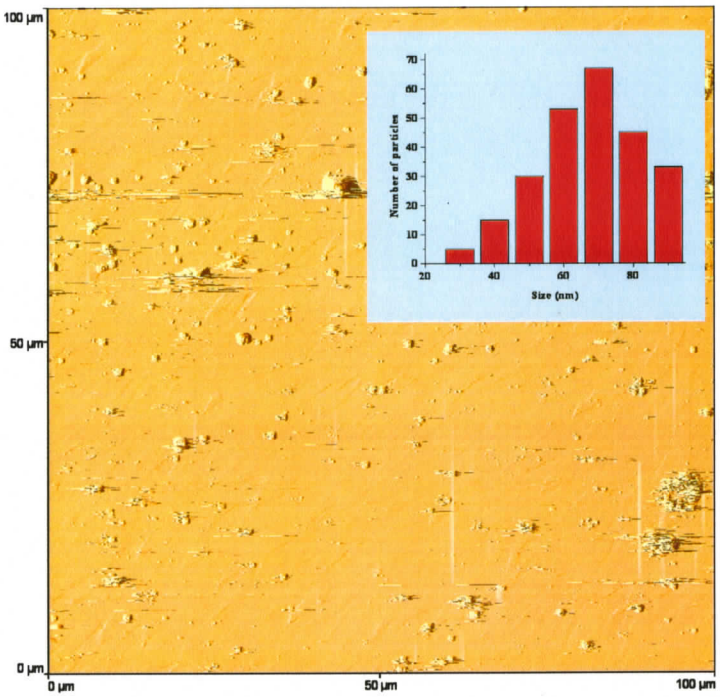

Figure 5.13. AFM image of oleic acid-stabilised In_2O_3 coated LaOF:Er^{3+} nanoparticles deposited on a glass substrate from a $CHCl_3$ dispersion.

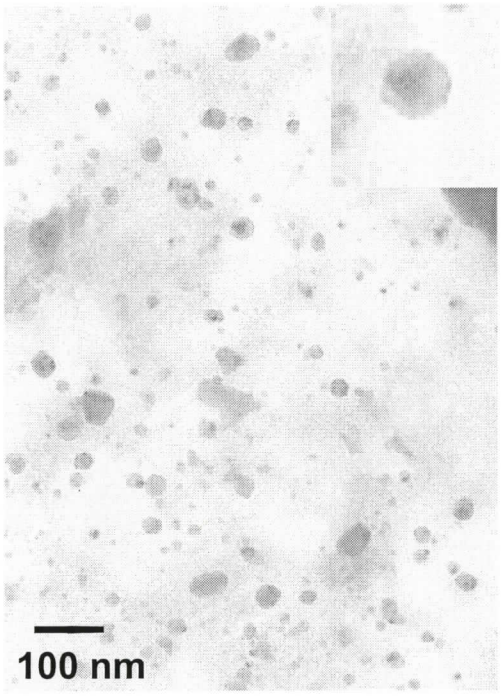

Figure 5.14. TEM image of oleic acid stabilised In_2O_3 coated LaOF:Er^{3+} nanoparticles on a copper grid deposited from a $CHCl_3$ dispersion.

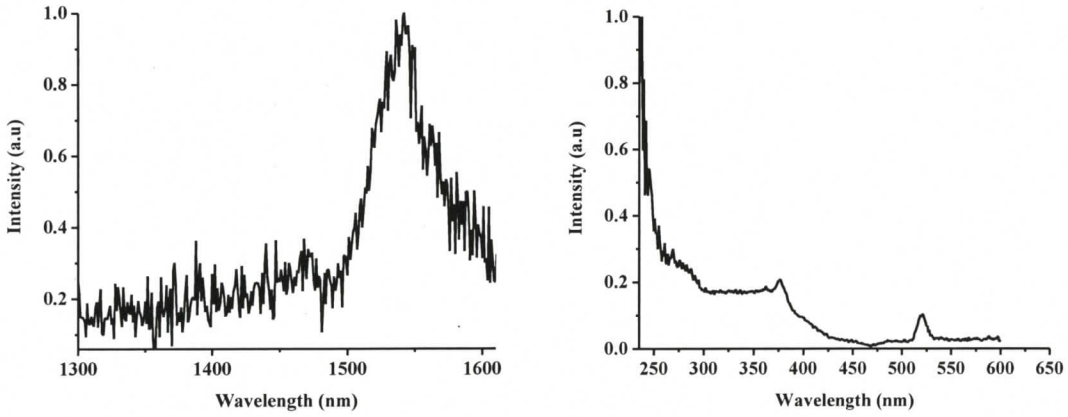

Figure 5.15. Oleic acid stabilised In_2O_3 coated LaOF:Er nanoparticles a) emission spectrum under 385 nm excitation, b) excitation spectrum of emission collected at 1540 nm.

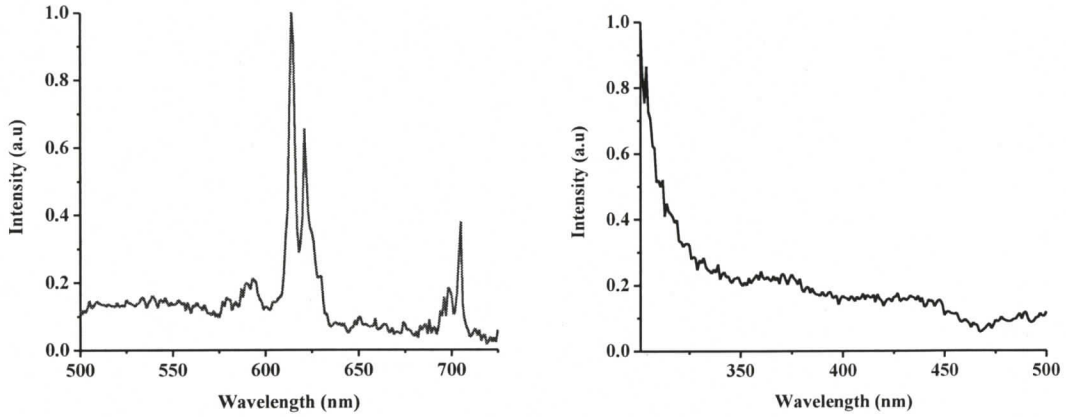

Figure 5.16. Oleic acid-stabilised In_2O_3 coated LaOF:Eu nanoparticles a) emission spectrum under 300 nm excitation, b) excitation spectrum of emission collected at 612 nm.

5.3 Conclusion

In this chapter, a general and facile method for the preparation of sol-gel thin films (In_2O_3, HfO_2, ZrO_2) made with $LaF_3:Ln^{3+}$ nanoparticles has been reported. These films show energy transfer from semiconductor matrix (In_2O_3, $La_2Hf_2O_7$, and $La_2Zr_2O_7$) to lanthanide ions upon optical excitation of the semiconductor thin film. Oleic acid-stabilised In_2O_3 coated $LaOF:Ln^{3+}$ nanoparticles were prepared and they also show energy transfer from In_2O_3 to lanthanide ions.

5.4. Experimental Section

All chemicals were used as received without further purification. The lanthanide salts, $La(NO_3)_3.6H_2O$, $Tb(NO_3)_3.5H_2O$, $Eu(NO_3)_3.5H_2O$, $Er(NO_3).6H_2O$,

$Nd(NO_3)_3.5H_2O$, and $Y(NO_3)_3.5H_2O$ all having a purity of 99.99%, oleic acid (90%) indium tert-butoxide (5 wt% solution in butanol), zirconium propoxide (70 wt% solution in 1-propanol), hafnium *tert* -butoxide (99.99%) HCl (30 wt% solution) NH_4OH_{aq} (35% wt% aqueous solution), and sodium fluoride (99%) were purchased from Aldrich. Citric acid (99%) was purchased from Caledon Laboratories Ltd.

5.4.1 Preparation of Indium oxide sol-gel thin films

Indium *tert*-butoxide (1.43 ml) solution was dissolved in 8 ml of absolute ethanol and followed by the addition of 0.5 ml of concentrated HCl. 15 mg of $La_{0.95}Ln_{0.05}F_3$ (Ln = Tb, Eu, Er, and Nd) nanoparticles were dissolved in 2 ml distilled water and added dropwise. The solution was stirred for 24 h to get a clear sol. The sol was then spin-coated on a quartz substrate at 2500 rpm and heated to 400°C from 25°C in 1.40 h, staying at 400°C for 30 min, and then heated to 800 °C in 2 h and staying at 800 °C for 12 h under ambient environment.

5.4.2. Preparation of HfO_2 sol-gel thin films

Hafnium *tert*-propoxide (1 ml) solution was dissolved in 9 ml of absolute ethanol and followed by the addition of 0.5 ml of concentrated HCl. 50 mg of $La_{0.95}Ln_{0.05}F_3$ (Ln = Eu, Er, and Nd) nanoparticles were dissolved in 2 ml distilled water and added dropwise. The solution was stirred for 24 h to get a clear sol. The sol was then spincoated on a quartz substrate at 2500 rpm and the heating procedure is same as In_2O_3 thin film.

5.4.3. Preparation of ZrO_2 sol-gel thin films

Zirconium propoxide (2 ml) solution was dissolved in 9 ml of absolute ethanol and followed by the addition of 0.5 ml of concentrated HCl. 50 mg of $La_{0.95}Ln_{0.05}F_3$ (Ln = Nd) nanoparticles were dissolved in 2 ml distilled water and added dropwise. The solution was stirred for 24 h to get a clear sol. The sol was then spin-coated on a quartz substrate at 2500 rpm and the heating procedure is same as In_2O_3 thin film.

5.4.4. Preparation of oleic acid-stabilised In_2O_3 coated LaOF:Ln^{3+} nanoparticles

The thin film material (50 mg) present in the 800 °C heated In_2O_3 sol-gel thin film made with LaF_3:Ln^{3+} (Ln = Er and Eu) nanoparticles were scratched from the substrate and the yellowish white powder was mixed with 2 ml of oleic acid. The mixture was sonicated for 30 min. The mixture was then heated at 180 °C for 24 h under argon atmosphere. The mixture was cooled to room temperature and the oleic acid stabilised nanoparticles were centrifuged and washed with 5 ml of methanol (centrifuged after every washing) several times to remove excess oleic acid. The particles were dried under vacuum for 24 h and redispersed in chloroform through sonication for 20 min. The dispersions are stable for 2 days. Very few particles had settled at the bottom of the container after 2 days.

5.4.5. NMR measurements

Room temperature ^{1}H NMR data were recorded using Bruker AC 300 instrument. The basic frequencies for the ^{1}H nucleus is 300.13 MHz. ^{1}H NMR of In_2O_3 coated

LaOF:Er particles stabilised with oleic acid ligand δ ($CDCl_3$) : 5.2 – 5.4 (broad, -C<u>H</u>=C<u>H</u>-), 2.2-2.4 (broad, -C<u>H_2</u>-COOH), 1.8-2.0 (broad, -C<u>H_2</u>-CH=CH-C<u>H_2</u>-), 1.2-1.8 (broad, -(C<u>H_2</u>)$_5$-C<u>H_2</u>-CH_2-CH=CH-CH_2-(C<u>H_2</u>)$_5$-), and 0.9 (C<u>H_3</u>). The peak at 7.2 belongs to solvent C<u>H</u>Cl_3.

5.4.6. AFM measurements

AFM images were recorded in the contact mode using a Thermo microscope AFM scanner having a silicon nitride tip (model MLCT-EXMT-A) supplied by Veeco Instruments. The particles were dispersed in chloroform and a drop of the solution was put on a glass sheet (5 x 5 mm^2) and allowed to dry before mounting the sheet on the sample holder. The measurements were done with a resolution of 500 x 500 pixels per image and an image dimension of 100 x 100 μm^2. The average particle height was determined by measuring the individual particle heights for over 100 particles.

5.4.7. Transmission Electron Microscope (TEM)

TEM of the In_2O_3-coated *LaOF:*Ln^{3+} nanoparticles was carried out using a Hitachi H-7000 microscope, operated at 100 kV. Around 1-2 mg of sample was dispersed in 5 ml of chloroform by sonication (20 min) and a drop of this mixture was evaporated on a carbon-coated 300 mesh copper grids. Around 8 images were recorded from different regions of the same sample and an average particle size was obtained based on a minimum of 100 particles.

5.4.8. Luminescence studies

All the emission spectra, lifetime analysis were done by using the same set-up reported in chapter 3.

5.4.9. Powder X-Ray diffraction studies

XRD analysis were done by using the same set-up reported in chapter 3.

References

(1) Wang, F.; Tan, W. B.; Zhang, Y.; Fan, X. P.; Wang, M. Q. *Nanotechnol.* **2006**, *17*, R1.

(2) Kenyon, A. J. *Prog. in Quant. Electron.* **2002**, *26*, 225.

(3) Jia, C. J.; Sun, L. D.; You, L. P.; Jiang, X. C.; Luo, F.; Pang, Y. C.; Yan, C. H. *J. Phys. Chem. B* **2005**, *109*, 3284.

(4) Sun, Y. J.; Liu, H. J.; Wang, X.; Kong, X. G.; Zhang, H. *Chem. Mater.* **2006**, *18*, 2726.

(5) Riwotzki, K.; Haase, M. *J. Phys. Chem. B* **2001**, *105*, 12709.

(6) Liu, G. X.; Hong, G. Y.; Wang, J. X.; Dong, X. T. *Nanotechnol.* **2006**, *17*, 3134.

(7) Stouwdam, J. W.; Raudsepp, M.; van Veggel, F. C. J. M. *Langmuir* **2005**, *21*, 7003.

(8) Coppo, P.; Duati, M.; Kozhevnikov, V. N.; Hofstraat, J. W.; De Cola, L. *Angew. Chem. Int. Ed.* **2005**, *44*, 1806.

(9) Kang, T. S.; Harrison, B. S.; Bouguettaya, M.; Foley, T. J.; Boncella, J. M.; Schanze, K. S.; Reynolds, J. R. *Adv. Funct. Mater.* **2003**, *13*, 205.

(10) Slooff, L. H.; Polman, A.; Cacialli, F.; Friend, R. H.; Hebbink, G. A.; van Veggel, F. C. J. M.; Reinhoudt, D. N. *Appl. Phys. Lett.* **2001**, *78*, 2122.

(11) Li, S. F.; Zhong, G. Y.; Zhu, W. H.; Li, F. Y.; Pan, J. F.; Huang, W.; Tian, H. *Chem. Lett.* **2005**, *34*, 688.

(12) Zheng, Y. X.; Zhou, Y. H.; Yu, J. B.; Yu, Y. N.; Zhang, H. J.; Gillin, W. P. *J. Phys. D-Appl. Phys.* **2004**, *37*, 531.

(13) Conde-Gallardo, A.; Garcia-Rocha, M.; Hernandez-Calderon, I.; Palomino-Merino, R. *Appl. Phys. Lett.* **2001**, *78*, 3436.

(14) Conde-Gallardo, A.; Garcia-Rocha, M.; Palomino-Merino, R.; Velasquez-Quesada, M. P.; Hernandez-Calderon, I. *Appl. Sur. Sci.* **2003**, *212*, 583.

(15) Garcia-Rocha, M.; Conde-Gallardo, A.; Hernandez-Calderon, I.; Palomino-Merino, R. *Mod. Phys. Lett. B* **2001**, *15*, 769.

(16) Jadwisienczak, W. M.; Lozykowski, H. J. *Opt. Mater.* **2003**, *23*, 175.

(17) Jadwisienczak, W. M.; Lozykowski, H. J.; Berishev, I.; Bensaoula, A.; Brown, I. G. *J. Appl. Phys.* **2001**, *89*, 4384.

(18) Jadwisienczak, W. M.; Lozykowski, H. J.; Xu, A.; Patel, B. *J. Electron. Mater.* **2002**, *31*, 776.

(19) Palomino-Merino, R.; Conde-Gallardo, A.; Garcia-Rocha, M.; Hernandez-Calderon, I.; Castano, V.; Rodriguez, R. *Thin Solid Films* **2001**, *401*, 118.

(20) Conde-Gallardo, A.; Garcia-Rocha, M.; Calderon, I. H.; Palomino-Merino, R. *Mod. Phys. Lett. B* **2001**, *15*, 813.

(21) Stouwdam, J. W.; van Veggel, F. C. J. M. *Chemphyschem* **2004**, *5*, 743.

(22) Hayakawa, T.; Selvan, S. T.; Nogami, M. *J. Sol-Gel Sci. Tech.* **2000**, *19*, 779.

(23) Hayakawa, T.; Selvan, S. T.; Nogami, M. *J. Lumin.* **2000**, *87-9*, 532.

(24) Selvan, S. T.; Hayakawa, T.; Nogami, M. *J. Non-Cryst. Sol.* **2001**, *291*, 137.

(25) Nogami, M.; Enomoto, T.; Hayakawa, T. *J. Lumin.* **2002**, *97*, 147.

(26) Bol, A. A.; Meijerink, A. *Phys. Stat. Sol. B* **2001**, *224*, 173.

(27) Bhargava, R. N. *J. Lumin.* **1996**, *70*, 85.

(28) Bhargava, R. N. *J. Lumin.* **1997**, *72-4*, 46.

(29) Bhargava, R. N.; Gallagher, D.; Welker, T. *J. Lumin.* **1994**, *60-1*, 275.

(30) Kane, R. S.; Cohen, R. E.; Silbey, R. *Chem. Mater.* **1999**, *11*, 90.

(31) Ihara, M.; Igarashi, T.; Kusunoki, T.; Ohno, K. *J. Electrochem. Soc.* **2000**, *147*, 2355.

(32) Okamoto, S.; Kobayashi, M.; Kanemitsu, Y.; Kushida, T. *Phys. Stat. Sol. B* **2002**, *229*, 481.

(33) Qu, S. C.; Zhou, W. H.; Liu, F. Q.; Chen, N. F.; Wang, Z. G.; Pan, H. Y.; Yu, D. P. *Appl. Phys. Lett.* **2002**, *80*, 3605.

(34) Bol, A. A.; van Beek, R.; Meijerink, A. *Chem. Mater.* **2002**, *14*, 1121.

(35) Raola, O. E.; Strouse, G. F. *Nano Lett.* **2002**, *2*, 1443.

(36) Terki, R.; Feraoun, H.; Bertrand, G.; Aourag, H. *Comp. Mater. Sci.* **2005**, *33*, 44.

(37) Terki, R.; Feraoun, H.; Bertrand, G.; Aourag, H. *J. Appl. Phys.* **2004**, *96*, 6482.

(38) De la Rosa-Cruz, E.; Diaz-Torres, L. A.; Salas, P.; Mendoza, D.; Hernandez, J. M.; Castano, V. M. *Opt. Mater.* **2002**, *19*, 195.

(39) De la Rosa-Cruz, E.; Diaz-Torres, L. A.; Salas, P.; Rodriguez, R. A.; Kumar, G. A.; Meneses, M. A.; Mosino, J. F.; Hernandez, J. M.; Barbosa-Garcia, O. *J. Appl. Phys.* **2003**, *94*, 3509.

(40) Del Castillo, J.; Rodriguez, V. D.; Yanes, A. C.; Mendez-Ramos, J.; Torres, M. E. *Nanotechnol.* **2005**, *16*, S300.

(41) Yanes, A. C.; Del Castillo, J.; Torres, M.; Peraza, J.; Rodriguez, V. D.; Mendez-Ramos, J. *Appl. Phys. Lett.* **2004**, *85*, 2343.

(42) Xin, H.; Ma, R. Z.; Wang, L. Z.; Ebina, Y. S.; Takada, K.; Sasaki, T. *Appl. Phys. Lett.* **2004**, *85*, 4187.

(43) Sudarsan, V.; van Veggel, F.; Herring, R. A.; Raudsepp, M. *J. Mater. Chem.* **2005**, *15*, 1332.

(44) Stouwdam, J. W.; van Veggel, F. *Langmuir* **2004**, *20*, 11763.

(45) Stouwdam, J. W.; van Veggel, F. *Nano Lett* **2002**, *2*, 733.

(46) Stouwdam, J. W.; Hebbink, G. A.; Huskens, J.; van Veggel, F. *Chem. Mater.* **2003**, *15*, 4604.

(47) Sosa, R.; Foldvari, I.; Watterich, A.; Munoz, A.; Maillard, R. S.; Kugel, G. *J. Lumin.* **2005**, *111*, 25.

(48) Liu, Q. S.; Lu, W. G.; Ma, A. H.; Tang, J. K.; Lin, J.; Fang, J. Y. *J. Am. Chem. Soc.* **2005**, *127*, 5276.

CHAPTER 6

Silica-coated Ln^{3+}-doped LaF_3 nanoparticles as new robust down- and up-converting biolabels*©

* The major part of the work in this chapter was published: Sri Sivakumar, Peter R. Diamente, and Frank C.J.M. van Veggel, *Chem. Eur. J.* **2006**, *12*, 5878-5884. Mr. Peter R. Diamente did bioconjugation of silica-coated Tb^{3+}-doped LaF_3 nanoparticle.

6.1. Introduction

There is a large interest in the development of biomaterials for biological applications such as biolabeling, drug delivery, diagnostics of infectious and genetic diseases, etc.[1,2] Materials such as traditional organic dyes[3,4], quantum dots[5-9], and metal nanoparticles[10-12] are widely applied in biological analyses but have some limitations. Organic dyes have a number of known drawbacks such as weak photostability, broad absorption and emission band, and toxicity.[3,4] Various semiconductor quantum dots display high photostability, size-dependant emission, high quantum yields, and narrow emission bandwidth and have successfully been applied in biological applications.[5-9] However, they are still controversial because of their inherent toxicity and chemical instability.[13] Moreover, their inherent short-lived luminescent lifetime may overlap with the spontaneous background emission sources (natural fluorescence of biomolecules such as proteins is within 1-10 ns). Noble metal nanoparticles (e.g. gold nanoparticles) which are known to scatter and absorb visible light make them potentially suitable candidates for biosensors.[10-12] Though these noble metal nanoparticles posses biocompatibility, their optical properties in the visible region may overlap with natural proteins. Halas *et al.*[14,15] have addressed this issue in a different way by developing a gold nanoshell over a silica sphere of sub-micron size for bio-applications such as the integration of cancer imaging and therapy. Notwithstanding this progress, there is still a need for more efficient biolabels with high photostability, biocompatibility, optical properties, and ultrasensitivity to bioassays.

In order to address these key issues, the development of an alternative biomaterial via lanthanide-doped nanoparticle is gaining popularity due to their unique luminescent

properties such as sharp absorption and emission lines, high quantum yield, long lifetimes, and superior photostability.[16-23] In particular, lanthanide ions are known to exhibit both efficient energy down- and up-conversion emission properties, where the down-conversion process is the conversion of higher energy photons into lower energy photons, which is also widely exploited in quantum dots as well as in organic dyes.[24] In contrast, the up-conversion process converts lower energy photons via multiphoton processes into higher energy photons, and is, in general, based on sequential absorption and energy transfer steps.[25] One has to bear in mind that this event is different from multiphoton absorption processes which typically require high excitation densities.[25]

At present, there are only a selected number of reports on the use of lanthanide-based nanoparticles as potential biolabels that emit in the visible region, by either up-conversion or down-conversion processes.[13] Examples include the bioconjugation of Ln^{3+}-doped LaF_3 nanoparticle to avidin by our group,[26,27] and work done by Caruso and co-workers[28] with the functionalization of $LaPO_4$:Ce/Tb nanoparticles with streptavidin for biotin-streptavidin binding studies. In addition, a recent contribution from Li and co-workers[29] demonstrate that an Er^{3+}/Yb^{3+} up-converting nanoparticle label can be used in FRET type analysis, whereby the emission of the up-converting nanoparticle is quenched by the energy accepting gold nanoparticle that are functionalized with biotin for biotin-avidin detection and quantification. Although these lanthanide-based articles prove the principle of bioconjugation, they have three main drawbacks. The first is long term stability where it has been reported that ionic bound stabilizing ligands can be protonated off the surface of the nanoparticles in pH-dependent solutions.[26,27] The second is toxicity due to exposure of lanthanide ions to the body, and finally they emit only in the visible

region. Only a few reports have dealt these issues by developing a silica shell over the lanthanide-doped materials such as, silica-coated $YVO_4:Eu^{3+}$ nanoparticles functionalized with guanidinium for sodium channel targeting by Beaurepaire *et al.*[30], and silica-coated $Gd_2O_3:Tb^{3+}$ nanoparticle functionalized with streptavidin by Louis *et al.*[31] Additionally, Niedbala and co-workers[32] have done up-converting, silica-coated lanthanide-doped submicron-sized ceramic particles for DNA assays. The use of a silica coating over lanthanide-doped nanoparticles is an attractive alternative because the surface chemistry of silica spheres is well documented and silica is known to have benign effects in biological systems.[33] Up-converting and near-infrared (NIR) emitting biolabels with silica coating would be beneficial because up-converting materials can be excited with NIR light, which is outside the luminescent absorption range of biomolecules, thus minimizing loss of excitation energy to the surrounding material as compared to exciting with UV light.[13] Futhermore, excitation and emission in the NIR region can minimize interferences from the autofluorescence of proteins. However, these reports only showed emission in the visible region by a down-conversion process, and to the best of our knowledge, there are no reports available on silica-coated lanthanide-doped nanoparticles, which have near-infrared emission (750-2000 nm) via up- and down-conversion.

In this chapter, a general and easy method for the preparation and bioconjugation of silica-coated $LaF_3:Ln^{3+}$ nanoparticles is reported that display several non-overlapping emission lines that cover the visible to near-infrared region (450-1650 nm) though down-conversion as well as up-conversion processes, which can for instance be exploited in multiplexing applications.[34] The use of luminescent silica-coated $LaF_3:Ln^{3+}$ nanoparticle could have a number of potential advantages as probes in bioapplications over already

existing biolabels. First, LaF_3 has very low phonon energy and therefore minimizes the quenching of the excited state lanthanide ions and thus have high quantum yield.[18-22,26,27] Second, wide range of emission lines (450 – 1650 nm) can be achieved by doping with selected lanthanide ions. Third, the co-doping of the LaF_3 nanoparticle core with Yb^{3+} ions (for up-conversion) makes it possible to excite with 980 nm light source, which is outside the luminescent absorption range of biological molecules, thus minimizing loss of excitation energy to the surrounding material as compared to exciting with UV light. Fourth, excitation at 980 nm of the co-doped Yb^{3+} and Tm^{3+} nanoparticles produces a 800 nm emission line from Tm^{3+}, which is within the window (700-1300 nm) for which skin and other biological materials are most transparent, as compared to UV-Vis light, thus allowing for deeper penetration of excitation and easy escape of emission light.[14,15] Fifth, emission in the NIR region (from Yb^{3+}, Nd^{3+}, Er^{3+}) minimizes interferences from the auto-fluorescence of proteins. Sixth, silica is highly biocompatible and its surface chemistry is well documented for biological interactions. Seventh, the size of the silica shell can easily be adjusted to ease the secretion of nanoparticles though the kidney. Eighth, longer luminescent lifetimes (μs to ms range) allow for gated time-resolved fluorescence. The consequence of these long lifetimes is that the photo count per second could be low per single Ln^{3+}, but this is compensated for by the fact that we have many thousands of Ln^{3+} ions per nanoparticle. Finally, non size-dependent emission (unlike quantum dots), completely stable photocycle, and well established Ln^{3+} doping procedures[20,27,35,36] makes our approach an attractive alternative biolabel.

6.2 Results and discussion

6.2.1. Characterisation of silica-coated Ln^{3+}-doped LaF_3 nanoparticles

The nanoparticle core-matrix used to achieve the range of emission lines are the following: $La_{0.95}Eu_{0.05}F_3$ (LaF_3:Eu), $La_{0.95}Tb_{0.05}F_3$ (LaF_3:Tb), $La_{0.95}Nd_{0.05}F_3$ (LaF_3:Nd), $La_{0.75}$ $Yb_{0.20}Er_{0.05}F_3$ (LaF_3:Yb,Er), and $La_{0.75}Yb_{0.20}Tm_{0.05}F_3$ (LaF_3:Yb,Tm). First, the use of Tb^{3+} and Eu^{3+} ions resulted in green (541 nm) and red (591 and 612 nm) emission, respectively by energy down-conversion processes. Second, the use of Nd^{3+} ions gave 870, 1070 and 1350 nm emission lines, and Er^{3+} ions gave 1540 nm emission line via energy down-conversion processes. Additionally, the Er^{3+} ions gave green and red emission, and Tm^{3+} ion gave 800 nm emission, via energy up-conversion processes when co-doped with Yb^{3+} (λ_{ex} = 980 nm). The surface of the silica-coated LaF_3:Ln^{3+} nanoparticles were modified with 3-aminopropyltrimethoxysilane (APTMS), followed by the reaction with biotin-*N*-hydroxysuccinimide for subsequent specific binding to fluorescein isothiocyanate-labeled avidin (FITC-avidin), for which the FITC signal is monitored. The present work takes advantage of our recently published procedure to improve the up-conversion and NIR emission of lanthanide ions in sol-gel derived thin films (SiO_2, ZrO_2, and Al_2O_3), of which an important aspect is the effective separation of lanthanide ions from the high phonon energy matrix, residual OH groups, and the absence of lanthanide ion clustering.[35,36]

Shown in Scheme 6.1 is an outline of the step-wise preparation of the silica-coated LaF_3:Ln^{3+} nanoparticles, starting from the citrate-stabilised LaF_3:Ln^{3+} precursor

nanoparticles as the core matrix, followed by the formation of the silica shell via a modified Stöber process,[37] and then followed by its subsequent bioconjugation to FITC-avidin. To further our earlier work on the improvement of the up-converted and NIR emission of lanthanide ions in sol-gel derived thin films,[35,36] silica-coated LaF_3:Yb,Er, LaF_3:Yb,Tm, LaF_3:Nd (before surface modification with APTMS) were heated at 800°C for 12 h to improve significantly the NIR luminescence as well as up-conversion efficiency. Our previous report showed the presence of a non-stoichiometric lanthanum silicate phase ($La_{9.31}Si_{6.24}O_{26}$) along with the expected LaF_3 phase from X-ray diffraction (XRD) studies carried out on a silica-coated LaF_3:Tm^{3+} nanoparticle heated at 800°C. We assume that the same phases would be present in this sample also.

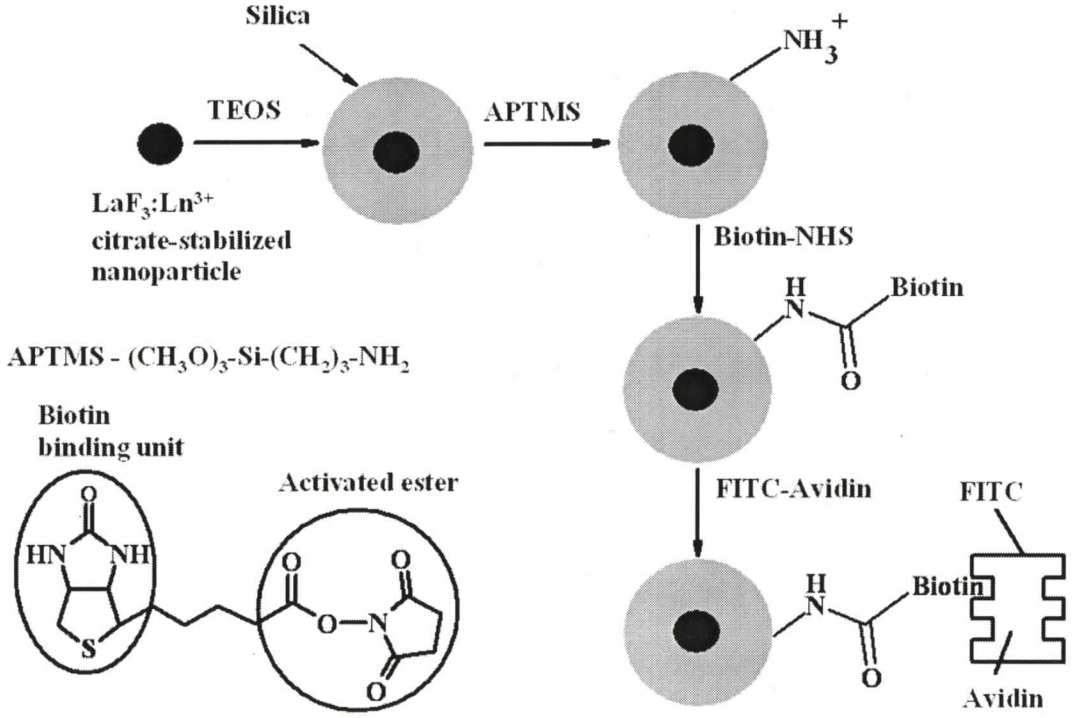

Scheme 6.1. Schematic illustration of preparation and bio-conjugation of silica-coated LaF_3:Ln^{3+} nanoparticles (not to scale).

The transmission electron microscopy (TEM) image shown in Figure 6.1 is of the as-prepared silica-coated LaF_3:Nd nanoparticles, which clearly shows that almost all the silica beads have a single core LaF_3:Nd nanoparticle (~5 nm) in the center with an average shell thickness of ~ 17 nm (±5 nm). The LaF_3:Nd core has a slightly higher contrast than the SiO_2 shell.

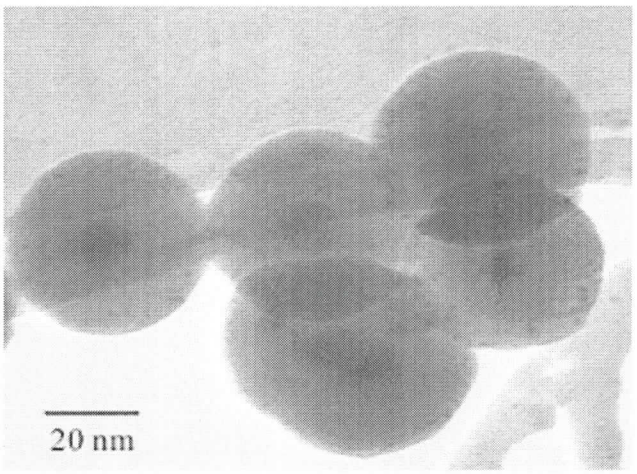

Figure 6.1. TEM image of as-prepared silica-coated LaF_3:Nd nanoparticles.

Figure 6.2a shows the emission spectrum of the as-prepared silica-coated LaF_3:Eu nanoparticles, in which the major emission bands of the Eu^{3+} ions at 590 nm and 612 nm are assigned to the $^5D_0$ to $^7F_1$ and $^5D_0$ to $^7F_2$ transitions. Detailed analysis of the emission spectrum is reported by us elsewhere.[19,20] The effective lifetime (defined in chapter 3) of 5.9 ms is assigned to the $^5D_0$ level (insert in Figure 6.2a) with an estimated quantum yield of 88% based on the radiative lifetime of 6.9 ms. Additionally, the emission spectrum of the as-prepared silica-coated LaF_3:Tb^{3+} nanoparticles is shown in Figure 6.2b, in which the most intense peak at 545 nm corresponds to $^5D_4$ to $^7F_5$ transition, and the peaks at 586 and 623 nm correspond to the $^5D_4$ to $^7F_4$ and $^7F_3$ transitions, respectively. The effective

lifetime of 3.7 ms is attributed to the $^5D_4$ level (insert in Figure 6.2b) with an estimated quantum yield of 76% based on the radiative lifetime of 4.9 ms.[16]

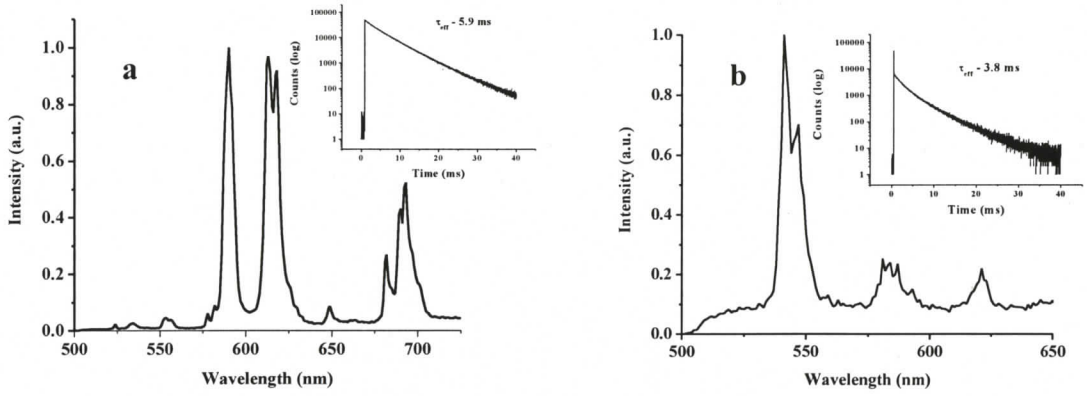

Figure 6.2. a) Emission spectrum of as-prepared silica-coated LaF_3:Eu nanoparticles (λ_{ex} = 464 nm). Insert: decay curve for silica-coated LaF_3:Eu nanoparticles before surface modification. (λ_{ex} = 464 nm, λ_{em} = 591 nm). b) Emission spectrum of as-prepared silica-coated LaF_3:Tb nanoparticles (λ_{ex} = 485 nm). Insert: decay curve for silica-coated LaF_3:Tb nanoparticles before surface modification.. (λ_{ex} = 485 nm, λ_{em} = 542 nm).

Figure 6.3 shows the TEM image of silica-coated LaF_3:Nd nanoparticle heated at 800°C for 12 h, resulting in the beads to contract to an average shell thickness of ~ 15 nm (±5 nm) with no observable effects of particle fusing.

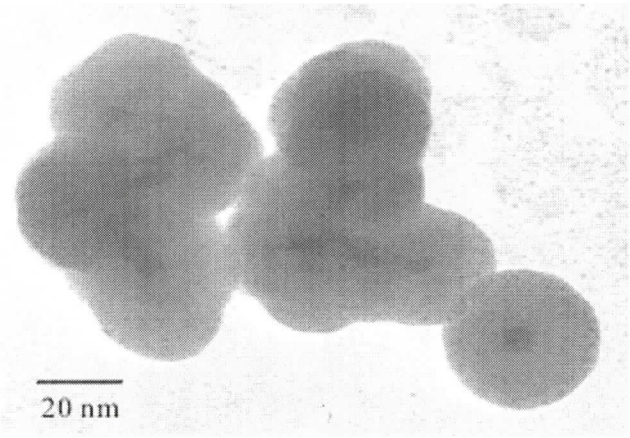

Figure 6.3. TEM image of as 800°C heated silica-coated LaF_3:Nd nanoparticles before surface modification.

Figure 6.4a shows the emission spectrum of the silica-coated LaF_3:Nd nanoparticles, where the emission peaks at 870 nm, 1070 nm, and 1330 nm are from $^4F_{3/2}$ transitions to $^4I_{13/2}$, $^4I_{11/2}$, and $^4I_{9/2}$, respectively, with an effective luminescent lifetime of 170 μs (insert in Figure 6.4a). Due to the ability of lanthanide ions to be excited indirectly though the sensitized emission of another lanthanide ion, Figure 6.4b shows the emission spectrum of silica-coated LaF_3:Yb,Er nanoparticles, via sensitized emission from $Yb^{3+}$to the Er^{3+} ions, by direct excitation of the Yb^{3+} ions at 940 nm. The importance of this spectrum demonstrates that though Er^{3+} has no absorption lines at this wavelength, this process results in the simultaneous observation of very weak emission of Yb^{3+} at 980 nm (attributed to the $^2F_{5/2}$ to $^2F_{7/2}$ transition), and the shown sensitized emission of the Er^{3+} ions at 1540 nm ($^4I_{13/2}$ to $^4I_{15/2}$ transition), with an effective lifetime of 1.8 ms from the $^4I_{13/2}$ level (insert in Figure 6.4b).

The up-conversion emission spectrum of the 800°C heated silica-coated LaF_3:Yb,Er nanoparticles, Figure 6.5a shows the emission spectrum of the Er^{3+} ions by

up-conversion, with the peaks at 515, 540 nm, and 660 nm being assigned to the $^2H_{11/2}$ to $^4I_{15/2}$, $^4S_{3/2}$ to $^4I_{15/2}$, and $^4F_{9/2}$ to $^4I_{15/2}$ transitions, respectively. Furthermore, Figure 6.5b demonstrates the up-conversion emission spectrum of heated silica-coated LaF_3:Yb,Tm nanoparticles, in which the emission band around 800 nm is a result of the $^3H_4$ to $^3H_6$ transition of Tm^{3+} ions. Moreover, a weak Tm^{3+} emission band at 475 nm was observed and assigned to the $^1G_4$ to $^3H_6$ transition (insert in Figure 6.5b), and is also a result of the up-conversion process.

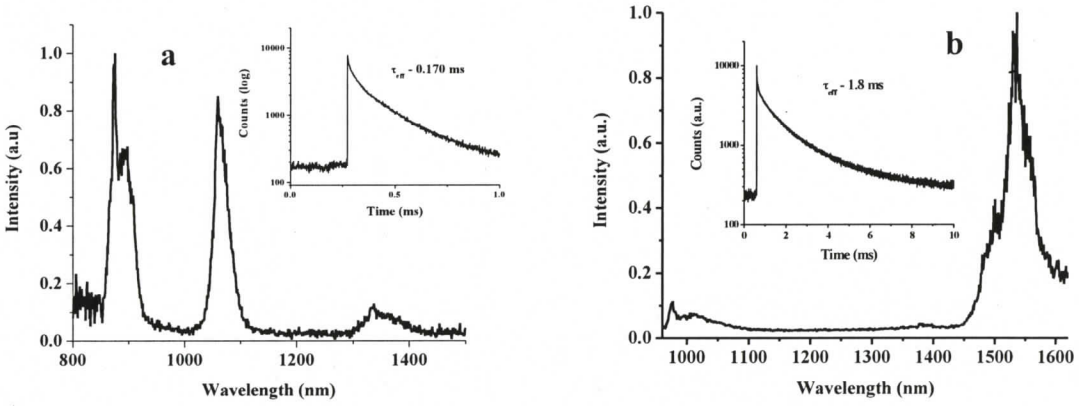

Figure 6.4. a) Emission spectra of 800°C heated silica-coated LaF_3:Nd nanoparticles (λ_{ex} = 514 nm). Insert: decay curve for 800°C heated silica-coated LaF_3:Nd nanoparticles before surface modification. (λ_{ex} = 514 nm, λ_{em} = 1070 nm). b) Emission spectra of 800°C heated silica-coated LaF_3:Yb,Er nanoparticle (λ_{ex} = 980 nm). Insert: decay curve for 800°C heated silica-coated LaF_3:Yb,Er nanoparticles before surface modification. (λ_{ex} = 940 nm, λ_{em} = 1540 nm).

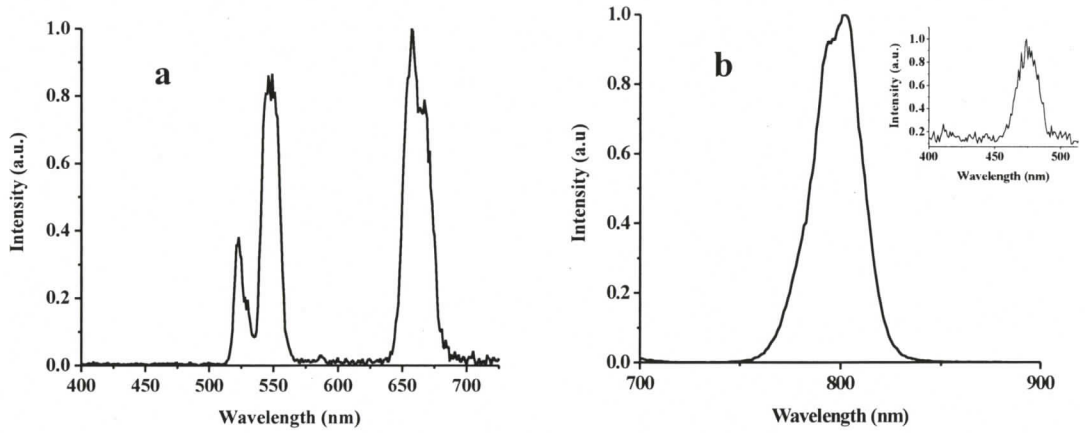

Figure 6.5. a) Up-conversion emission spectrum of 800°C heated silica-coated LaF_3:Yb,Er nanoparticles (λ_{ex} = 980 nm), b) Up-conversion emission spectrum of 800°C heated silica-coated LaF_3:Yb,Tm nanoparticles (λ_{ex} = 980 nm). Insert: Up-conversion emission spectrum of 800°C heated silica-coated LaF_3:Yb,Tm nanoparticles before surface modification (λ_{ex} = 980 nm).

The mechanism of the up-conversion process is occurring via energy transfer (ET) rather than an excited state absorption (ESA) or photon-avalanche (PA) process.[25] Blue emission from Tm^{3+} ions is a thee-photon process. The detailed mechanism of up-conversion of Tm^{3+} has been discussed in chapter 3. Green and red emission from Er^{3+} is a two photon process. It has been already discussed in chapter 4 that the power dependence graph of low Yb^{3+} concentration shows the slope of ~2 in most of the power range. Shown in Figure 6.6 are the schematic diagrams of the energy levels and possible energy transfer processes of the silica-coated LaF_3:Yb,Er and LaF_3:Yb,Tm nanoparticles.

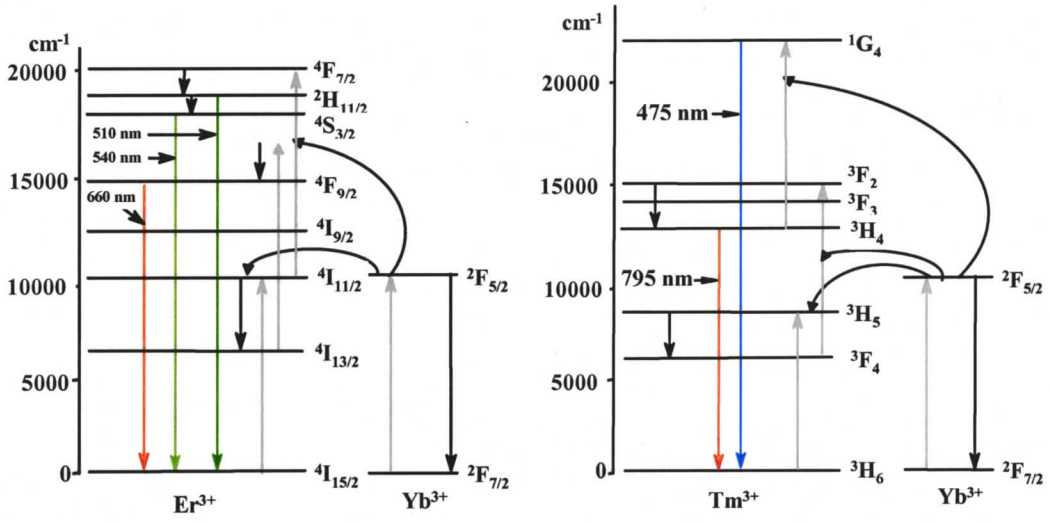

Figure 6.6. Energy level of Er^{3+}, Tm^{3+} and Yb^{3+} ions as well as the possible up-conversion mechanisms based on reference 9.

6.2.2. Bioconjugation of silica-coated Ln^{3+}-doped LaF_3 nanoparticles

To test the ability of the core-shell silica nanoparticles to be bound to a biological system, surface modification of the silica shell with biotin was used as a model for nanoparticle binding with FITC-avidin, and the extent of binding was monitored by the FITC emission intensity. Due to the biologically inert nature of silica, the shell had to be modified first in a two-step process in order to impart biotin activity, as shown in scheme 6.1.

The emission spectra of bioconjugation of silica-coated LaF_3:Tb nanoparticles to FITC-avidin, which is overlaid along with non-biotinylated particles as a control experiment, is shown in the Figure 6.7. The emission spectra show an approximate 25-fold increase in FITC signal over the control particles, clearly proving that specific

binding of avidin to the silica particles has been achieved, and that the signal from the control particles is likely a result of some physical adsorption of avidin onto the particles in a negligible amount. This is a conservative estimate because controls with APTES-modified beads showed that the non-specific binding is about a factor of two-fold less than with the unmodified beads, however this result is superior to the non-silica coated nanoparticles previously reported by us.[26] The effect of nanoparticles aggregation after bioconjugation has yet been studied on our silica-coated nanoparticles. Our previous work has shown that coating the surface of $LaF_3:Ln^{3+}$ nanoparticles with poly(ethylene glycol)-based ligands minimized the effects of non-specific binding, and we expect the same result with our current silica particles.[26] No terbium emission was observed because of the low absorption coefficient of Tb^{3+} ions when compared to FITC.

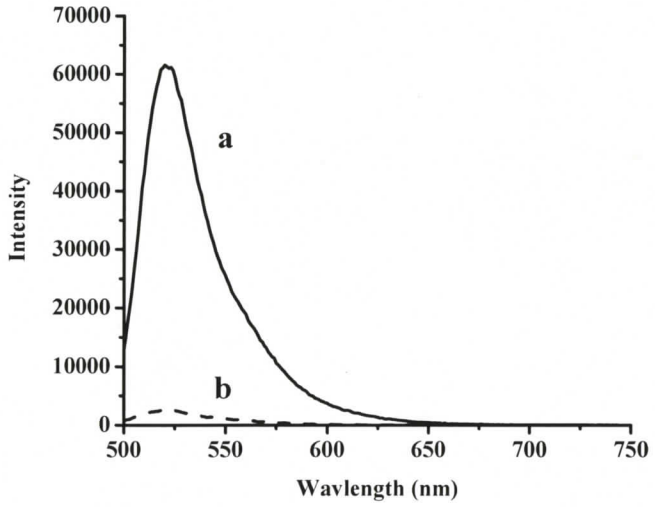

Figure 6.7. Emission spectra of silica-coated LaF_3:Tb nanoparticle after bioconjugation with FITC-avidin beads a) specific binding, b) non-specific binding (λ_{ex} = 485 nm, excitation source – 450 W Xe lamp).

Figure 6.8 shows the Tb^{3+} emission spectrum of the particles excited with high excitation power, in which the dominant 544 nm peak of Tb^{3+} is visible on top of the FITC signal with an effective luminescent lifetime of 3.2 ms (inset in Figure 6.8), which is in agreement with that of the unmodified and APTMS modified particles.

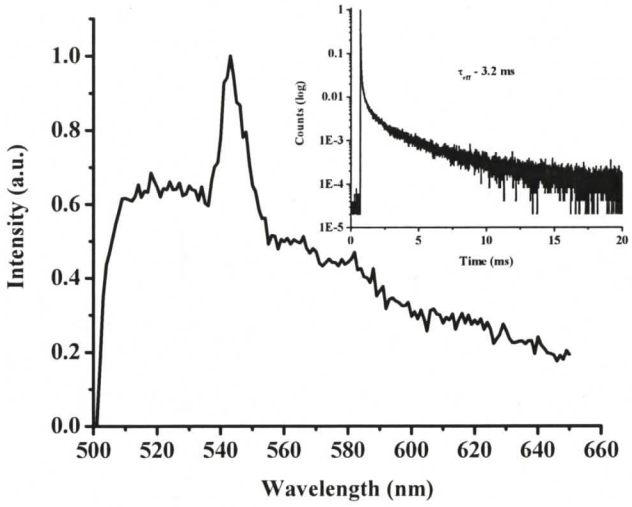

Figure 6.8. The emission spectrum of FITC-avidin bound silica-coated LaF_3:Tb nanoparticles in 10 mM phosphate-buffered saline solution. (λ_{ex} = 485 nm, excitation source - OPO). Inset shows the decay curve of Tb^{3+} ion (λ_{ex} = 485 nm, λ_{em} = 542 nm). The effective lifetime was calculated by neglecting the initial part of the decay curve (0 – 0.8 ms), which is from FITC.

The same binding experiments were carried on silica-coated LaF_3:Nd nanoparticles resulting in approximate thee-fold increase in FITC emission over the control particles (Figure 6.9). The extent of specific binding of avidin to silica-coated LaF_3:Nd nanoparticles is less when compared to silica-coated LaF_3:Tb nanoparticles because the availability of OH groups on silica for surface modification is less in 800°C

heated silica-coated LaF_3:Nd nanoparticles. However, our group has addressed this issue by developing a fresh silica shell over this heated silica-coated $LaF_3:Ln^{3+}$ nanoparticle. Figure 6.10 shows the emission spectrum of the silica-coated LaF_3:Nd nanoparticles, showing the characteristic peaks at 870 nm, 1064 nm and 1330 nm, with an effective luminescent lifetime of 178 μs (inset in Figure 6.10), which is in agreement with that of the unmodified particles.

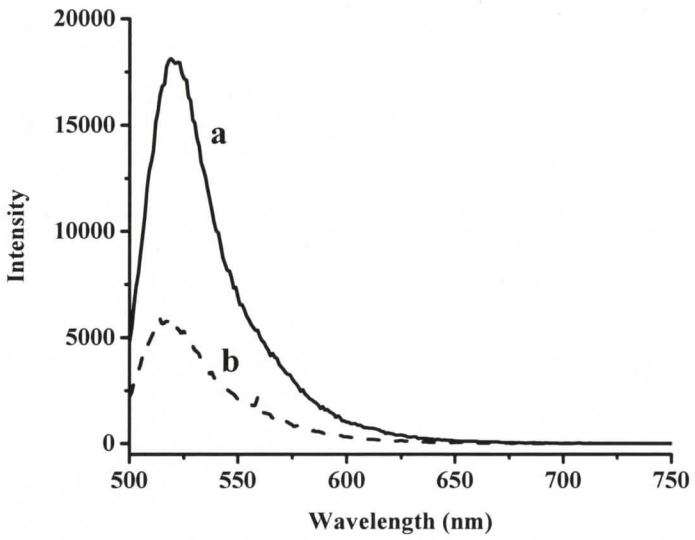

Figure 6.9. Emission spectra of silica-coated LaF_3:Nd nanoparticle after bioconjugation with FITC-avidin beads in 10 mM phosphate-buffered saline solution a) specific binding, b) non-specific binding (λ_{ex} = 485 nm, excitation source – 450 W Xe lamp).

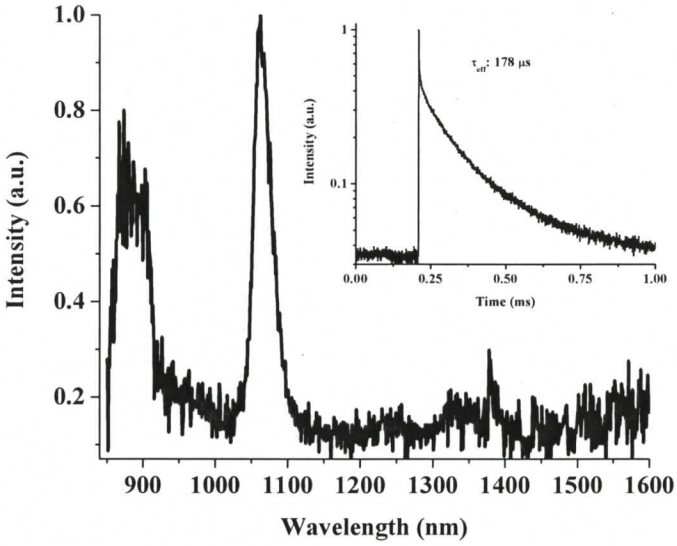

Figure 6.10. The emission spectrum of FITC-avidin bound silica-coated LaF_3:Nd nanoparticles in 10 mM phosphate-buffered saline solution. (λ_{ex} = 514 nm, excitation source - OPO). Inset shows the decay curve of Nd^{3+} ion (λ_{ex} = 514 nm, λ_{em} = 1070 nm).

The formation of the silica coating over the LaF_3:Nd and LaF_3:Yb,Er nanoparticles improved the NIR luminescence significantly by minimizing the solvent quenching effect as compared to our previously reported citrate and 2-aminoethylphosphate stabilised LaF_3:Nd nanoparticles.[26]

6.3. Conclusion

In conclusion, a general and facile method for the production of bioconjugated silica-coated LaF_3:Ln^{3+} nanoparticles with a uniform size distribution has successfully been demonstrated. A wide range of emission lines (450 – 1650 nm) by up- and down-conversion processes have been achieved by doping with different lanthanide ions. In

particular, the excitation with 980 nm light on co-doped silica-coated LaF_3:Yb,Tm nanoparticles resulted in 800 nm emission by up-conversion processes, which is of potential to biological applications. The surface modification of silica-coated nanoparticles with APTMS, followed by the NHS-activated biotin derivative for biotin-avidin binding, resulted in at least a 25-fold increase in the FITC signal over non-biotin functionalized silica- coated nanoparticles.

6.4. Experimental Section

Chemicals of the highest purity were obtained from Aldrich and used without further purification. The FITC-avidin was obtained from Invitrogen and used as received. All water used was distilled. All nanoparticles were made with LaF_3 were doped at the respective % atom doping on the total Ln^{3+} amount.

6.4.1. Synthesis of nanoparticles

Citrate-stabilised LaF_3:Ln^{3+} nanoparticles were prepared by the same procedure reported in chapter 3.

6.4.2. Synthesis of silica-coated LaF_3:Ln^{3+} nanoparticles

Citrate stabilised LaF_3:Ln^{3+} nanoparticles (50 mg) dissolved in 1.44 ml of distilled water was added to ethanol (20 ml) and 30% NH_4OH (0.4 ml) mixture. 1.2 ml of tetraethyl orthosilicate (TEOS) was added to the above mixture. The mixture was stirred

for 60 min. White coloured silica beads were centrifuged and washed with ethanol for several times. Silica beads were dried under vacuum. Silica-coated LaF_3:Nd, LaF_3:Yb,Er, and LaF_3:Yb,Tm nanoparticles were heated at 800°C for 12 h in air.

6.4.3. Surface modification of the silica-coated $LaF_3:Ln^{3+}$ nanoparticles with 3-aminopropyltrimethoxysilanes (APTMS)

Silica-coated $LaF_3:Ln^{3+}$ nanoparticles (10 mg) were suspended in 10 ml of ethanol, followed by the addition of 0.5 ml (2 mmol) of APTMS and stirred for 24 h at room temperature. The particles were isolated and purified by centrifugation, washed 3 times with ethanol and dried under reduced pressure.

6.4.4.Biotinylation of silica-coated $LaF_3:Ln^{3+}$ nanoparticles

APTMS modified silica-coated $LaF_3:Ln^{3+}$ nanoparticles (10 mg) were suspended in 2 ml of DMSO, followed by the addition of 10 mg (0.03 mmol) of (+)-biotin *N*-hydroxysuccinimide ester and stirred for 1.5 h at room temperature. The particles were isolated and washed by centrifugation, washed once with water and thee times with ethanol, and dried under reduced pressure.

6.4.5. Biotin-FITC-avidin binding

Amine-modified silica-coated $LaF_3:Ln^{3+}$ nanoparticles (10 mg) were suspended in 10 ml of 10 mM phosphate-buffered saline, pH 7.4, followed by the addition of 0.4 ml of FITC-avidin (final avidin concentration of 0.1 mg/ml) and stirred for 2.5 h at room

temperature. The particles were isolated and purified by centrifugation, washed 5 times with 10 mM phosphate-buffered saline solution and resuspended in 10 ml of 10 mM phosphate-buffered saline solution.

6.4.6. Transmission Electron Microscope (TEM)

TEM analysis of the silica-coated $LaF_3:Ln^{3+}$ nanoparticles was carried out using a Hitachi H-7000 microscope, operated at 100 kV. Around 1-2 mg of sample was dispersed in 5 ml of ethanol and a drop of this mixture was evaporated on a carbon-coated 300 mesh copper grids. Around 45 images were recorded from different regions of the same sample and an average particle size was obtained based on a minimum of 100 particles.

6.4.7. Luminescence studies

All the emission spectra (down-conversion and up-conversion), lifetime analysis were done by using the same set-up reported in the chapter 3.

References

(1) Bruchez, M.; Moronne, M.; Gin, P.; Weiss, S.; Alivisatos, A. P. *Science* **1998**, *281*, 2013.

(2) Chan, W. C. W.; Nie, S. M. *Science* **1998**, *281*, 2016.

(3) Banks, P. R.; Paquette, D. M. *Bioconjug. Chem.* **1995**, *6*, 447.

(4) Holmes, K. L.; Lantz, L. M. *Methods Cell Biol.* **2001**, *63*, 185.

(5) Bailey, R. C.; Nam, J. M.; Mirkin, C. A.; Hupp, J. T. *J. Am. Chem. Soc.* **2003**, *125*, 13541.

(6) Goldman, E. R.; Balighian, E. D.; Mattoussi, H.; Kuno, M. K.; Mauro, J. M.; Tran, P. T.; Anderson, G. P. *J. Am. Chem. Soc.* **2002**, *124*, 6378.

(7) Jaiswal, J. K.; Mattoussi, H.; Mauro, J. M.; Simon, S. M. *Nature Biotechnol.* **2003**, *21*, 47.

(8) Rosenthal, S. J.; Tomlinson, A.; Adkins, E. M.; Schoeter, S.; Adams, S.; Swafford, L.; McBride, J.; Wang, Y. Q.; DeFelice, L. J.; Blakely, R. D. *J. Am. Chem. Soc.* **2002**, *124*, 4586.

(9) Taylor, J. R.; Fang, M. M.; Nie, S. M. *Anal. Chem.* **2000**, *72*, 1979.

(10) Kobayashi, Y.; Katakami, H.; Mine, E.; Nagao, D.; Konno, M.; Liz-Marzan, L. M. *J. Colloid. Interface Sci.* **2005**, *283*, 392.

(11) Nam, J. M.; Stoeva, S. I.; Mirkin, C. A. *J. Am. Chem. Soc.* **2004**, *126*, 5932.

(12) Parak, W. J.; Gerion, D.; Pellegrino, T.; Zanchet, D.; Micheel, C.; Williams, S. C.; Boudreau, R.; Le Gros, M. A.; Larabell, C. A.; Alivisatos, A. P. *Nanotechnol.* **2003**, *14*, R15.

(13) Wang, F.; Tan, W. B.; Zhang, Y.; Fan, X. P.; Wang, M. Q. *Nanotechnol.* **2006**, *17*, R1.

(14) Loo, C.; Lowery, A.; Halas, N.; West, J.; Drezek, R. *Nano Letters* **2005**, *5*, 709.

(15) Nehl, C. L.; Grady, N. K.; Goodrich, G. P.; Tam, F.; Halas, N. J.; Hafner, J. H. *Nano Letters* **2004**, *4*, 2355.

(16) Binnemans, K.; Van Deun, R.; Gorller-Walrand, C.; Adam, J. L. *J. Non-Cryst. Solids.* **1998**, *238*, 11.

(17) Heer, S.; Kompe, K.; Güdel, H. U.; Haase, M. *Adv. Mater.* **2004**, *16*, 2102.

(18) Patra, A.; Friend, C. S.; Kapoor, R.; Prasad, P. N. *J. Phys. Chem. B* **2002**, *106*, 1909.

(19) Stouwdam, J. W.; van Veggel, F. *Langmuir* **2004**, *20*, 11763.

(20) Stouwdam, J. W.; van Veggel, F. C. J. M. *Nano Letters* **2002**, *2*, 733.

(21) Sudarsan, V.; van Veggel, F.; Herring, R. A.; Raudsepp, M. *J. Mater. Chem.* **2005**, *15*, 1332.

(22) Vetrone, F.; Boyer, J. C.; Capobianco, J. A.; Speghini, A.; Bettinelli, M. *J. Phys. Chem. B* **2003**, *107*, 1107.

(23) Werts, M. H. V.; Jukes, R. T. F.; Verhoeven, J. W. *Phys. Chem. Chem. Phys.* **2002**, *4*, 1542.

(24) Feldmann, C.; Justel, T.; Ronda, C. R.; Schmidt, P. J. *Adv. Funct. Mater.* **2003**, *13*, 511.

(25) Wright, J. C. *Top. Appl. Phys.* **1976**, *15*, 239.

(26) Diamente, P. R.; Burke, R. D.; van Veggel, F. C. J. M. *Langmuir* **2006**, *22*, 1782.

(27) Diamente, P. R.; van Veggel, F. C. J. M. *J. Fluor.* **2005**, *15*, 543.

(28) Meiser, F.; Cortez, C.; Caruso, F. *Angew. Chem. Int. Ed.* **2004**, *43*, 5954.

(29) Wang, L. Y.; Yan, R. X.; Hao, Z. Y.; Wang, L.; Zeng, J. H.; Bao, H.; Wang, X.; Peng, Q.; Li, Y. D. *Angew. Chem. Int. Ed.* **2005**, *44*, 6054.

(30) Beaurepaire, E.; Buissette, V.; Sauviat, M. P.; Giaume, D.; Lahlil, K.; Mercuri, A.; Casanova, D.; Huignard, A.; Martin, J. L.; Gacoin, T.; Boilot, J. P.; Alexandrou, A. *Nano Lett.* **2004**, *4*, 2079.

(31) Louis, U.; Bazzi, R.; Marquette, C. A.; Bridot, J. L.; Roux, S.; Ledoux, G.; Mercier, B.; Blum, L.; Perriat, P.; Tillement, O. *Chem. Mater.* **2005**, *17*, 1673.

(32) Corstjens, P.; Zuiderwijk, M.; Brink, A.; Li, S.; Feindt, H.; Neidbala, R. S.; Tanke, H. *Clin. Chem.* **2001**, *47*, 1885.

(33) Ow, H.; Larson, D. R.; Srivastava, M.; Baird, B. A.; Webb, W. W.; Wiesner, U. *Nano Lett.* **2005**, *5*, 113.

(34) Gerion, D.; Parak, W. J.; Williams, S. C.; Zanchet, D.; Micheel, C. M.; Alivisatos, A. P. *J. Am. Chem. Soc.* **2002**, *124*, 7070.

(35) Sivakumar, S.; van Veggel, F. C. J. M.; Raudsepp, M. *J. Am. Chem. Soc.* **2005**, *127*, 12464.

(36) Sudarsan, V.; Sivakumar, S.; van Veggel, F. C. J. M.; Raudsepp, M. *Chem. Mater.* **2005**, *17*, 4736.

(37) Stöber, W.; Fink, A.; Bohn, E. *J. Colloid Interface Sci.* **1968**, *26*, 62.

Summary

This thesis describes the incorporation of lanthanide-doped nanoparticles into sol-gel matrices to improve the optical properties of lanthanide ions and they can potentially be used in white light devices, optical amplifiers, lasers, and biolabeling.

Chapter 1 covers the historical development and technological importance of white light sources. In order to generate efficient white light a material is required to have a stable photocycle, a cheap energy source, and an easy and cost effective fabrication.

The unique optical properties of lanthanide ions have been discussed in chapter 2. The three major up-conversion mechanisms have been described in detail and are accompanied by examples, i.e. 1) ground state absorption/excited state absorption, ii) energy transfer, and iii) photon-avalanche mechanisms. Despite the higher efficiency of photon-avalanche mechanism when compared to other two, it suffers from a number of drawbacks such as weak ground state absorption, longer temporal evolution time, and need of high pump fluxes to reach the threshold condition. The optical properties of lanthanide ion in organic complexes, inorganic bulk materials, and inorganic nanoparticles have been described. It discusses the reasons for the inefficient luminescence of lanthanide-complexes and disadvantages of lanthanide-doped inorganic bulk materials. The lanthanide-doped inorganic nanoparticles have advantages such as processability, and improved optical properties over other matrices. The technological importance of incorporation of these processable nanoparticles in sol-gel matrices together with historical development of sol-gel process have been discussed.

The generation of white light from sol-gel thin films (SiO_2 and ZrO_2) made with lanthanide-doped nanoparticles through up-conversion of a single 980 nm light source has been demonstrated in chapter 3. In part I, the first example of the generation of white

light has been described from SiO_2 and ZrO_2 sol-gel thin films made with Eu/Er/Tm-doped nanoparticles. Eu^{3+} and Tm^{3+} ions are responsible for red and blue emission, respectively. Er^{3+} ion is responsible for green as well as deep red emission. The control experiments proved the need of Ln^{3+} doped nanoparticles rather than Ln^{3+} ion directly incorporated in SiO_2 and ZrO_2 thin films. The efficiency of generation of white light has been improved by incorporation of new combinations of lanthanide-doped nanoparticles which is discussed in part II. A 33-fold increase in the white light emission intensity was observed from silica thin film made with Combination 2 (Yb/Tm and Yb/Er) nanoparticles when compared to the thin film discussed in part I. The estimated efficiency of production of the resulting white light is 12.5%, which is based on the efficiency of energy transfer and quantum yield of the Ln^{3+} emission. Similarly, SiO_2/ZrO_2 thin film made with combination 1 (Yb/Tm, Yb/Ho, and Yb/Er), combination 3 (Yb/Tm, Yb/Tb, and Yb/Er), and combination 4 (Yb/Tm, Yb/Tb, and Yb/Eu) nanoparticles also produced white light with higher efficiency when compared to thin film discussed in part I. The up-conversion mechanisms involved in the generation of light has been discussed.

In chapter 4, bright green and red luminescence has been generated from silica sol-gel thin films made with $La_{0.45}Yb_{0.50}Er_{0.05}F_3$ nanoparticles through a newly-described hetero-looping-enhanced energy-transfer (*hetero*-LEET) up-conversion process, which exhibits a power dependence *similar* to that of a photon-avalanche (PA). The *hetero*-LEET mechanism is potentially more efficient than PA, ground state absorption/excited state absorption (GSA/ESA), and energy-transfer (ETU) mechanisms because it combines resonant ground-state absorption with an avalanche-like feedback process.

Preparation of semiconductor sol-gel thin films (In_2O_3, HfO_2, and ZrO_2) with lanthanide-doped nanoparticles has been discussed in chapter 5. These semiconductor sol-gel thin films show energy transfer from the semiconductor matrix (In_2O_3, $La_2Hf_2O_7$, and $La_2Zr_2O_7$) to the lanthanide ions. The absence of blue emission from the In_2O_3 matrix (due to oxygen vacancies) suggests that the energy transfer is efficient. Highly dispersible In_2O_3-coated LaOF:Ln^{3+} doped nanoparticles have been prepared and they also show energy transfer from semiconductor matrix to lanthanide ions. The particle sizes are in the range of 60-70 nm. These semiconductor-coated nanoparticles are potential candidates for polymer-based LEDs.

The preparation and bioconjugation of nearly monodisperse (40 nm) silica-coated LaF_3:Ln^{3+} nanoparticles has been described in chapter 6. Doping of the LaF_3 core with selected luminescent Ln^{3+} ions allows the particles to display a range of emission lines from the visible to the near-infrared region (450-1650 nm). Er^{3+} ions gave green and deep red emission and Tm^{3+} ion gave 800 nm emission, via up-conversion processes when co-doped with Yb^{3+} (λ_{ex} = 980 nm). Bioconjugation of avidin, to which a fluorophore FITC was bound, was acting as the reporter of the binding event. This was first done by surface modification of the silica particles with 3-aminopropyltrimethoxysilane, followed by the reaction of the biotin-*N*-hydroxysuccinimide activated ester to form an amide bond, imparting biological activity to the particles. A 25-fold or better increase in the FITC signal over the non-biotinylated silica particles indicates that there is minimal non-specific binding of FITC-avidin to the silica particles.